Wallace Torres de Figueiredo

Elucidating the electronic nature of the Strong Metal-Support Interaction (SMSI) effect

UFRGS
UNIVERSIDADE FEDERAL
DO RIO GRANDE DO SUL

Porto Alegre, RS - Brazil
August, 2022

Wallace Torres de Figueiredo

Elucidando a natureza eletrônica do efeito de Forte Interação Metal-Suporte (SMSI)

Tese realizada sob a orientação do Prof. Dr. Fabiano Bernardi e coorientação do Prof. Dr. Maximiliano Segala, apresentada ao Instituto de Física da Universidade Federal do Rio Grande do Sul, em preenchimento parcial dos requisitos para a obtenção do título de Doutor em Física.

Universidade Federal do Rio Grande do Sul

Instituto de Física

Programa de Pós-Graduação em Física

Orientador: Prof. Dr. Fabiano Bernardi

Coorientador Prof. Dr. Maximiliano Segala

Porto Alegre, RS - Brasil

Agosto, 2022

Acknlowledgment

Firstly, I would first like to thank Prof. Dr. Fabiano Bernardi for his guidance, advisement, patience, and friendship. Throughout this period there were dark times when I was unable to achieve my best performance, yet Prof. Fabiano always gave me space and time to reorganize my thoughts. The door to Prof. Bernardi was always open whenever I ran into a trouble spot or had a question about my research. He consistently steered me into the right path, whenever he thought I needed it. Further, I would like t thank to Prof. Dr. Maximiliano Segala who magnified my understanding of computational methods, provided important tips and insights that allowed me achieve better understanding of the modeling techniques and electronic phenomena.

I would also like to thank Profs. Dr. Sílvio Buchner, Dr. Oscar Pérez, Dr. Edmar Soares, Dr. Ravi Prakash, and Dr. Roland Hergenröder by supplying me with the better facilities to accomplish the experimental measurements of this work.

My thanks and appreciation also go to my colleagues who have ennobled my knowledge through enriching discussions, and to all those people who have made my stay away from home more happier and enjoyable. The friends that I made in the lab and daily discussions I will take for life. In special, I would like to thank Alisson, Lívia, Marco, and their families for their reception and all the kindness shared with me. Some older friends have kept me on the right track and nurtured my desire to become a scientist. Lucas, Ludmila, and Natália, you were paramount for my personal evolution, in academia and in life. Thanks for everything.

At last, but not least, I have to thank my family for their support. My mother and sister have always backed me, whenever I needed them. Such support eased my stay away from our house and pushed me to finish the job.

"Natural science, does not simply describe and explain nature;
it is part of the interplay between nature and ourselves."
Werner Karl Heisenberg

ABSTRACT

As industrial interest turned to the development of petrochemical processes, the investment in the development of the heterogeneous catalysis field increased. Nevertheless, classical catalysts still present unsettled phenomena in industrial conditions. An example of such obscure behavior is the suppression of H_2 (and CO) chemisorption capacity of some noble metal nanoparticles supported on reducible oxides after high temperature reduction treatments. This event is known in the literature as the Strong Metal-Support Interaction (SMSI) effect and has been extensively studied over the past 40 years due to the dramatic alteration of substantial catalytic properties such as the sorption capacities. In spite of the high number of studies in the field, the SMSI effect is not completely understood from the fundamental point of view. Intending to answer the open questions about the nature of electronic phenomena regarding the SMSI effect, this work presents an experimental-computational investigation of the changes in the electronic structure of Pd/MO (MO = TiO_2, CeO_2 and Nb_2O_5) nanoparticles induced by the occurrence of such interaction. Initially, the dimensions of the as prepared samples were explored by means of Transmission Electron Microscopy (TEM) and Dynamic Light Scattering (DLS) measurements. The crystalline structure of the metal and oxide nanoparticles were determined by X-ray Diffraction (XRD) measurements. A combination of ex-situ X-ray Photoelectron Spectroscopy (XPS) and Ultraviolet Photoelectron Spectroscopy (UPS) measurements explored the surface state of Pd/MO nanoparticles after reduction (H_2) and oxidation (O_2) treatments at low (300 °C) and high (500 °C) temperatures. Photoelectron Spectroscopy measurements evidenced the occurrence of the geometrical factor of the SMSI effect on some of the reducible oxide (TiO_2 and Nb_2O_5) supported samples, at high (500 °C) temperature reduction treatments, through the detection of an oxide encapsulation layer covering the Pd nanoparticles surface. At the same time, UPS measurements evidenced that at lower reduction temperatures, the electronic interactions overcome the geometrical feature of the SMSI effect, present at all Pd/MO systems studied. Near-Ambient Pressure (NAP) XPS measurements revealed that the electronic interaction occurred at lower temperature treatments induced energetic shifting of the core levels of both metal and oxide, evidencing charge transfers from the Pd nanoparticles to its oxide support, mediated by Pd-O-M (M = Ti, Ce, Nb) entities formed at the metal/support interface. Further, it was verified that such electronic interactions survive oxidation treatments, differently than the classical SMSI effect encapsulation phenomenon. Density Functional Theory (DFT) calculations provided details regarding these interface interactions, revealing that the apparent orbital hybridization of O p (from the support) with Pd d

valence orbitals are the entities responsible to build the Pd-metal oxide bridges, mediated by O bonds, for the charge transfer. Furthermore, evaluating the charge distribution at the systems, DFT calculations reinforced the charge transfer phenomena indicating alterations in the charge concentration at the interface in comparison with the farther regions. The results from this work help to control the surface properties of nanostructured systems, allowing the development of a new generation of optimized catalysts.

RESUMO

Ao passo que o interesse industrial se voltou ao desenvolvimento de processos petroquímicos, o investimento no desenvolvimento de pesquisa na área de catálise heterogênea aumentou. No entanto, catalisadores clássicos ainda apresentam fenômenos pouco entendidos em condições industriais. Um exemplo de tal comportamento obscuro é a supressão da capacidade de quimisorção de H_2 (e CO) de algumas nanopartículas de metais nobres suportadas em óxidos redutíveis após tratamentos de redução em alta temperatura. Esse evento é conhecido na literatura como efeito de forte interação metal-suporte (SMSI - Strong Metal-Support Interaction) e tem sido extensivamente estudado nos últimos 40 anos devido à dramática alteração de propriedades catalíticas fundamentais, como a capacidade de sorção. Apesar do expressivo número de estudos nesta área, o efeito SMSI não é completamente compreendido do ponto de vista fundamental. Com o objetivo de responder às questões abertas sobre a natureza do efeito SMSI, este trabalho apresenta uma investigação experimental-computacional sobre as alterações da estrutura eletrônica de nanopartículas de Pd/OM (OM = TiO_2, CeO_2 e Nb_2O_5) induzidas pela ocorrência de tal interação. Inicialmente, as dimensões das amostras preparadas foram exploradas por meio de medidas de Microscopia Eletrônica de Transmissão (TEM), e Espalhamento Dinâmico de Luz (DLS). A estrutura cristalina das nanopartículas metálicas e dos óxidos foram determinadas por medidas de difração de Raios-X (XRD). Combinando medidas ex-situ de Espectroscopia de Fotoelétrons Excitados por Raios-X (XPS) e Espectroscopia de Fotoelétrons Excitados por Ultravioleta (UPS), foi explorado o estado das superfícies das nanopartículas de Pd/OM após tratamentos de redução (H_2) e oxidação (O_2) em baixas (300 °C) e altas (500 °C) temperaturas. As medidas de XPS evidenciaram a ocorrência do fator geométrico do efeito SMSI nas amostras suportadas em alguns dos óxidos redutíveis (TiO_2 e Nb_2O_5), em tratamentos de redução em alta (500 °C) temperatura, através da detecção de uma camada de óxido encobrindo a superfície das nanopartículas de Pd. Ao mesmo tempo, as medidas de UPS evidenciaram quem em baixas temperaturas de redução, as interações eletrônicas dominam as características geométricas do efeito SMSI, presentes em todos sistemas Pd/MO estudados. O estudo dos espectros de UPS dessas nanopartículas revelou que os estados eletrônicos associados ao efeito SMSI no metal e no suporte são semelhantes para as amostras suportadas em TiO_2 e CeO_2, onde é observada transferência de carga do suporte para as nanopartículas de Pd. Cálculos usando a Teoria do Funcional da Densidade (DFT) correlacionaram a ocorrência das interações eletrônicas nos sistemas apresentando o efeito SMSI com a formação de estados não-ligantes de O na interface metal-suporte.

Medidas de XPS próximas à pressão ambiente (NAP-XPS) revelaram que as interações eletrônicas verificadas nos tratamentos de redução em baixas temperaturas induziram deslocamento energético em níveis de caroço de ambos metal e óxido, evidenciando transferências de carga das nanopartículas de Pd para o óxido de suporte, medidados por entidades do tipo Pd-O-M (M = Ti, Ce, Nb) formados na interface entre metal e suporte. Além disso, foi verificado que estas interações eletrônicas sobrevivem a tratamentos de oxidação, diferentemente do clássico fenômeno de encapsulação do efeito SMSI. Cálculos usando a Teoria do Funcional da Densidade (DFT) proveram detalhes a respeito dessas interações de interface, indicando que a hibridização aparente de estados de valência O p (provenientes do suporte) e Pd d são as entidades eletrônicas responsáveis por construir as pontes eletrônicas Pd-óxido metálico, mediadas por ligações com O, para as transferências de carga. Mais além, avaliando a distribuição de cargas nos sistemas, os cálculos de DFT reforçam a fenômeno da transferência de carga indicando alterações nas concentrações de cargas na interface metal/suporte quando comparadas com regiões mais distantes. Os resultados desse trabalho auxiliam no controle das propriedades de superfície de sistemas nanoestruturados, permitindo o desenvolvimento de uma nova geração de catalisadores otimizados.

Press release

The Physics of Nanostructures Laboratory has been developing research including the investigation of fundamental phenomena (developing basic science) and the application of structured systems at the atomic level to solve current problems such as the production and storage of renewable energies. One of the research focuses is associated with the study of the surface properties of nanostructured materials. These properties are mainly established by the electrons present in the surface atoms of these nanomaterials. In this way, phenomena that alter the distribution of surface electrons directly influence the physicochemical characteristics of materials, which may improve or prevent the application of the nanostructure.

One of the effects of great impact on the properties of nanostructured catalysts is known as the Strong Metal-Support Interaction Effect (or SMSI effect), which manifests itself through electronic and geometric phenomena. Although the occurrence of this effect has been observed for more than 40 years, several questions regarding the nature of such effect have remained unanswered until then. Using a combination of experimental and computational techniques, this work revealed the mechanisms by which the electronic phenomena of the 'SMSI' effect occurs. The results obtained allowed the identification of the thermal and atmospheric conditions for the occurrence of electronic interactions, and with that the control of such phenomenon, enabling the engineering of nanocatalysts to tune such interaction whenever it is interesting.

Comunicado de Imprensa

O Laboratório de Física de Nanoestruturas tem desenvolvido pesquisas desde a investigação de fenômenos fundamentais (desenvolvendo ciência basilar) até a aplicação de sistemas estruturados em nível atômico na solução de problemas atuais como a produção e armazenamento de energias renováveis. Um dos focos de pesquisa está associado ao estudo das propriedades da superfície dos materiais nanoestruturados. Essas propriedades são estabelecidas principalmente pelos elétrons presentes nos átomos da superfície desses nanomateriais. Dessa maneira, fenômenos que alteram a distribuição dos elétrons de superfície influenciam diretamente nas características físico-químicas dos materiais, podendo aprimorar ou impossibilitar a aplicação da nanoestrutura.

Um dos efeitos de grande impacto para as propriedades de catalisadores nanoestruturados é conhecido como o Efeito de Forte Interação Metal-Suporte (em inglês, *SMSI effect*), que se manifesta através de fenômenos eletrônicos e geométricos. Embora a ocorrência desse efeito seja observada há mais de 40 anos, várias perguntas a respeito da natureza desse efeito permaneceram sem resposta até então. Utilizando a combinação de técnicas experimentais e computacionais, este trabalho revelou os mecanismos pelos quais os fenômenos eletrônicos do efeito 'SMSI' acontecem. Os resultados obtidos permitiram a identificação das condições térmicas e atmosféricas para a ocorrência das interações eletrônicas, e com isso o controle de tal fenômeno, habilitando a engenharia de nanocatalisadores sintonizar tal interação quando for interessante.

List of Figures

List of Tables

Contents

List of abbreviations and acronyms

a.u.	Arbitrary Units
AC	Analysis Chamber
CAE	Constant Analyzer Energy
CESUP	Centro Nacional de Supercomputação
CCD	Charge-Coupled Device
CMM	Centro de Microscopia e Microanálise
CNANO	Centro de Nanociência e Nanotecnologia
CRR	Constant Retard Ratio
DFT	Density Functional Theory
DLS	Dynamical Light Scattering
DRIFTS	Diffuse Reflectance Infrared Fourier Transform Spectroscopy
DTA	Differential Thermal Analysis
EDS	Energy-dispersive X-ray Spectrometry
EELS	Electron Energy Loss Spectroscopy
FWHM	Full Width at Half Maximum
HRTEM	High-Resolution Transmission Electron Microscopy
HTR	High-temperature reduction
HSA	Hemispherical Sector Analyzer
ICSD	Inorganic Crystal Structures Database
LAMINAT	Laboratório de Micro e Nanopartículas Aplicadas a Terapeutica
LAPMA	Laboratório de Altas Pressões e Materiais Avançados
LS	Long Scan
LTR	Low-temperature reduction

NAP-XPS	Near Ambient Pressure X-ray Photoelectron Spectroscopy
PROCAT	Laboratório de Processos Catalíticos
SMSI	Strong Metal-Support Interaction
STEM	Scanning Transmission Electron Microscopy
TCD	Thermal Conductivity Detector
TEM	Transmission Electron Microscopy
TPR	Temperature-Programmed Reduction
UPS	Ultraviolet Photoelectron Spectroscopy
XPS	X-ray Photoelectron Spectroscopy
XRD	X-ray Diffraction

List of symbols

$\hat{A}$	Vector potential operator
$\alpha(\omega_i)$	Orbital spin function
c	Light speed
χ^2	*Chi* squared factor, indicating the quality of a XPS fit
χ_i	Orbital wave function
D	Particles mean diameter
D_s	Self-diffusion coefficient
$D_{ef}(T_n)$	Detector efficiency for electrons of kinetic energy T_n
ΔT	Temperature difference
e	Electron charge
E	Energy
E_b	Binding energy
E_F	Fermi energy
E_{rot}	Rotational energy
E_{vib}	Vibrational energy
E_{XC}	Exchange-correlation energy
$\hat{\epsilon}$	Polarization vector
$F_s(q,\tau)$	Particle dynamic structure factor
F_X	X-rays flux
ϕ	Quantum state
$\phi(r_i)$	Orbital spatial distribution
h	Planck constant
$h\nu$	Photon energy

I	Intensity
λ_{IMFP}	Inelastic mean free path
m_e	Electron mass
M_{ij}	ij-th element of the M matrix
N_e	Number of electrons
$\psi(r_i)$	Single-particle wave function
$\Psi(r_i)$	Many-particle wave function
Ψ^H	Hartree's wave function
R_{wp}	Rietveld refinement weighted profile residual factor
R_{exp}	Rietveld refinement expected profile residual factor
$\rho(r)$	Electronic density
$\rho_0(r)$	Ground-state electronic density
σ_{nl}	Photoionization cross section of a electron from the atomic level defined by the n and l quantum numbers
T	Kinetic energy
τ_i	i-th time interval
Θ	Angular direction
$\phi_{analyser}$	Spectrometer work function
ϕ_{sample}	Sample work function
ϕ_{as}	Phase-shift caused by scattering processes
UHV	Ultra-high vacuum
V	Electrostatic potential
V_{ext}	External potential
V_{XC}	Exchange-correlation potential
Y_i^{calc}	Calculated intensity at the i point of a diffraction pattern
Y_i^{obs}	Observed intensity at the i point of a diffraction pattern

1 Literature Review

This introductory chapter will present a bird's eye view of the research field in which this project was developed, evidencing the historical understanding regarding the Strong Metal-Support Interaction (SMSI) effect. At the end of the chapter, the project's objectives shall also be presented.

1.1 Catalysis

Since the dawn of society, people have been fascinated by noble metals. It came a time when some people, called *alchemists*, were engaged in discovering/developing a special substance able to convert base metals into noble metals [1]. Despite their unsuccessful attempts, these experimentalists gathered a wide empirical knowledge that, years later, was translated as the laws for the conservation of matter.

The idea of using some chemical substance to convert a compound into another has been applied for centuries. Reports from the sixteenth century already show the use of inorganic compounds to improve the conversion of alcohol into ether [1, 2], however, due to the isolation of these scientists, new discoveries were sporadic. Almost three centuries later, J. J. Berzelius assimilated the most relevant contemporary findings [3–6] under its concept of *catalysis*. Assuming the existence of a natural force, the *catalytic* force, Berzelius concluded that bodies have the ability to decompose some compounds in their elements and recombine them in different forms, remaining unchanged [7, 8].

Discoveries fomented by research in the catalysis field changed the bare perception of chemical reactions. After Wilhelmy's experiments demonstrating the dependency of reactants to a reaction rate [9], van't Hoff developed the theory of chemical equilibria [10] providing a systematic framework for the development of catalysts. Such advances brought industrial relevance to catalysis research at the beginning of the 20th century [1, 11]. At 1905, Fritz Haber developed a method to synthesize ammonia (NH_3) reacting atmospheric nitrogen (N_2) with hydrogen (H_2) in the presence of magnetite (Fe_3O_4). Five years later, Carl Bosch developed an industrial-scale plant at BASF industries for the ammonia production [12]. Haber's achievement solved two of the largest german problems at once: famine and 'homeland security' [13, 14]. At that time, the western world was concerned about the supply of fertilizers (fixed nitrogen) for food crops. About ten years later, it became clear that Germany was also interested in using this ammonia as a bulk chemical in the production of explosives (through the Ostwald process [15]) for the Great War [1].

Haber-Bosch process of producing ammonia become a milestone, changing forever the course of the modern world. As shown in Figure 1.1, the production of fertilizers through the Haber-Bosch process promoted a fast increase in the population growth rate across the world. Erisman and collaborators estimated that, by 2008, nitrogen fertilizers were already responsible to feed about 50% of the world's population [16].

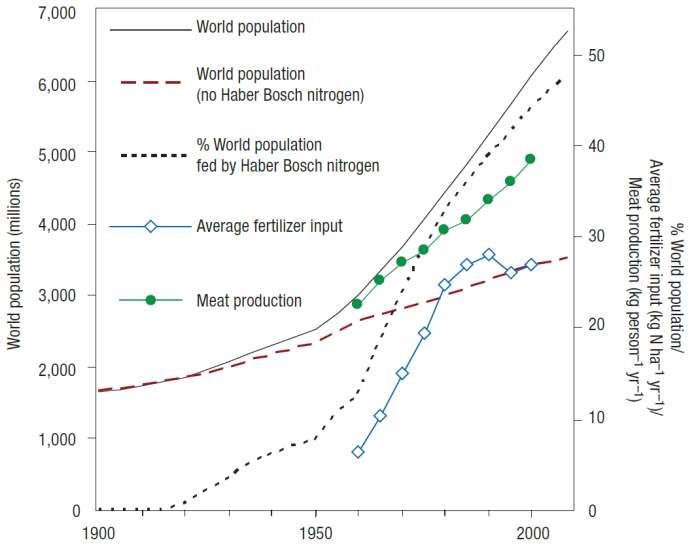

Figure 1.1 – Trends in human population and nitrogen use throughout the twentieth century. From the total world population (solid line), an estimate is made about the number of people that could be sustained without reactive nitrogen from the Haber–Bosch process (long dashed line), and the percentage of the global population using nitrogen from Haber-Bosh process (short dashed line). The recorded increase in average fertilizer use per hectare of agricultural land (blue symbols) and the increase in per capita meat production (green symbols) are also shown. (Image from [16])

After World War II, the rise of the petrochemicals industry followed the European fast expansion of the automotive market, shifting the world's fuel demand from coal to oil, and introducing the appreciation for commodities in the society, which would enhance the human quality of life through the use of polymers such as plastic [1, 17].

The advance of catalysis was an essential aspect responsible for industrial development and can be associated with its collateral effects. Links between the industrial rush of the 20th century and the environmental driving forces associated with climate change have been made [18, 19]. Due to the establishment of more stringent legislation, demanding the emissions control of several chemicals (e.g. hydrodesulfurization of fuels and reduction of NO_x), automotive industries have been supporting researches on new catalytic materials and more efficient processes [20–24] towards sustainable and environment-friendly solutions. The development of such "green chemistry" relies on a multi-stage framework that applies reusable catalysts in reactions yielding the maximum reactants-products conversion and the minimum of waste (by-products, usually undesired)[25, 26]. In this pursuit, the outrunners are the heterogeneous catalysts.

Generically, catalytic processes may be accomplished homogeneously, heterogeneously, or enzymatically [27]. Homogeneous catalysis occurs when the catalyst inserted into the reaction is in the same phase as the reactants (usually liquid). The use of homogeneous catalysts yields high activity and selectivity, even in mild conditions. However, due to the formation of a single-phase mixture, the separation of reaction products is usually expensive [28]. Enzymes are proteins able to catalyze biochemical reactions. These natural catalysts are usually composed of repeating units of amino acids, often twisted in helices to form 3D structures [29]. On the other hand, heterogeneous catalysis takes place when the catalyst is in a different phase than the reactants. A typical heterogeneous process occurs when a solid material (catalyst) is exposed to gaseous (or liquid) reactants. Compared to the homogeneous catalysts, these solid materials are easier to handle, recover, recycle, and cheaper [27]. Considering also the stability under high temperature and steam conditions, the petrochemical industries made the use of heterogeneous catalysts the dominant case in industrial reactions.

The development of optimized catalysts was enabled after the establishment of instrumentation and techniques to characterize materials' properties at the atomic level. In the 1950s, the chemical industries presented expressive progress due to the rise of solid state-based devices industry and the economical availability of ultrahigh vacuum systems [30]. Due to the development of such tools, well-controlled synthesis methods could be established, enabling then the design of optimized catalysts after the correlation of physical-chemical properties of materials to their structural characteristics (shape, size, morphology) [31].

The ability to characterize materials surfaces at the nanoscale enabled scientists to tune the properties of the catalysts through engineering their geometrical structure. By reducing its dimensions from bulk to the nanoscale, several physical properties of materials can be changed. In the literature, one can find alterations in particles' mechanical strength [32–35], optical absorption [36–38], and electrical conductivity [39–41] just by reducing their size. Moreover, by miniaturizing materials one also changes their chemical reactivity. All these alterations are associated with the increase in the percentage of atoms at the surface of the nanoparticles as their size decreases. Figure 1.2 shows an estimation of the percentage of surface atoms of a Pd nanoparticle as a function of its diameter. One can notice that nanoparticles of diameter as big as 3 nm already present less than 50% of their atoms on the surface. The nanosize effect changes electronic and structural properties of the materials, then there is an ideal size for optimizing the catalytic reaction results [42–44]. Whereas size plays a key role in the design of a catalyst, its composition is critical. While many materials will induce the break of the reactants and the formation of new composts, different catalysts compositions can yield a wide variety of reaction products in very distinct amounts.

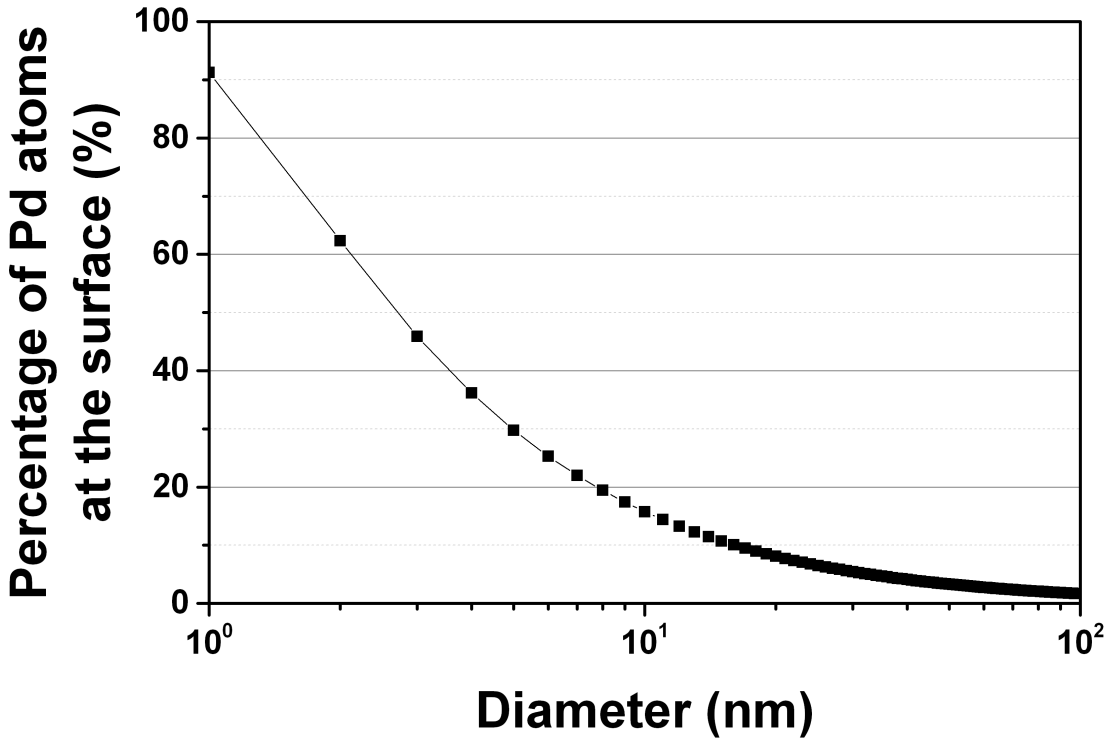

Figure 1.2 – Calculated percentage of surface atoms in Pd nanoparticles as a function of the size.

According to the Sabatier principle, the best catalyst for a given reaction would bind the reactants not so weak that these would still be activated, and not so strong that products would be able to be desorbed. Such bond strength is dependent on the materials' surface composition and their correspondent electronic structure. Transition metals are widely applied as catalysts due to their variety of oxidation states, and ability to exchange electrons with reactants. Due to the presence of wide *d*-bands in these materials' electronic structures, the surfaces of such catalysts are prolific regarding the ability to display active sites for catalysis.

Among transition metals, Palladium's outstanding ability to absorb H_2 (up to 1000 times its own volume [45]) highlights it as very promising material for hydrogen storage. Pd is also one of the earlier catalysts applied to hydrogenation processes and the most common catalyst applied to the emissions control of automotive exhausts [46]. Apart from the automotive industry, pharmaceutical chemists have also exploited the Palladium-based catalysts for organic synthesis due to their versatility in the formation of carbon-carbon bondings and their tolerance to several functional groups, such as carbonyl and hydroxyl [45, 47].

Pd nanoparticles need to be thermally stabilized for avoiding loss of activity. This stabilization can be performed during its synthesis process, e.g., by the use of polymers (large molecules weakly bound to the surface of the nanoparticles) or

dendrimers (highly branched macromolecules assembling molecular containers able to trap/stabilize nanoparticles), or by the deposition of nanoparticles on solid supports. Transition metal oxides (e.g. TiO_2, SiO_2, CeO_2, Fe_2O_3, MgO, ZnO, etc.) are commonly used as support, establishing the thermal stability of the metallic nanoparticles by avoiding agglomeration phenomena, which decreases the surface area of the nanoparticles [48]. Particularly, the surface oxygen vacancies formed on easily reducible oxides can serve as strong anchoring sites for metallic nanoparticles[49, 50]. Besides providing thermal stability, the association of an oxide support to the Pd nanoparticles influences their catalytic activity [51–53]. Berguerand and coworkers have studied the effect of associating different oxide supports on the catalytic activity and selectivity of Pd nanoparticles for the hydrogenation of 2-butyne-1,4-diol[54]. Comparing the results for MgO, ZnO, Ga_2O_3, Al_2O_3, ZrO_2, SnO_2, and SiO_2 supports, the authors linked the systems activity (and selectivity) to the oxide acid-base character. They verified that the Pd nanoparticles on more acidic supports (such as SiO_2) presented higher catalytic activity (up to 10x higher than the more basic oxide, MgO), though lower selectivity.

The electronic disturbance caused by the association of an oxide support to metal nanoparticles may induce alterations in the materials' catalytic properties. Depending on the reaction conditions, strong metal-support interactions may arise disrupting the system morphology, introducing strain, or even promoting charge transfers between its components, as schematized in Figure 1.3.

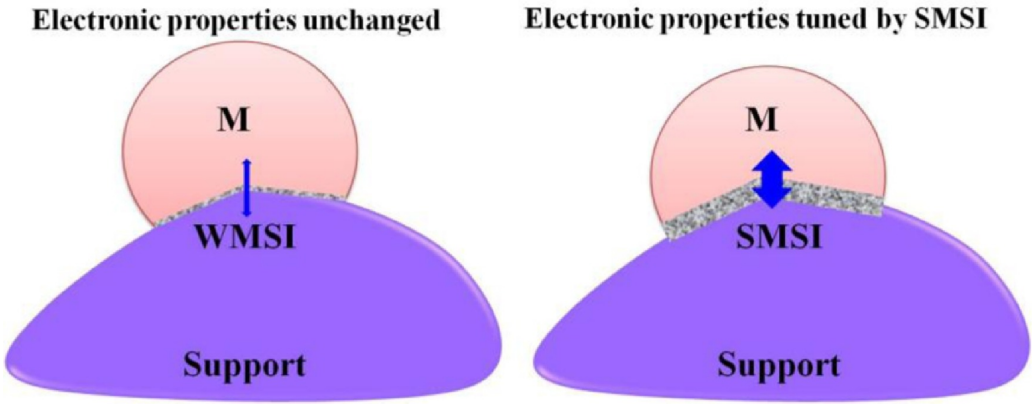

Figure 1.3 – Electronic effects resulting from weak metal-support interactions (WMSI) and strong metal-support interactions (SMSI). The grey crosshatched area evidences the interface region where charge is rearranged and transferred. (Image from [55])

1.2 Metal-Support Interactions

Metal-support interactions are usually related to disturbance of the system properties on the interfacial perimeter. Phenomena such as charge transfer, change in nanoparticle morphology, and mass transport are common to these interaction effects. An early example of a disturbance observed on oxide-supported metal nanoparticles' catalytic properties is now known as the "Strong Metal-Support Interaction" (SMSI) effect.

The SMSI effect was firstly reported by Tauster and coworkers while studying the stability of noble metals supported on TiO_2 after reduction treatments [56]. Monitoring the H_2 and CO absorption on M/TiO_2 (M = Ru, Rh, Pd, Os, Ir, Pt) after reduction treatments (H_2) at 200 °C and 500 °C, the authors verified that for low-temperature treatments (200 °C) noble metals nanoparticles remain dispersed, however, do not achieve complete reduction. Differently, after high-temperature reduction treatments (500 °C), they noticed that the samples' uptake capacity was drastically decreased, for both H_2 and CO. Later, the authors verified that the sorption properties of these systems were recovered after high-temperature oxidation treatment. After discarding agglomeration and poisoning phenomena as responsible for such results, the authors suggested that the high-temperature reduction treatments could lead to chemical interactions between metal and support. The authors suggested that such interactions would involve bondings among noble metal atoms and titanium entities (cations or atoms) at the support surface. Following the interaction model proposed by Dickson [57], Tauster and coworkers argued that these interactions could be associated with the overlapping of electron-rich *d*-bands of noble metals with vacant *d* orbitals of Ti ions at the samples' surfaces. The formation of intermetallic compounds was also considered, being thermodynamically driven by electron transferring phenomena between metal and Ti *d* bands.

The intermetallic interaction hypothesis was further investigated by Horsley through a theoretical approach using Xα self-consistent field molecular orbital calculations [58]. Using a single Pt atom to interact with an octahedral $(TiO_6)^{8-}$ cluster, Horsley evaluated the interaction energies of two configurations: (i) the Pt atom outside the oxide cluster, neighboring oxygen atoms; (ii) the Pt atom replacing one of the oxygen atoms from the cluster. The calculations suggest that the O vacancies (which are typically created during H_2 reduction treatments) allow the approximation of Pt and Ti atoms facilitating the formation of an ionic Pt-Ti interaction with charge transferred from Ti 3d levels to the Pt 5d level, supporting the hypothesis of Tauster and coworkers.

Intending to explore the SMSI effect, Tauster and Fung inspected its occurrence on different support oxides [59]. Using Ir nanoparticles supported on MgO, Sc_2O_3, Y_2O_3, TiO_2, ZrO_2, HfO_2, V_2O_3, Nb_2O_5, and Ta_2O_5, the authors verified a correlation between the SMSI effect occurrence and the support reducibility. Surveying the temperature of

reduction treatments, from 200 °C to 700 °C, the authors observed that the H_2 uptake capacity of TiO_2, V_2O_3, Nb_2O_5, and Ta_2O_5 supported nanoparticles decreased (to almost complete suppression) as the temperature of the reduction treatment increased. It was noticed that the chemisorption properties of MgO, Sc_2O_3, Y_2O_3, ZrO_2, and HfO_2 were kept unchanged. Tauster and Fung draw attention to the fact that the reducible oxides studied are saturated, thereby, formally having zero-*d*-orbital-occupancy before the reduction treatments. Although reducibility is a bulk property, the authors argue the importance of the reduction of the oxide surface (removing these zero-*d*-orbital-occupancy states) for the bondings on the metal-support interface and the occurrence of the SMSI effect. A few years later, Sadeghi and Henrich highlighted the impact on the reduction of the support towards the SMSI effect occurrence by probing the alterations on the electronic structure of an Rh thin film deposited over (i) a reduced TiO_2 single crystal and (ii) a fully oxidized TiO_2 single-crystal [60]. Through Electron Energy Loss Spectroscopy (EELS) measurements, the authors revealed a decrease in the occupation of Ti 3d electron level on the reduced TiO_2 (r-TiO_2) after depositing the Rh film. Later, the analysis of the Ti 2p X-ray Photoelectron Spectroscopy (XPS) region and the Ti LMV Auger transitions showed evidence that the Rh film oxidizes surface Ti ions through an electron transfer process. By means of Ultraviolet Photoelectron Spectroscopy (UPS), Sadeghi and Henrich verified that the Rh-Ti interaction is much stronger (ionic character) on the r-TiO_2 than in the fully oxidized TiO_2 surface, however, both samples presented similar results towards the CO chemisorption. The explanation for these results considers another feature of the SMSI effect: the geometrical factor.

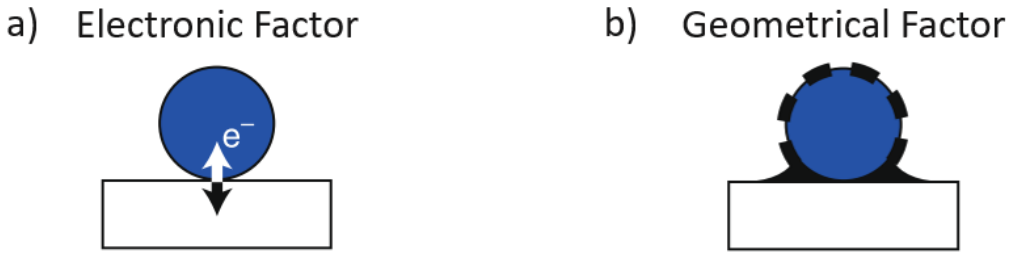

Figure 1.4 – Illustration representing the (a) electronic and (b) geometrical factors associated to the SMSI effect. (Image adapted from [61])

Together with the electronic phenomena, geometrical features were associated with the SMSI effect (both represented at Figure 1.4). Shortly after Tauster's studies, Santos and coworkers suggested that the alterations in reaction kinetics towards ammonia synthesis and the suppression of CO chemisorption capacity observed for Fe/TiO_2 should be associated with the migration of support's sub-oxides to metal nanoparticles' surface (encapsulation process) after a reduction treatment under H_2

atmosphere at 770 K [62]. While no change in surface Fe chemical state was detected on analysis of Mössbauer spectra collected on the samples, an expressive increase in the activation energy of the ammonia synthesis reaction was observed. The encapsulation hypothesis was considered but directly probed a few years later by Logan and coworkers through the observation of sub-oxide decoration layers on Rh/TiO_2 nanoparticles by means of High-Resolution Transmission Electron Microscopy (HRTEM)[63]. The authors observed that a low-temperature reduction (LTR, at 473 K) treatment in H_2 was not enough to induce such migration, but a high-temperature reduction (HTR, 773 K) induced the encapsulation of the Rh nanoparticles by amorphous layers of about 0.3 nm in thickness, as shown in Figure 1.5. They have also shown that a subsequent oxidation treatment (O_2) at 473 K was not able to clean the Rh surface, although restored the H_2 chemisorption capacity.

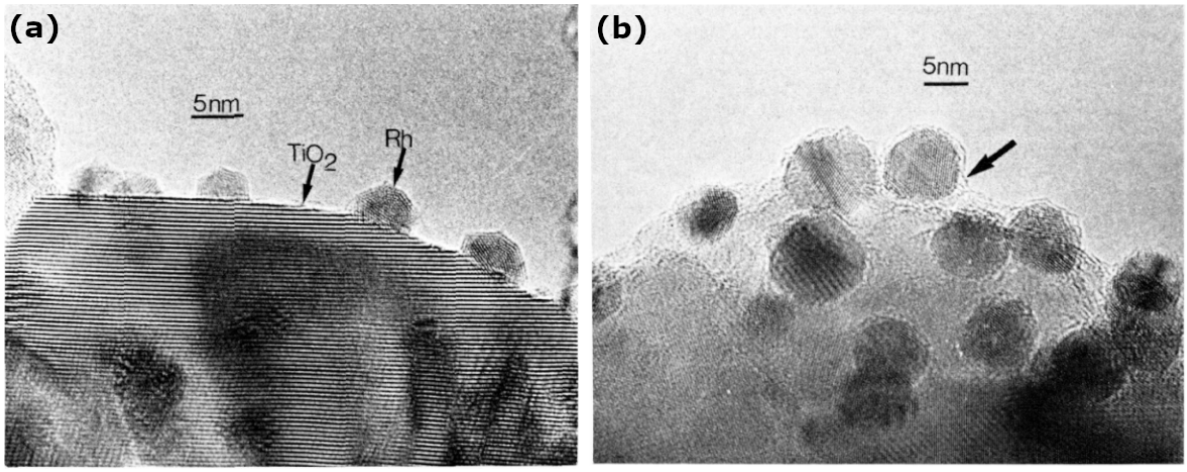

Figure 1.5 – HRTEM micrographs of Rh nanoparticles (darker gray) supported on TiO_2 after (a) LTR, and (b) HTR. It is possible to notice the presence of thin amorphous layers (arrowed) covering Rh nanoparticles and at the support at (b). (Image adapted from [63])

Despite the number of studies, the very limited access to *in situ* methods prevents the complete understanding of the mechanisms related to SMSI effect traits. On the literature, one can find much more information regarding the geometrical factor of the SMSI effect than on it's electronic feature [63–67], probably due to the possibility of the exploitation towards the avoidance of particles sintering [64–66] and unambiguous determination through the most distinct methods [63, 67–70]. Yet, pieces of evidence show that the electronic interactions which arise at milder reduction conditions impact more the catalysts' applicability than the presence of encapsulation layers over the metallic nanoparticles [63]. As the driving forces behind SMSI effect occurrence have not yet been explicit, further investigation is needed for the elucidation of the electronic entities involved in the interaction beginning.

On a previous work, our group mapped the surface electronic states involved on the electronic phenomena of the SMSI effect on Cu_xNi_{1-x}/CeO_2 (x = 0.25, 0.35, 0.60, 1.00) nanoparticles after reduction treatment (H_2 atmosphere, 500 °C) using *in situ* techniques [71]. Through Near Ambient Pressure (NAP) XPS measurements, the occurrence of the geometrical factor of the SMSI effect was evidenced in the Cu richer samples (x= 0.60, 1.00) by the strong decrease of the (Cu 2p + Ni 2p)/Ce 3d NAP-XPS intensity ratio during exposition to the reducing atmosphere, indicating the formation of encapsulation layers over the metallic nanoparticles. This encapsulation phenomenon was later confirmed by High-Resolution Transmission Electron Microscopy (HRTEM) measurements. Further, the comparison of contributions to the Ce 3d NAP-XPS region after H_2 and CO_2 high temperature treatments indicated disturbances in Ce electronic states during the SMSI effect. By detecting energy shifts at the Ce 3d components associated to the $Ce3d^{10}O2p^6Ce4f^1$ and $Ce3d^{10}O2p^6Ce4f^0$ states, it was possible to determine the Ce(III) and Ce(IV) states involved on the interaction with the Cu-Ni nanoparticles, as represented in Figure 1.6. *In situ* X-ray Absorption Near Edge Structure (XANES) measurements revealed also a decrease on the reduction temperatures for the Cu/CeO_2 and $Cu_{0.60}Ni_{0.40}/CeO_2$ nanoparticles in comparison to the non-supported ones. This observation was associated with a charge transfer process from support to the (bi)metallic nanoparticles. Later, the SMSI state was destroyed by exposing the systems to a high-temperature oxidizing treatment (CO_2 atmosphere, 500 °C). A strong correlation between the surface Cu concentration and the SMSI effect occurrence was observed, depicting a specimen threshold for starting the interaction. Density Functional Theory (DFT) calculations on a $Cu_2Ni_2{}^{cluster}/CeO_2{}^{slab}$ model evidenced the charge transfer process through the interaction of Cu and Ni *d* with apparent hybridized Ce-O states.

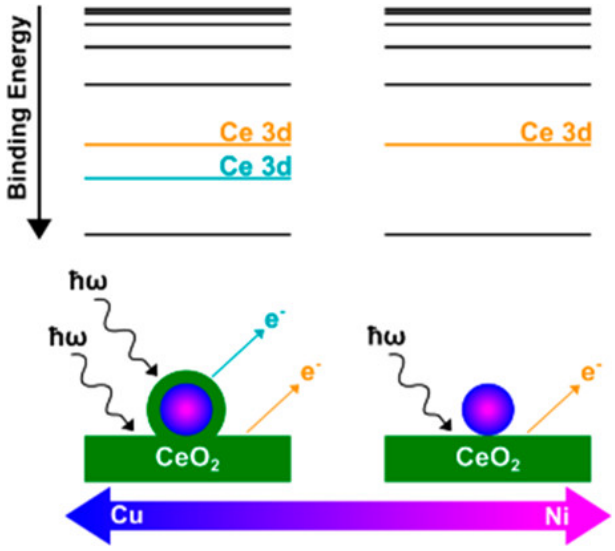

Figure 1.6 – Diagrammatic representation of the experimental mapping process of the Ce electronic levels responsible by the metal-support interaction on Cu_xNi_{1-x}/CeO_2 (x = 0.25, 0.35, 0.60, 1.00) nanoparticles. (Image from [71])

Since its discovery, the SMSI effect has been the focus of intense discussions in the catalysis community since there are several reports of enhancement and depression of systems catalytic activity. The depression of the catalytic activity is typically associated to the geometrical factor [69, 72], besides this effect may also improve the catalytic properties [64, 65, 69].

The ability to control the SMSI effect occurrence allows the tuning of the system's surface chemical/electronic properties, providing tools for the development of a new generation of catalysts. Recently, Bruix and coworkers have demonstrated that the electronic interaction between small particles of Pt and CeO_2 could strongly enhance (up to 20-fold enhancement) the catalytic activity for water-gas shift reaction, in comparison to pure Pt catalysts [73]. Through UPS measurements, the authors verified that supported Pt nanoparticles presented a much smaller density of states near the Fermi level in comparison to bulk Pt. DFT calculations revealed that the electronic interactions may disturb the charge distribution and the geometry of the particles, providing better sites for the adsorption of the H_2O molecules, lowering the energetic barrier for water dissociation, and stabilizing the formed OH and H products. Li and coworkers also worked on the exploitation of electronic metal-support interactions (EMSI) towards the tailoring of supported Pt catalysts properties towards the increase of its activity [74]. Using XAS, XPS, and Infrared (IR) spectroscopy measurements to characterize the electronic properties of Pt single atoms supported on Co_3O_4, CeO_2, ZrO_2, and graphene, the authors verified that strong EMSI phenomena on Pt/Ce_3O_4 induced a strong depletion of electrons from Pt 5d band. Such phenomena induced an increase in the system catalytic activity 68-fold in ammonia borane dehydrogenation. The Fourier transforms of the Extended X-ray Absorption Fine Structure (EXAFS) oscillations of the samples indicate that the metal does not agglomerate, as confirmed by Scanning Transmission Electron Microscopy (STEM) measurements. Further, DFT calculations indicated that the boost in the catalytic activity is due to the formation of Pt 5d empty states near the Fermi level, responsible to bind strongly the reactants but allowing its dissociation and release of the H_2 product.

According to the evidence presented above, the reports regarding the electronic phenomena around SMSI effects are associated with the disturbance of metal and oxide electronic structures due to charge transfer and/or chemical bondings at the metal-support interface [75]. Surveying the literature, physical and chemical considerations have been made for these interface interactions. Early discussions proposed that the heterojunction in the system's interface imposes the bending of the metal and the semiconductor energy bands due to an alignment of both Fermi levels [76, 77]. Then, it was suggested that interfacial states may appear, screening the semiconductor bands, and thereafter narrowing its band gap [78]. Further, the interface mid-gap states could be associated with the folding of the metal's conduction band into

the oxide band gap. The penetration depth of these metal bands into the oxide gap would then determine the direction of charge transfer phenomena [79]. Charge redistribution at metal-semiconductor interfaces could also be influenced by the formation of chemical bondings, according to the difference in materials electronegativity ($\chi_M - \chi_S$) [80]. As driving forces for electronic interactions are ruled by energy minimization processes and the law of continuity (imposed on the solids' electric potential) [81], charge transfer and diffusion occur through few atomic layers at the metal-support interface. The polarization at this interface can affect the electrons distribution on the metal and oxide orbitals. This electronic redistribution can be strong enough to promote the formation of depletion zones [82] or even the migration of oxide cations onto the metal particles' surface [67].

As stated above, many factors influence the electronic state at the metal/oxide interface. Therefore, determining the nature of electronic interactions in these systems is paramount for the development of sophisticated catalysts. While physical and chemical phenomena may disturb the electronic structure of the components present at the metal/oxide interface, such alterations reflected on interface and surface energies impact significantly the thermodynamic properties of nanostructured systems. In particular, Fu and coworkers indicated that dramatic phenomena such as the encapsulation present in the SMSI effect happen for metals of large work functions and surface energies, such as Pt and Pd, supported by reduced (or n-doped) oxides of small surface energies, such as TiO_2 and CeO_2 [67]. They state that high temperatures are required to activate transport phenomena responsible for the formation of the encapsulation layers, so such systems studied under reduction treatments at low temperatures may give important insights towards the electronic features of the SMSI effect.

1.3 Project Objective

Intending to investigate the disturbances on the electronic structure of the metal/support interface caused by the SMSI effect, systems composed of Pd nanoparticles supported on TiO_2, CeO_2 and Nb_2O_5 were scrutinized theoretically and experimentally. The experimental-computational approach applied comprises UPS and NAP-XPS measurements, for the characterization of the surface chemical state and electronic structure of the samples, and DFT calculations to gain insights into the interactions associated with the alterations in the electronic structure of the supported Pd nanoparticles involved in the SMSI effect.

The oxides chosen as support bear distinct electronic structures and have been used in prior studies presenting metal-support interaction reports. TiO_2 was chosen since it is the most studied support presenting the SMSI effect, thereby presenting also the better-understood phenomena. Yet, there are still open questions about the electronic effect at the atomic level. Further, Nb_2O_5 and CeO_2 also presents the SMSI effect, however presents less understood mechanisms and phenomena. It is desired to elucidate the SMSI effect on CeO_2 and Nb_2O_5 supported systems due to its high importance in catalysis [83, 84]. Using oxide supports of distinct chemical periods (4, 5, and 6, for the Ti, Nb, and Ce, respectively), this work search the answers to questions such as

- How do the SMSI effect disturbs the electronic structure of the metal/support interface?
- Are, in fact, chemical bonds formed at the metal/support interface?
- Which are the electronic entities associated to the electronic phenomena of the SMSI effect?

Elucidating these points, one will be able to predict the occurrence of electronic metal-support interactions, therefore shall have the capacity to tune the surface properties of nanostructured heterogeneous catalysts.

2 Physical Background on the Experimental and Theoretical Techniques

This chapter provides an assessment on each of the techniques applied for the characterization of the nanoparticles and the investigation of the metal-support electronic interactions, describing briefly the measurement (calculation) process, the typical equipment setup, and the signal detection.

2.1 Temperature-Programmed Reduction

Temperature-Programmed Reduction (TPR) is a thermoanalytical technique used for the characterization of chemical properties of solids, mainly applied for catalysis research [85]. Chemical information can be obtained by monitoring the change on the reducing gas conductivity, while the temperature of the system is driven. The method, introduced by Jenkins [86], is highly sensitive and depends only on the reducibility of the sample under investigation [87]. Usually, the solid sample is exposed to a hydrogen flow while altering its temperature and the gas conductivity is monitored before and after reducing the sample [85].

At the beginning of the TPR experiment, a fixed amount of the solid sample is exposed to a diluted amount of the reducing agent (typically 5% H_2 mixed with nitrogen or argon), controlled by a gas-handling system. Part of the gas passes directly through one of the arms of the thermal conductivity cell, as a reference, while the other part overspreads the reactor (heated linearly at a predetermined rate) before being detected on the other arm of the thermal conductivity cell. Comparing the signal detected in both arms, it is possible to observe changes in the gas concentration that indicates hydrogenation (H_2 uptake) or dehydrogenation (H_2 release). Such distinct processes show peak-like structures in the TPR profile.

2.2 Differential Thermal Analysis

Analogously to TPR, Differential Thermal Analysis (DTA) is a standard thermoanalytical method used to characterize chemical transformation on solid samples [88], employed since Le Chatelier [89].

DTA experiments require a simple experimental setup. Usually, the apparatus is composed of a furnace, where the sample holders for the studied and the reference samples are located, gauges for the control of the furnace heating rate and gas flux, and the electronics to record and amplify the probed signal.

During the measurements, a thermocouple probes the temperature difference (ΔT) between a sample and an inert material (reference) during a heating/cooling process. Evaluating the evolution of the signal associated with the temperature difference, it is possible to identify endothermic reactions (such as dehydration, melting and evaporation reactions, structural and magnetic transformations, and reduction) or exothermic reactions (e.g. reconstruction of crystalline structures, structural transformations, oxidation, and combustion) as the ΔT curve slope deviates downwards or upwards, as shown in Figure 2.1.

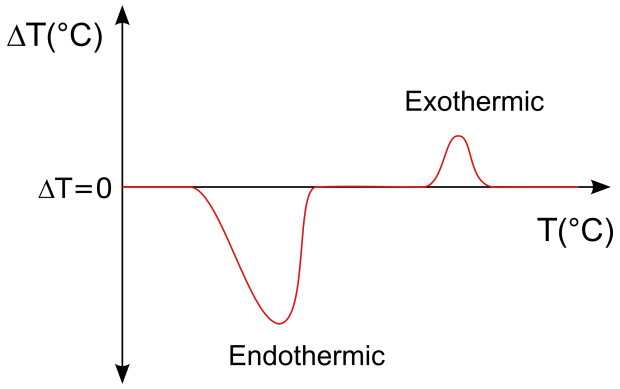

Figure 2.1 – Schematic representation of endothermic and exothermic events detected in a DTA curve.

Thermal events indicated as peak-like structures on DTA curves arise from the dynamics of the method [88]. When an event involving heat absorption occurs, the temperature difference between the sample and reference increases until such reaction is done, when the ΔT declines again. The analogous situation is found for the reaction with heat release. In this manner, each event raises a peak which allows the determination of properties such as the transformation temperature, heat of transformation (latent heat), and rate of transformation [90].

2.3 Transmission Electron Microscopy

Transmission Electron Microscopy (TEM) is a widely used method for the investigation of size and morphology in nanostructured materials, providing high spatial and analytical resolution [91].

Working similarly to the light microscopes, electron microscopes allow the investigation of nanometric structures due to the capacity to resolve parts as small as 0.01 nm (while light microscopes achieve resolutions of around 150 nm). Inside the microscope, these electrons, emitted by an electron gun, are collimated coherently by a series of electromagnetic lenses before striking the sample. After reaching the sample, the electrons of the incident beam are scattered at different angles depending on the thickness and electronic density of the sample. Thick and high-density obstacles shall deflect a high number of electrons, while thin and low-density obstacles allow the

transmission of a higher number of electrons. The transmitted beam is then refocused onto a detector (phosphorous screen or CCD camera) where a shadow image of the structures present on the sample is formed. Figure 2.2 shows a TEM image of $Au@Al_2O_3$ core-shell nanoparticles, where the darker region of nanoparticles is due to the higher electronic density of Au coated with a lighter gray region associated with the Al_2O_3 shell.

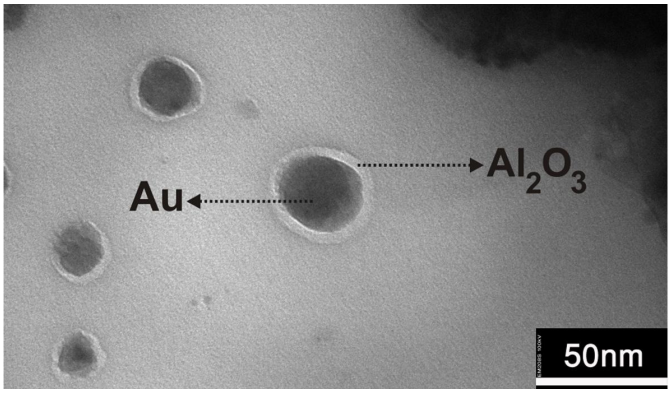

Figure 2.2 – TEM image of $Au@Al_2O_3$ core-shell nanoparticles. (Image from [92])

The electron beam used to obtain images raises secondary signals that can be used to gather chemical information of the samples. After scattering the incident electrons, atoms on the sample may become excited, and relax through the emission of characteristic X-rays, allowing the determination of atomic composition by Energy-dispersive X-ray Spectrometry (EDS) measurements. Besides that, by probing the energy loss of the electrons transmitted through the sample, it is possible to gather information about atomic composition, chemical compounds and electronic properties of the nanostructures with the Electron Energy-Loss Spectrometry (EELS) spectra.

2.4 Dynamic Light Scattering

Dynamic Light Scattering (DLS) technique is an experimental method that allows one to determine particles' size distribution profiles when these are suspended in a fluid. The method is based on the interpretation of the interaction between the incident light and the charges of a given particle.

Considering an electromagnetic wave of wavelength λ, linearly polarized, propagating in the x-direction, its electric field (Equation 2.1) may induce a distortion in the particles' spatial charge distribution. The electrons are shifted according to the external wave modulation, transforming the particle into an oscillating dipole, which scatters the incident wave elastically

$$E(x,t) = E_0 \left(sin\left(\frac{2\pi x}{\lambda}\right) + sin\left(\frac{2\pi c}{\lambda t}\right)\right) \tag{2.1}$$

The thermal density fluctuations of the fluid induce random (Brownian) motion of the diluted particles. Such motion cause temporal fluctuation in the particles' position and local concentration, resulting in the interference of the scattered waves. By studying the temporal dependence of the intensity of the scattered wave, one can quantitatively analyse the scattering particles' radii [93]. After measuring the scattered intensity ($I(q,t)$ shown in Figure 2.3), the signal is mathematically transformed into an *intensity autocorrelation function* by multiplying the time-dependent scattered intensity with itself after translating the signal by a τ time, and averaging the result over the complete measurement time interval. The autocorrelation function is then determined after calculating $\langle I(q,t)I(q,t+\tau)\rangle$ for different values of τ, usually from 100 ns to some seconds.

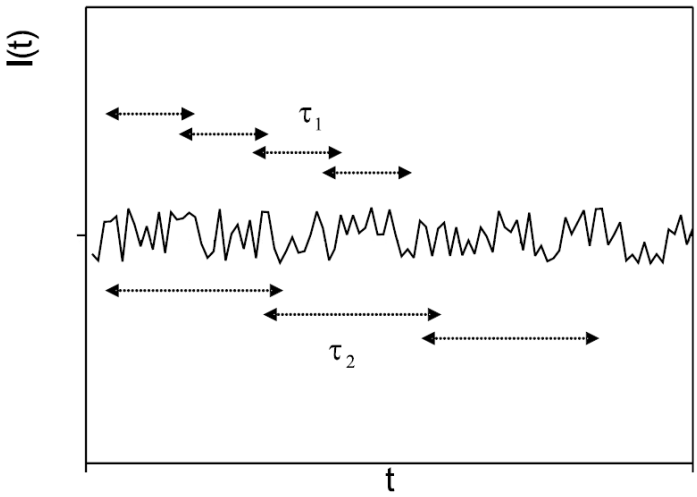

Figure 2.3 – Sketched intensity fluctuations and time intervals τ_1 and τ_2 used to calculate autocorrelation functions. (Image adapted from [93])

The intensity autocorrelation function is associated to the particles dynamic structure factor $F_s(q,\tau)$ by

$$F_s(q,\tau) = \sqrt{\frac{\langle I(q,t)I(q,t+\tau\rangle)}{\langle I(q,t)^2\rangle} - 1} \tag{2.2}$$

which can also be associated to their self-diffusion coefficient D_s by

$$F_s(q,\tau) = exp(-D_s q^2 \tau) \tag{2.3}$$

At the experimental conditions, the suspended particles diffuse through the fluid on a laminar flow. Such a regime allows the approximation of the self-diffusion coefficient using the Einstein-Stokes relation [94]

$$D_s = \frac{k_B T}{6\pi\eta R} \tag{2.4}$$

where k_B is the Boltzmann's constant, T is the sample temperature, η is the solvent dynamic viscosity, and R is the radius of the spherical particle (under Brownian motion).

Experimentally, three main parameters may interfere with the scattered intensity: (i) mass/size of scattering particles, (ii) particles concentration in the solution, and (iii) the difference between the refractive indices of the solute particles and the solvent. A properly prepared solution is inserted in a quartz glass cuvette (with usually 10 - 30 mm diameter). The most common setup uses single angle light scattering apparatus composed of an incident light source (typically a laser), the light scattering cell (such as a quartz glass cuvette), and a light detector (photomultiplier tube or avalanche photodiode) mounted on a goniometer, connected to the hardware for signal processing and analysis. Such setup is schematically represented in Figure 2.4.

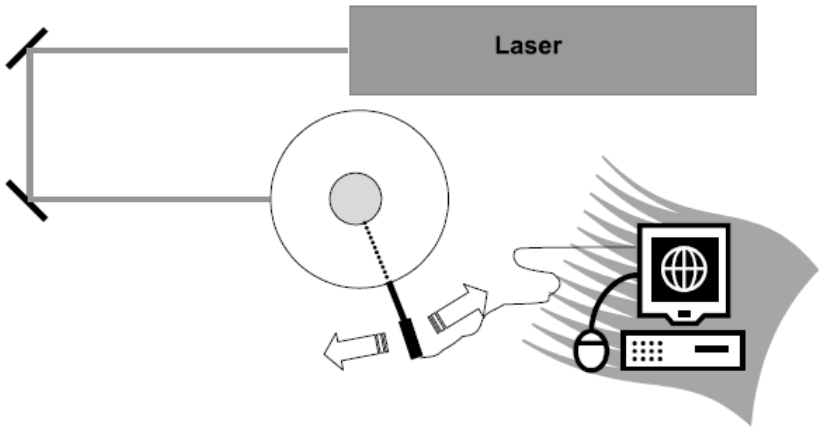

Figure 2.4 – Standard single angle light scattering setup viewed from the top. (Image from [93])

2.5 X-rays

In 1895, Röntgen related the discovery of a new type of radiation, of *unknown* nature, which he named "X-rays" [95]. Studying discharge tubes[1], Röntgen noted that this invisible radiation was capable to penetrate (and even trespassing) several objects, depending on their densities and thickness.

Formally, X-rays are defined as high-energy electromagnetic waves (frequently within the range from 200 eV to 1 MeV [96]), presenting wavelengths between 10^{1} nm and 10^{-4} nm. They may be produced by the deceleration of high kinetic energy electrons (*bremsstrahlung*). Inside discharge tubes, these high speed electrons may collide several times with the atoms of an anode target, decelerating. As the majority of this energy is converted into heat at the anode, less than 1% of the kinetic energy is responsible to produce a continuous wide spectrum of X-rays.

[1] Sealed glass tube, filled with a gas mixture at reduced pressure (about the normal air pressure at the sea level), and containing electrodes (cathode-anode) at its ends.

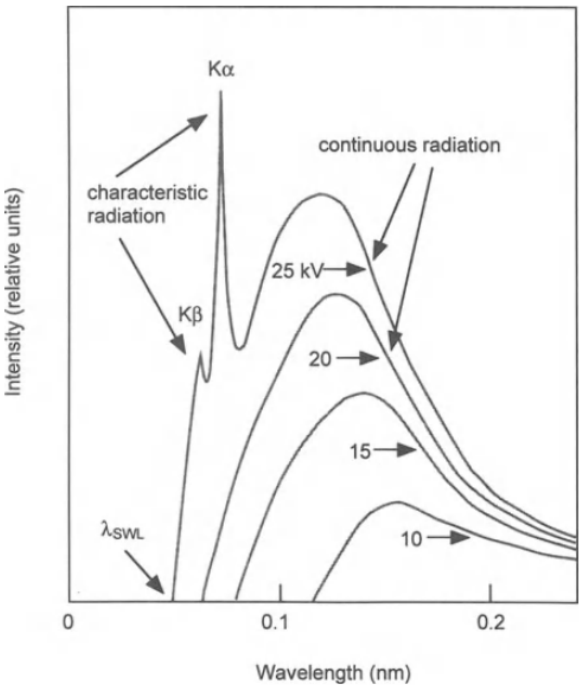

Figure 2.5 – X-ray spectra of $_{42}$Mo at different accelerating potentials. The characteristic radiation features are not to scale. (Figure extracted from [96])

Figure 2.5 shows examples of X-ray spectra from a Mo anode produced by applying different potentials on the cathode-anode system. The shorter wavelength (λ_{SWL}) present on this spectrum corresponds to the X-ray photons produced by the total conversion of the electron kinetic energy into radiation, while the other wavelengths correspond to photons resulting from scattered electrons. The maximum energy (E) of the emitted X-rays can be related to the accelerating potential (V) on the discharge tube by

$$eV = E = \frac{hc}{\lambda} \tag{2.5}$$

from where it is possible to determine $\lambda_{SWL} = hc/eV$. This relation makes it easy to notice that by increasing the accelerating potential, λ_{SWL} decreases as shown in Figure 2.5. Notwithstanding, increasing the potential V leads to a new phenomenon associated with the appearance of narrow and intense lines at specific wavelengths. These lines, known as characteristic lines, appear when the electrons accelerated by the potential U have enough energy to eject (after a collision) a core electron bounded to one of the atoms of the anode target. The ionization leaves the atom excited due to the electronic hole on an inner shell. A possible atomic relaxation process occurs by filling the hole on the inner shell with an outer-shell electron and emitting an X-ray photon of energy equal to the energetic difference of the levels involved in the relaxation process. These characteristic X-rays are labeled according to the shell from which the core-electron is ejected — K, L, M, ... — and classified with respect to the shells distance — α for first neighboring shells (L $\rightarrow$ K); β for second neighboring shells (M $\rightarrow$ K); γ for third neighboring shells (N $\rightarrow$ K).

The intensity (I) of an X-ray spectrum can be related to the anode target composition by

$$I = AiZV^2 \tag{2.6}$$

where A is a proportionality constant, i is the electrons current inside the discharge tube, Z is the atomic number of the anode target, and V is the charges accelerating potential. Analogously, the intensity of an X-ray characteristic line (I_{line}) can be related to the ejected electron shell S as

$$I_{line} = Ci(V - U_S)^n \tag{2.7}$$

where C and n are proportionality constants (specific for each shell), and U is the anode's electron-atom binding energy for the S shell. From Equation 2.7 it is possible to notice that the most intense lines are the K set, since these comes from the ionization of the inner-most shell (thereby most bounded electrons). Experimentally, the most common X-ray sources are Cu K_α ($\lambda = 0.1541$ nm), Mo K_α ($\lambda = 0.0711$ nm), Cr K_α ($\lambda = 0.2291$ nm), Al K_α ($\lambda = 0.8339$ nm), and Mg K_α ($\lambda = 0.9889$ nm).

2.6 X-ray Diffraction

The X-ray diffraction (XRD) analysis is an experimental technique used primarily for the determination of a material crystal structure. It is a non-destructive technique that allows the precise identification of the crystal phase, lattice parameters, strain, and crystallite size.

As shown by Max von Laue, the X-rays radiation wavelength is extremely convenient for producing X-rays diffraction patterns on crystalline materials [97]. Investigating the scattering of X-rays on a copper sulfate crystal, he and his coworkers identified the condition for constructive interference of the x-rays scattered, which is a momentum conservation law of the x-ray beam [98]. Such a discovery was proven to be so relevant that yielded von Laue a Nobel Prize in Physics. After von Laue's discoveries, W. L. Bragg independently showed the same phenomenon with an alternative mathematical equation [99]. He noticed that the intensity of the scattered radiation depends on the radiation's angle of incidence. Such phenomenon was translated on a relation between the X-rays beam incident angle and the crystal's structure given by

$$2\,d\,sin(\theta) = n\,\lambda_i \tag{2.8}$$

where d designates the distance between the atomic planes (experimented by the incident X-rays), θ is the X-rays incidence angle with respect to the atomic plane, λ_i is the incident X-ray wavelength, and n is an integer related to the reflection order.

Equation 2.8, known as "Bragg's law" (or "Bragg's condition"), schematized in Figure 2.6, indicates that there is a constructive interference between scattered x-rays if the optical path difference is an integer multiple of their wavelength, i.e. $\delta = n\lambda$. Observing Figure 2.6, one can notice that CD and CC' integrate wavefronts, thereafter, the path difference δ between them is $DE + EC' = 2EC'$. Using trigonometric relations on the triangle CEC', is possible to observe that $\delta = 2d'sin(\theta)$, where the Equation 2.8 is recovered.

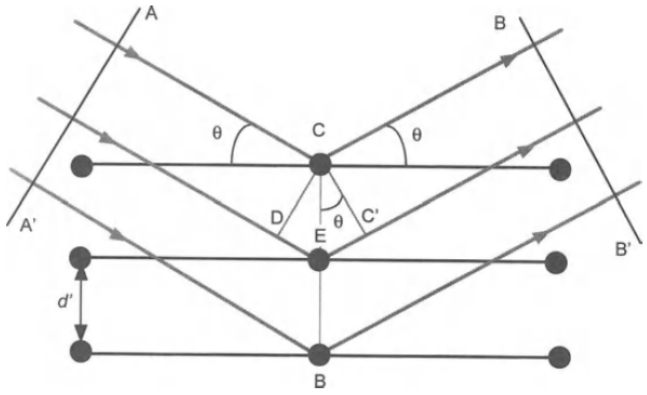

Figure 2.6 – Schematic diagram representing the Bragg's condition for diffraction in crystals. (Image from [96])

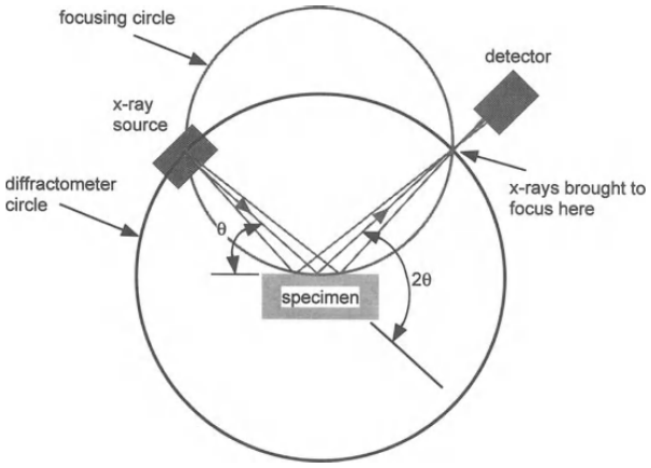

Figure 2.7 – Schematic representation of the arrangement of the components on an X-ray diffractometer. (Image from [96])

The experimental setup for a diffractometer may present distinct features depending on the manufacturer, however, an instrument presents three main components: an X-ray source, the sample holder, and the X-ray detector. These three components lie in an arrangement of two structures known as the focusing circle and the diffractometer circle (also known as the goniometer circle). Figure 2.7 shows the most common diffractometer geometry, known as θ-2θ, where θ is the angle between the

X-rays source and the plane of the sample holder (containing the specimen), while 2θ is the angle between the incident and scattered X-rays. At this geometry setup, the X-rays source is kept fixed while the sample holder and the detector are moved to collect the scattered radiation through a range of angles. During these measurements, the radius of the focusing circle increases as 2θ increases.

Conventional diffractometers use radiation from a X-ray tube to probe the structural properties of a crystalline sample. As the detector surveys the intensity of the scattered radiation through the angular range, one identifies the formation of a pattern composed of a series of peaks of distinct intensities, as shown in Figure 2.8. These peaks correspond to the constructive interference of diffracted X-rays at specific sets of planes and thereafter are referred to as "Bragg reflections". These reflections' absolute intensities bear a convolution of several experimental parameters (such as diffractometer optics, and current and voltage used in the X-rays source) and are not of great interest, however, the relative intensities can be evaluated to obtain information regarding atomic positions in a crystal, ordering (long-range), and relative proportion of phases in multi-component samples. Further, the width of the Bragg reflections can be used for the determination of crystallite size, and study lattice distortions.

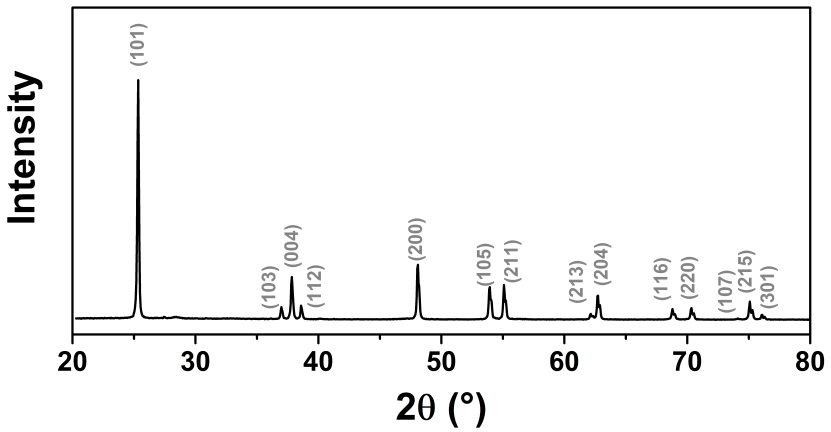

Figure 2.8 – X-ray diffraction pattern of a TiO_2 powder sample. The Bragg reflections are identified with Miller indices.

Since XRD analysis provides detailed information about atomic structures, it is a fundamental tool for catalytic applications, where materials are usually designed at the nanoscale. Through the comparison of a diffraction pattern with those from digital databases, such as the files from the International Centre for Diffraction Data (ICDD), one can easily identify a compound and its crystal phase. Further, computational methods have been developed for the quantitative analysis of materials structures. For powder diffraction analysis, the most reliable quantitative method is the one developed by H. Rietveld [100], in which instrumental and structural parameters are determined by fitting the experimental data with a calculated profile. Such an elegant technique,

limited basically to the instrumental resolution, can also determine precisely the structures of organic and metal-organic frameworks, proteins, and macromolecules.

The Rietveld refinement method is based on a nonlinear least-squares minimization process of the Φ function

$$\Phi = \sum_{i=1}^{n} w_i (Y_i^{obs} - Y_i^{calc})^2 \tag{2.9}$$

in which Y_i^{obs} is the observed and Y_i^{calc} is the calculated intensities of each point i from the diffraction pattern, w_i is the weight associated to the ith point, and the summation is made over all measured (n) points [101]. The calculated intensity term at Equation 2.9 can be rewritten as

$$Y_i^{calc} = b_i + K \sum_{j=1}^{m} I_j y_j(x_j) \tag{2.10}$$

where b_i is the background calculated for the ith point, K is a scale factor for the crystal phase, m is the number of Bragg reflections contributing to the intensity at the ith calculated point, I_j is the intensity of the jth Bragg reflection, and $y_j(x_j)$ is the peak-shape function (usually, a pseudo-Voigt peak with an asymmetry correction [102]). When the material is composed of more then one crystal phase, the $K \sum_j I_j y_j(x_j)$ term is summed over each phase.

2.7 X-ray Photoelectron Spectroscopy

X-ray Photoelectron Spectroscopy (XPS) is a premiere technique for materials science, allowing detailed investigation of the surface chemistry of materials through the determination of elemental composition, chemical state of these elements, and their concentrations [103].

The technique consists on probing the kinetic energy of photoelectrons ejected from atomic core levels, after the absorption of a X-ray photon. According to the photoelectron effect, the kinetic energy T of ejected photoelectrons is

$$T = h\nu - \phi_{sample} - E_b \tag{2.11}$$

where $h\nu$ is the energy of the incident X-ray photons, ϕ_{sample} is the sample work function, and E_b is the binding energy to the atom (with respect to the Fermi level) of the ejected photoelectron. For the measurements, the sample is grounded to the spectrometer's electron analyser so their Fermi levels get aligned, allowing Equation 2.11 to be rewritten as

$$T = h\nu - \phi_{analyser} - E_b \tag{2.12}$$

Equation 2.12 shows that by analysing the photoelectron kinetic energy, one can determine its binding energy since the incident photon energy is well defined by the selected radiation source and the analyser work function is known. Electrons from atomic inner levels will be ejected with less kinetic energy than those from outer levels since their binding energy are greater (as illustrated in Figure 2.9)

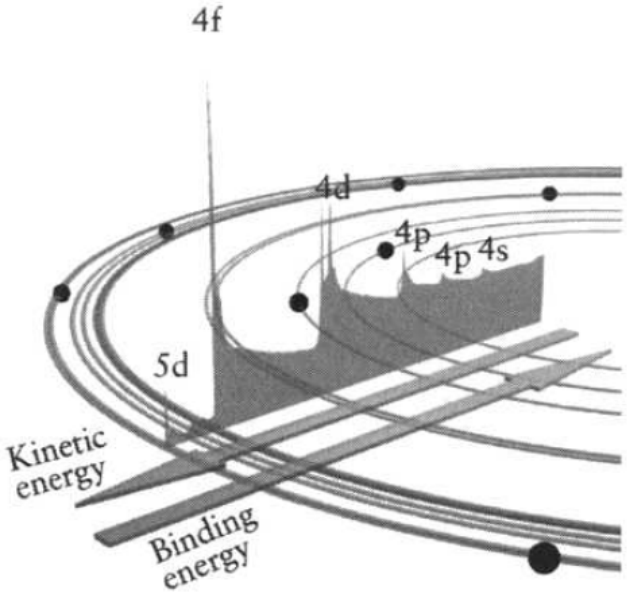

Figure 2.9 – Illustration of a lead sample's photoelectron spectrum, superposed with atomic orbitals, depicting the correlation between the kinetic and binding energy of photoelectrons. It is shown that photoelectrons from specific levels give rise to sharp peaks and may contribute to inelastic background due to energy loss processes. (Image from [103])

During the photoemission process, the electrons that escape the sample without any energy loss contribute to characteristic peaks at the XPS spectrum. (as shown in Figure 2.9). At the same time, some electrons scatter inelastically and contribute to the background of the spectrum. After the ejection, a 'hole' is left at the parent atom core level. As outer shell electrons rapidly refill these inner levels, the binding energy difference between these levels may be enough to allow the atom to eject a secondary electron during its relaxation. The kinetic energy of these secondary electrons (also called Auger electrons) depends only on the energy difference of the atomic levels involved in the relaxation process and thereafter are labeled over these specific shells (i.e. KLL Auger electron was bound to a L shell before being ejected after another L shell electron fill the K shell hole left by the photoelectron emitted). Further, since the kinetic energy of Auger electrons does not depend on the energy of the incident X-rays, changing the radiation source allows easy detection of a photoelectron or Auger peak since the kinetic energy of the photoelectron changes in accordance to Equation 2.12. While Auger emissions are favored for lighter atoms (low atomic number), heavier specimens usually relax through the emission of X-rays instead of electrons.

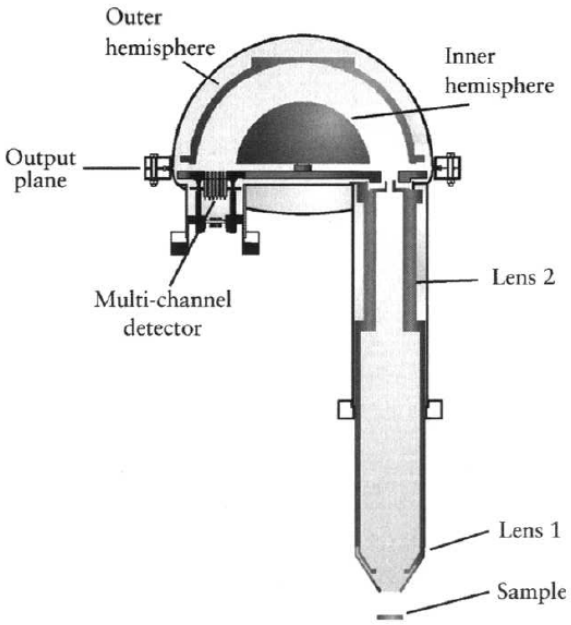

Figure 2.10 – Schematic diagram of a hemispherical sector analyser. (Image from [103])

The analysis of the photoelectrons is most commonly performed by using a Hemispherical Sector Analyser (HSA), as shown in Figure 2.10. The ejected photoelectrons are focused by a series of lenses before reaching the HSA, where they pass through the gap between the pair of concentric hemispherical electrodes. A potential difference is applied across these hemispheres (with the outer being more negative than the inner), setting a circular path for the electrons that reach the analyser. Controlling the kinetic photoelectron energy by using a retarding potential before HSA, one can select the electrons that will reach the detector since those whose kinetic energy is higher (lower) than the desired shall follow a path with too large (small) radius and collide at the outer (inner) hemisphere before being detected. As the photoelectrons reach the detector, a photomultiplier coupled to a multichannel collector emits several secondary electrons in a cascade effect, increasing the signals about 10^8 times, then creating a current recorded as the electrons are counted. The electrons spectrometer associates the electrons count to the correspondent binding energy.

The photoelectrons ejected from atoms closer to the surface have a bigger probability to be detected before scattering on another sample's atoms. Those ejected at deeper atoms in the sample have a bigger probability to be inelastically scattered before escaping the sample. Usually, the reference distance of the photoelectrons contributing to an XPS spectrum is the inelastic mean free path (λ_{IMFP}) of electrons, which depends on their kinetic energy as shown by the universal curve trend presented at Figure 2.11. About 65% of the total XPS signal comes from electrons ejected from depths of less than λ_{IMFP}, and 95% from depths $< 3\lambda_{IMFP}$.

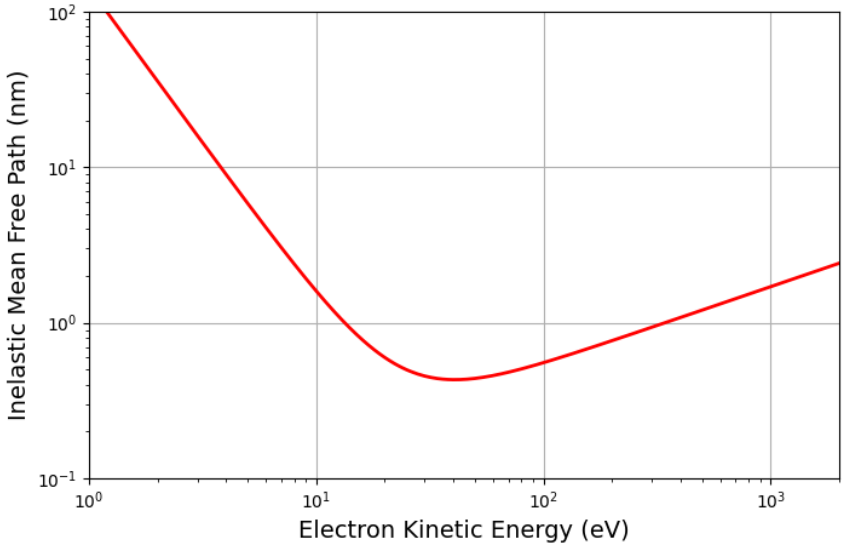

Figure 2.11 – Universal curve for the inelastic mean free path of electrons in elements, according to Seah and Dench [104].

The intensity of the recorded spectrum depends on apparatus parameters (such as photons flux, detector efficiency, and angle of collection of the photoelectrons) and samples' parameters (photoionization differential cross-section, atomic concentration, and depth from sample's surface). Such dependence can be written as

$$I_n = F_X \cdot \frac{d\sigma_n}{d\Omega}(h\nu) \cdot D_{ef}(T_n) \cdot \int_0^{\infty} \rho(z) \exp -\frac{z}{\lambda_{IMFP}(T_n) \cdot cos(\theta)} \tag{2.13}$$

where I_n is the intensity of a peak related to photoelectron ejected from the atomic level n, F_X is the X-rays flux, $\frac{d\sigma_n}{d\Omega}(h\nu)$ is the differential photoionization cross section for incident photons of $h\nu$ energy, $D_{ef}(T_n)$ is the detector efficiency at T_n energy, z is the depth from which the electron was ejected, $\rho(z)$ is the concentration per volume unit of its parent atom at z depth, $\lambda_{IMFP}(T_n)$ is the respective inelastic mean free path of a electron with T_n kinetic energy, and θ is the angle of the electron emission with respect to the sample's surface normal [105].

Conventional XPS setups require ultra-high vacuum (UHV) conditions for carrying out measurements in safety and avoiding surface contamination due to scattering of gas molecules in the sample-detector path. Nevertheless, the study of catalysts under ex-situ conditions may provide incomplete information on the electronic and structural properties of the studied systems which are applied for operation under high temperatures and pressures. Recently, developments in the instrumentation allowed the spectrometers to operate in situ (in high pressures and temperatures, named as Near-Ambient Pressure XPS measurements), defining the state-of-the-art in surface characterization of catalysts. The technique availability is still very limited, and its setups in usually associated with synchrotron facilities, where a thin membrane

(typically of Si_3N_4) or through a differentially pumped system is used to protect the vacuum in the beamline, allowing the passage of the X-ray beam into the analysis chamber but sustaining a pressure difference of about 10^9 between the analysis chamber and the storage ring. In the analysis chamber, the sample surface is brought very close to a differentially-pumped aperture that connects the electron analyzer to the chamber, allowing the sample to remain in an ambient of tens of millibar pressure while the measurements are conducted [106, 107].

2.8 Ultraviolet Photoelectron Spectroscopy

The Ultraviolet Photoelectron Spectroscopy (UPS), similarly to the XPS technique, is a method for the study of surface properties of materials [108]. As for XPS, the UPS measurements rely on the measurement of the kinetic energy of electrons ejected from a sample after the incidence of a radiation beam. The main difference is that ultraviolet sources provide much less energy, restricting the ejection of the electrons on atomic valence bands at the surface. These photoelectrons are ejected with a kinetic energy T of

$$T = h\nu - E_b - \phi_{sample} \tag{2.14}$$

where $h\nu$ is the energy of the ultraviolet source, E_b is the electron binding energy to the atoms valence band, and ϕ_{sample} is the sample work function. The recorded photoelectrons contribute peaks on the UPS spectrum associated with each orbital they occupied. Further, during the ionization of the sample, vibration and/or rotational states may be excited, shifting the kinetic energy of the photoelectron as

$$T = h\nu - E_b - E_{vib,rot} - \phi_{sample} \tag{2.15}$$

and the presence of these additional lines constitute orbital bands.

Each band present on an UPS spectrum corresponds to ejections of a single orbital. At the same time, each orbital (of given binding energy) probed by the measurement give rise to a single band. Thereafter, the analysis of an UPS spectrum allows the study of the valence state of the sample surface. Figure 2.12 shows the evolution of the electronic structures on the valence band throughout the deposition of Pd monolayers over a MgO film, where one can observe the variation in the intensities of O 2p and Pd 4d overtime.

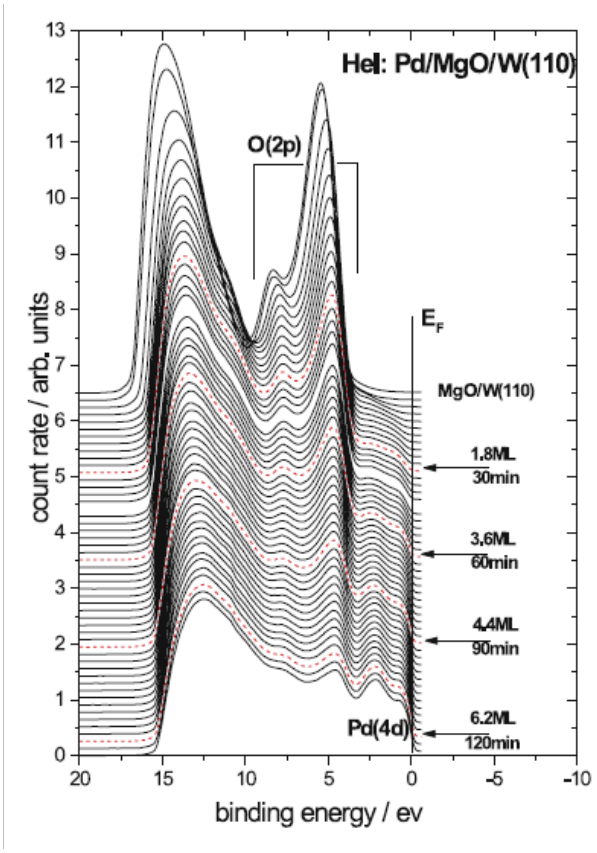

Figure 2.12 – UPS (He I) spectra for Pd on MgO as a function of the metal monolayers deposition on the oxide. The oxide O 2p and the metal Pd 4d bands are indicated on the figure. (Image adapted from [109])

The most used radiation for UPS measurements is that produced by electrical discharge in a pure helium lamp, which gives rise to He I ($h\nu = 21.2$ eV, $\lambda = 58.43$ nm) and He II ($h\nu = 40.8$ eV, $\lambda = 30.38$ nm) resonance lines. Although the intensity of the He I line is greater than the He II one (about 100x), the latter allows probing complete valence shells.

Since the UPS measurements probe only the outermost atomic layers of a sample, high vacuum conditions are extremely necessary to ensure the analysis of the sample surface. Pressures of 10^{-6} torr allow the deposition of one monolayer of ambient gas per second over the sample surface, so it is mandatory to achieve pressures of at least 10^{-9} torr (which takes around fifteen minutes for the deposition of a gas monolayer).

The absolute intensities of the peaks in UPS spectra can be disregarded since they depend on a convolution of physical and experimental factors which are usually not precisely known. On the other hand, the relative intensities of these structures are meaningful, as they are related to ionization cross-sections and proportional to the number of electrons available for the ionization [108].

2.9 Density Functional Theory

Density functional theory (DFT) provides powerful tools to compute and describe the quantum state of many-particle systems, such as molecules and solids. It provides a sophisticated approach to the theory of electronic structure, changing the paradigm of the many-particle wave function determination to the computation of the electron density distribution $n(r)$ [110].

The first approach to electron density functional theories dates back to the early attempts to solve the Schrödinger's quantum mechanical wave equation for systems with a large number of electrons. Thomas[111] and Fermi[112] developed a statistical model in which the Coulombian interactions between electrons (treated as a gas) induce their rearrangement around positive charges, so the system's total energy is minimized. At the same time, Hartree [113] developed a model to solve the quantum problem by approximating the many-particle wave function ($\Psi(r_i)$) by a product of single-particle wave functions ($\psi(r_i)$), i.e.,

$$\Psi^H(r_1, \cdots, r_N) = \prod_{i=1}^{N} \psi_i(r_i) \tag{2.16}$$

Shortly after, Fock upgraded Hartree's theory by including a spin coordinate in the single-particle wave function [114], adapting Hartree's equations to the anti-symmetry principle [115]. Such consideration was implemented by rewriting the electronic Coulombian repulsion in two terms: a one-electron averaged interaction, associated with the *charge density*, and a two-electron *exchange* interaction. This exchange interaction incorporates the electron's orbitals symmetries, implicitly including the spin on the calculation. The spin consideration made the Hartree-Fock method equivalent to the Thomas-Fermi's method whereas both describe the electron's motion as independent of all the others electrons in the system. By these means, Fock suggested rewriting Hartree's wave functions (Ψ^H) as a linear combination of orbital wave functions (χ_i). These orbital wave functions can be expressed as

$$\chi_i(\mathbf{x}_i(r_i, w_i)) = \phi(r_i)\alpha(\omega_i) \tag{2.17}$$

where $\phi(r_i)$ describes the orbital spatial distribution, and $\alpha(\omega_i)$ is the orbital spin functions.

The Tomas-Fermi and Hartree-Fock theories influenced the development of most of the work on the electronic structure of solids in the following years. In the mid-'60s, Hohenberg and Kohn developed a method to rigorously compute ground-state properties of an interacting system by using its electronic density distribution [116].

Hohenberg-Kohn theory is based on a lemma which states that the ground-state electron density, $\rho_0(r)$, uniquely determines the potential V_{ext} (within an additive constant) [117]. This lemma also states, as a corollary, that the ground-state density determines all of the properties of the system. In variational formalism, Hohenberg-Kohn's theorem can be equated as

$$E[\rho(\mathbf{r})] = \int V_{ext}\rho(\mathbf{r})dr + F[\rho(\mathbf{r})] \tag{2.18}$$

where the energy $E[\rho(\mathbf{r})]$, associated to a given potential V_{ext}, has an unique minimum for $\rho(\mathbf{r}) = \rho_0(\mathbf{r})$. The functional $F[\rho(\mathbf{r})]$ is defined as

$$F[\rho(\mathbf{r})] = T[\rho(\mathbf{r})] + V_{Coul.}[\rho(\mathbf{r})] = \langle \Psi_{\rho(\mathbf{r})}|T + U|\Psi_{\rho(\mathbf{r})}\rangle \tag{2.19}$$

where $\Psi_{\rho(\mathbf{r})}$ is the ground state wave function associated to the density $\rho(\mathbf{r})$, and T and $V_{Coul.}$ are respectively the kinetic energy and the Coulombian potential operators.

Briefly after the publication of Hohenberg-Kohn's theory, Kohn and Sham [118] developed a self-consistent algorithm to find the true electron density $\rho(\mathbf{r})$ using a set of single-particle equations

$$\left(-\frac{\hbar^2}{2m_e}\nabla^2 + V_{eff}(\mathbf{r})\right)\psi_i(\mathbf{r}) = \epsilon_i\psi_i(\mathbf{r}) \tag{2.20a}$$

$$\rho(\mathbf{r}) = \sum_{i=1}^{N}|\psi_i(\mathbf{r})|^2 \tag{2.20b}$$

$$V_{eff}(\mathbf{r}) = V_{ext}(\mathbf{r}) + \int \frac{\rho(\mathbf{r}')}{|\mathbf{r}-\mathbf{r}'|}d\mathbf{r}' + V_{XC} \tag{2.20c}$$

where V_{XC} is a potential called the local exchange-correlation potential, responsible to account the quantum effects associated to the spin inclusion, defined as

$$\begin{cases} V_{XC} & = \frac{\delta E_{XC}}{\delta\rho(\mathbf{r})} \\ E_{XC} & = F[\rho(\mathbf{r})] - \frac{1}{2}\int \frac{\rho(\mathbf{r})\rho(\mathbf{r}')}{|\mathbf{r}-\mathbf{r}'|}dr' - T_{n.e}[\rho(\mathbf{r})] \end{cases} \tag{2.21}$$

with $T_{n.e}[\rho(\mathbf{r})]$ describing the kinetic energy of a system with non-interacting electrons on the ground state density $\rho(\mathbf{r})$.

Using Kohn-Sham equations, it is possible to determine the correct electron density $\rho(\mathbf{r})$ by using the following algorithm:

1. Define an ansatz for the electron density $\rho'(\mathbf{r})$
2. Solve the Kohn-Sham equations for the defined $\rho'(\mathbf{r})$, determining a single particle wave function $\psi_i'(\mathbf{r})$
3. Calculate the Kohn-Sham electron density associated to $\psi_i'(\mathbf{r})$ according to $\rho_{KS}(\mathbf{r}) = 2\sum_i \psi_i'^*(\mathbf{r})\psi_i'(\mathbf{r})$
4. Compare the calculated electron density $\rho_{KS}(\mathbf{r})$ with the initial ansatz. If both densities are equal, then this is the ground state electron density and it is used to compute the system's energy (and other properties). Otherwise, the ansatz must be updated, restarting the calculations from item 2.

The Kohn-Sham equations are *in principle* exact, however, they need an explicit form for $V_{XC}(\mathbf{r})$ to be solved. Since the exchange-correlation potential expression is unknown (a priori), approximations of $V_{XC}(\mathbf{r})$ are used to solve Equation 2.20. The two most used approximations for the exchange-correlation potentials are the local density approximation (LDA) and the generalized gradient approximation (GGA). LDA potentials consider an uniform electron gas model allowed to move through the positively charged background described by the atoms' cores in such a way that the system is electrically neutral. GGA potentials, on the other hand, account for the inhomogeneity of the charge density. LDA and GGA exchange-correlation energy functionals can be expressed as

$$E_{XC}^{LDA}[\rho(\mathbf{r})] = \int \rho(\mathbf{r})\epsilon_{XC}(\rho[\mathbf{r}])d\mathbf{r} \tag{2.22a}$$

$$E_{XC}^{GGA}[\rho_+(\mathbf{r}), \rho_-(\mathbf{r})] = \int \epsilon_{XC}\Big(\rho_+(\mathbf{r}), \rho_-(\mathbf{r}), \nabla\rho_+(\mathbf{r}), \nabla\rho_-(\mathbf{r})\Big)d\mathbf{r} \tag{2.22b}$$

where $\epsilon_{XC}(\rho[\mathbf{r}])$ is the exchange-correlation energy per electron on the gas, and the subscripted indexes "+" and "−" indicate the distinct spins in the system.

Through the application of DFT, one can determine materials' electronic structure, interaction sites for gas adsorption with respective sorption, diffusion, activation, and reaction energies with an outstanding agreement with the state-of-the-art experimental results. Despite such predictive power, DFT calculations' accuracy is limited in some situations. One of these is for the determination of electronic excited states. Such limitation is expected from the Hohenberg-Kohn theorem, which is only applied for ground-state energies, and thereafter the extension of the calculations for excited states must be carefully evaluated. Other well-known limitations for DFT

calculations regard the underestimation of band gaps in semiconductors and insulating materials [119], and the determination of weak van der Waals interaction between atoms and molecules [120].

The fast increase of importance on the design of nanostructured materials was strongly supported by the improvement on the computational resources available for materials scientists as by the introduction of numerous DFT software distributions (e.g. Quantum ESPRESSO [121], VASP [122], SIESTA [123], CASTEP [124], ABINIT [125], ORCA [126], and Gaussian [127]).

3 Academic realizations

During the period 2017-2022, in which this doctoral work was carried out, the author participated in the production of scientific papers and had works presented in congresses.

Papers published correlated to the thesis:

- W.T. Figueiredo, R. Prakash, C.G. Vieira, D.S. Lima, V. E. Carvalho, E.A. Soares, S. Buchner, H. Raschke, O.W. Perez-Lopez, D.L. Baptista, R. Hergenröder, M. Segala, and F. Bernardi. New insights on the electronic factor of the SMSI effect in Pd/TiO_2 nanoparticles. *Applied Surface Science*, 574, pp. 151647, 2022.

Papers published uncorrelated to the thesis:

- W.T. Figueiredo, G.B. Della Mea, M. Segala, D.L. Baptista, C. Escudero, V. Pérez-Dieste, and F. Bernardi. Understanding the Strong Metal–Support Interaction (SMSI) Effect in Cu_xNi_{1-x}/CeO_2 ($0<x<1$) Nanoparticles for Enhanced Catalysis. *ACS Applied Nano Materials*, 2(4), pp. 2559-2573, 2019.

- W.T. Figueiredo, C. Escudero, V. Perez-Dieste, C.A. Ospina, and F. Bernardi. Determining the Surface Atomic Population of Cu_xNi_{1-x}/CeO_2 ($0<x1$) Nanoparticles during the Reverse Water–Gas Shift (RWGS) Reaction. *The Journal of Physical Chemistry C*, 124(31), pp. 16868-16878, 2020.

- A.S. Thill, W.T. Figueiredo, F.O. Lobato, M.O. Vaz, W.P. Fernandes, V.E. Carvalho, E.A. Soares, F. Poletto, S.R. Teixeira, and F. Bernardi. New horizons in photocatalysis: the importance of mesopores for cerium oxide. *Journal of Materials Chemistry A*, 8(46), pp. 24752-24762, 2020.

Works presented in congresses:

- Talk - Elucidating catalytic events at the atomic level in Cu_xNi_{1-x}/CeO_2 ($0<x<1$) nanoparticles - *XVI Brazilian MRS meeting* - Brazilian Materials Research Society, Gramado (Brasil), 2017.

- Talk (presented by F. Bernardi) - Elucidating atomic events in Cu_xNi_{1-x}/CeO_2 ($0<x<1$) bimetallic nanoparticles - *17th European Conference on Applications of Surface and Interface Analysis (ECASIA)* - Le Corum, Montpellier (França), 2017

- Talk (presented by F. Bernardi) - Strong Metal Support Interaction (SMSI) in Cu_xNi_{1-x}/CeO_2 Nanoparticles - *5th Annual APXPS Workshop* - Fritz-Haber-Institut der Max-Planck-Gesellschaft, Berlin (Alemanha), 2018.

- Talk - In situ characterization of CuxNi1-x/CeO2 ($0 < x < 1$) nanoparticles applied to the RWGS reaction - *28th Annual Users Meeting (RAU)* - LNLS, Campinas (Brasil), 2018.

- Poster - Enlightening the influence of the Strong Metal-Support Interaction (SMSI) - *European Congress and Exhibition on advanced materials and processes (EUROMAT) 2019* - Estocolmo (Suécia), 2019.

- Talk - Esclarecendo a influência do efeito de forte interação metal-suporte (SMSI) na população atômica de superfície de nanopartículas bimetálicas - *V Mostra do CNANO* - Porto Alegre (Brasil), 2019

- Talk (presented by F. Bernardi) - Probing the Nature of the Strong Metal-Support Interaction (SMSI) Effect by NAP-XPS measurements for Enhanced Catalysis - *NAP-XPS Workshop of the 29th Reunião Anual de Usuários (RAU)* - LNLS, Campinas (Brasil), 2019

- Talk (presented by F. Bernardi) - Probing the electronic nature of the SMSI effect in Pd/TiO_2 nanoparticles - *7th Annual Ambient Pressure X-ray Photoemission Spectroscopy Workshop 2020* - Pohang Accelerator Laboratory, Gyeongsangbuk-do (Coréia do Sul), 2020

- Talk - Investigando a natureza eletrônica do efeito SMSI em nanopartículas de Pd/TiO_2 - *VI Mostra do CNANO* - Porto Alegre (Brasil), 2021

4 Published Results

Applied Surface Science 574 (2022) 151647

Contents lists available at ScienceDirect

Applied Surface Science

journal homepage: www.elsevier.com/locate/apsusc

Full Length Article

New insights on the electronic factor of the SMSI effect in Pd/TiO_2 nanoparticles

Wallace T. Figueiredo [a], Ravi Prakash [b], Clóvis G. Vieira [c], Dirléia S. Lima [d], Vágner E. Carvalho [c], Edmar A. Soares [c], Silvio Buchner [a], Hannes Raschke [b], Oscar W. Perez-Lopez [d], Daniel L. Baptista [a], Roland Hergenröder [b], Maximiliano Segala [e], Fabiano Bernardi [a,*]

[a] Programa de Pós-Graduação em Física, Instituto de Física, Universidade Federal do Rio Grande do Sul (UFRGS), Porto Alegre, RS, Brazil
[b] AG Bioresponsive Materials, Leibniz-Institute für Analytische Wissenschaften, ISAS - e.V., Dortmund, Germany
[c] Departamento de Física, Instituto de Ciências Exatas, Universidade Federal de Minas Gerais (UFMG), Belo Horizonte, MG, Brazil
[d] Departamento de Engenharia Química, Escola de Engenharia, Universidade Federal do Rio Grande do Sul (UFRGS), Porto Alegre, RS, Brazil
[e] Departamento de Físico-Química, Instituto de Química, Universidade Federal do Rio Grande do Sul (UFRGS), Porto Alegre, RS, Brazil

ARTICLE INFO

Keywords:
SMSI effect
Electronic factor
NAP-XPS
UPS
DFT

ABSTRACT

Whereas observed and explored for over 40 years, there are still open questions regarding the nature of the Strong Metal-Support Interaction (SMSI) effect. The lack of a precise determination of the atomic mechanisms of electronic and geometrical factors of the SMSI effect hinders the application of metal-support systems towards several catalytic reactions. The present study sheds light on the electronic factor of the SMSI effect in Pd/TiO_2 nanoparticles by using Near Ambient Pressure Photoelectron Spectroscopy (NAP-XPS), Ultraviolet Photoelectron Spectroscopy (UPS), and Density Functional Theory (DFT) calculations. The electronic and geometrical factor of the SMSI effect were observed during reduction treatment at 300 °C and 500 °C, respectively. The results enable mapping the electronic factor during reduction treatment at 300 °C, where a charge transfer from Pd nanoparticles to TiO_2 support through Pd-O-Ti entities existing at the Pd-TiO_2 interface is observed. Furthermore, the charge transfer is mediated by O *p* states present at the Pd-TiO_2 interface.

1. Introduction

Physical and chemical surface inhomogeneities such as low coordination numbers [1], presence of corner atoms [2], shifts on electron *d* band [3], and atomic vacancies [4] describe some of the surface features that establish the flavors of the catalytic active sites of heterogeneous catalysts. In order to ensure the availability of these sites, the surface of nanostructured catalysts must be cleaned before the chemical reaction. Usually, the cleaning procedures adopted involve the exposure of the catalyst to high temperature reduction treatments. However, while eliminating adsorbed molecules (such as atmospheric remnants) from the catalysts' surface, such thermal treatments may induce atomic rearrangements or charge transfer between the catalyst components [5].

At 1978, Tauster and co-workers identified the occurrence of particular metal-support interactions while studying H_2 and CO sorption on M/TiO_2 (M = Ru, Rh, Pd, Os, Ir, Pt) systems [6]. Comparing the treatments at 200 °C and 500 °C, the authors observed that higher temperature reduction treatment induced a strong suppression on the H_2 and CO uptakes for all the samples. Further, the authors verified that this phenomenon was reversible after high temperature oxidation treatments. This atomic phenomenon was named Strong Metal-Support Interaction (SMSI) effect. Later, Tauster and Fung have further explored the occurrence of the SMSI effect on Ir nanoparticles supported on several distinct oxides [7]. Sustaining the approach of investigating the H_2 sorption on the supported systems, the authors traced the occurrence of the SMSI effect to the reducibility of the support, since refractory oxides did not manifest the interaction.

Nowadays, it is well established that the SMSI effect appears mainly due, but not limited, to geometrical or electronic factors. The geometrical factor occurs due to the oxide migration from support towards the surface of metallic nanoparticles, then encapsulating the nanoparticles and clearly influencing the catalytic activity [8]. The electronic factor may occur due a charge transfer from the support to the nanoparticles [9] or from the nanoparticles to the support [10], depending on the

* Corresponding author.
E-mail address: bernardi@if.ufrgs.br (F. Bernardi).

https://doi.org/10.1016/j.apsusc.2021.151647
Received 6 May 2021; Received in revised form 14 October 2021; Accepted 16 October 2021
Available online 21 October 2021

system used. It means the electronic density of catalysts may be controlled through the electronic factor of the SMSI effect. Furthermore, it is well accepted that the electronic factor of the SMSI effect occurs at lower temperatures than the geometrical factor [11]. Tauster et al [6] suggest the electronic factor of the SMSI effect occurs through the formation of intermetallic compounds by interaction of *d* electrons in noble metals such as Pt with vacant *d* orbitals of Ti^{4+} species at the surface. Horsley explored such intermetallic interaction through Xα self-consistent field molecular orbital calculations in the Pt-TiO_2 system. A model consisting of a single Pt atom placed near a $(TiO_6)^{8-}$ cluster was used. The calculations suggest that the O vacancies, which are created during H_2 reduction treatment, allow the approximation of Pt and Ti atoms facilitating the formation of an ionic Pt-Ti interaction with charge transferred from Ti 3d levels to the Pt 5d level [12]. Furthermore, Horsley calculations indicate that the lack of such vacancies would result on a repulsive interaction between the Pt and neighboring O atoms, so the SMSI effect would not occur. The interaction between metal nanoparticles and support may be even more complex and can be used to control the catalytic activity. For example, it was observed the creation of O vacancies in TiO_2 surface catalyzed by Pt metallic nanoparticles and this gives a charge transfer from TiO_2 support to adsorbates at O vacancies, which activates the catalyst [13].

It is well known that the interface reaction for noble metals supported on TiO_2 occurs through the encapsulation of the metallic nanoparticles [14]. Particularly, the geometrical factor of the SMSI effect for Pd/TiO_2 nanoparticles was extensively investigated in the literature through the most different approaches [15–18]. Recently, the combination of experimental and computational techniques has proved to be a very solid strategy towards the elucidation of SMSI effect mechanisms [5,18–20]. For example, Zhang et al. combined Density Functional Theory (DFT) calculations with the results obtained by in situ ambient pressure Scanning Transmission Electron Microscopy (STEM) measurements to gain insights towards the formation dynamics of the TiO_x encapsulation layers over Pd nanoparticles [18]. Increasing gradually the temperature of the reduction treatment (under H_2 atmosphere), the authors observed the progressive crystallization of the TiO_x encapsulation layers, grown amorphous at the lower temperatures. Analogously, after a gradual increase of the temperature during latter oxidation treatments (under O_2 atmosphere), the authors observed a progressive amorphization of the reduced encapsulation layers. Pd/TiO_2 nanoparticles represent the classical case of SMSI effect studied and, whether the mechanisms of nanoparticles encapsulation have been unveiled for this system, the electronic factor of the SMSI effect, which should hold for lower temperatures, was still not investigated in details. Particularly, there is no consensus about the atomic entities involved on the electronic factor of the SMSI effect in Pd/TiO_2 nanoparticles. The present work aims to shed light on the atomic events behind the electronic factor of the SMSI effect in Pd/TiO_2 nanoparticles using a combination of theoretical and in situ experimental approaches, which allows paving the way for rationally control the electronic density of catalysts.

2. Material and methods

2.1. Experimental measurements

Commercial Pd (Nano Research Elements Inc.) and TiO_2 (Sigma-Aldrich) nanoparticles were used to produce 20 wt% Pd/TiO_2 nanoparticles by sonication for 30 min. The size distribution histograms of the Pd and TiO_2 nanoparticles were obtained through the analysis of the Transmission Electron Microscopy (TEM) images, which were acquired at CMM-UFRGS using the CCD camera of the JEOL JEM 1200 Exll electron microscope, operated at 80 kV. The observation of Pd nanoparticles supported on TiO_2 was carried out through Scanning Transmission Microscopy (STEM) by using a high-angle annular dark field detector (HAADF) and Energy-Dispersive X-ray Spectroscopy (EDS). The analyses were performed using an XFEG Cs-corrected FEI Titan 80/300 microscope operated at 300 kV. The nanoparticles were dispersed in deionized water, stirred in ultrasound batch for 30 min, and a drop of the solution was deposited on a C-coated Cu grid and dried.

The crystal structure of the Pd and TiO_2 nanoparticles was probed by X-ray Diffraction (XRD) measurements at CNANO-UFRGS. The nanoparticles powder was sieved on a 48 μm mesh for the measurements. The XRD patterns were collected on a Rigaku Ultima IV diffractometer. A Cu Kα radiation source (λ = 1.5405 Å) operating at 40 kV and 17 mA was used and the diffractograms were collected in the Bragg-Brentano geometry with step size of 0.05° and acquisition time of 0.5°/s, probing a 2θ interval from 20° to 90° (Pd nanoparticles) and 20° to 80° (TiO_2 support).

As described earlier, the SMSI effect is characterized by a set of features developing after high temperature reduction treatment, which vanishes after a subsequent high temperature oxidation treatment. Therefore, aiming to study the development of metal-support interactions on the Pd/TiO_2 system, reduction and oxidation treatments were performed with two temperatures (300 °C and 500 °C). The Temperature Programmed Reduction (TPR) measurements were performed using a SAMP3 multipurpose system equipped with a thermal conductivity detector (TCD). 50 mg of the Pd/TiO_2 nanoparticles powder was inserted in a U-shapped quartz tube, exposed to 30 mL/min of 5% H_2 + 95 % N_2 atmosphere, and heated to 300 °C or 500 °C with a 10 °C/min rate. At this temperature, the nanoparticles were exposed to the reducing atmosphere for 1 h. At the end, the sample was cooled to room temperature in 30 mL/min N_2 atmosphere.

Afterward, Differential Thermal Analysis (DTA) measurements were carried out on a Shimadzu DTA-50 thermal analyzer monitoring the heat flow between a Pt crucible containing about 20 mg of the samples powder and an empty crucible (reference). These measurements were conducted while exposing the previously reduced Pd/TiO_2 nanoparticles at 300 °C or 500 °C to 10 mL/min 20% O_2 + 80 % N_2 atmosphere and heating them from room temperature to 300 °C or 500 °C, respectively, at a 10 °C/min rate. The samples remained at the selected temperatures for 1 h. At the end, the system was cooled to room temperature under the same oxidant atmosphere.

Ex situ X-ray Photoelectron Spectroscopy (XPS) measurements were carried out aiming to probe the reduction temperature range for observing the electronic factor of the SMSI effect instead of the geometrical one. A thin layer of the as prepared, reduced and oxidized nanoparticles powder was spread over a C tape placed in a Nb sample holder and inserted into the UHV chamber (base pressure around $1x10^{-9}$ mbar). The nanoparticles were exposed to a thermal treatment at 120 °C in UHV for 10 h to remove gas molecules adsorbed at the samples surface before the XPS measurements, which were conducted at room temperature. An Al Kα X-ray source (hν = 1486.7 eV) operating at 13 kV and 9.0 mA (117 W) illuminated the sample and a SPECS PHOIBOS HSA3500 CCD 100 R6-HiRes hemispherical electron analyzer collected the ejected photoelectrons. The measurements were conducted in the Survey, C 1s, O 1s, Ti 2p, and Pd 3d XPS regions. The angle between the X-ray source and the electron analyzer corresponds to 54.7°. The survey spectra were collected with 50 eV pass energy, 1.0 eV energy step, and 0.1 s of dwell time, while high resolution scans used 30 eV pass energy, 0.1 eV energy step, and 0.2 s of dwell time. Charging effects were corrected considering the adventitious carbon at C 1s XPS region at 284.5 eV. In the same experimental setup, Ultraviolet Photoelectron Spectroscopy (UPS) measurements were conducted using He II (hν = 40.8 eV) radiation. The photoelectrons were collected with 2 eV pass energy, 0.1 eV energy step, and 0.1 s of dwell time. Despite discarding charging effects during the measurements, the insulating character of the oxide support imposed limitations on the calibration of the UPS spectra. Thereby, the samples spectra were calibrated by considering the Fermi energies at the beginning of the first peak. The intensity of the spectra was normalized for comparison purposes.

Near Ambient Pressure XPS (NAP-XPS) measurements allowed the evaluation of the chemical components at the surface of Pd/TiO_2

nanoparticles during reduction and oxidation treatments. The as-prepared Pd/TiO_2 nanoparticles powder was suspended in millipore distilled water with the aid of an ultrasonic bath, and then added dropwise onto a Si substrate kept at ~ 80 °C during this process. The sample holder containing the samples were held in place by sandwiching them between two Cu plates. After this, the sample was exposed sequentially (without cooling the sample) to (i) 0.1 mbar H_2 at room temperature, (ii) 0.1 mbar H_2 at 300 °C, (iii) 0.1 mbar O_2 at 300 °C, (iv) 0.5 mbar O_2 at 300 °C, and (v) 1.0 mbar O_2 at 300 °C with a heating rate of 10 °C/min. At the end, the O_2 atmosphere was removed and the sample was cooled to room temperature under UHV. The NAP-XPS measurements were conducted during the steps (i)-(v) described. The spectrometer is equipped with a modified SPECS Phoibos 150 electron energy analyzer mounted behind a wide angular acceptance "prelens" section. The nozzle aperture to the analyzer system in front of the prelens has a diameter of 0.6 mm, and the distance between nozzle and sample surface is also around 0.6 mm. Monochromated Al Kα X-rays ($h\nu$ = 1486.7 eV) focused onto a 0.6 mm diameter spot were provided by a SPECS μ-Focus 600 photon source operating at 14 kV and 9.0 mA (126 W) [21]. The angle between the incoming X-rays and the entrance of the analyzer system was 55°. An infrared laser heater (IRLH 150 from SPECS), attached at 180° to the entrance of the analyzer system, was used to heat the samples in situ. The NAP-XPS measurements were conducted in the Survey, C 1s, O 1s, Ti 2p and Pd 3d electronic regions. The spectra were collected with 80 eV pass energy, 0.1 eV energy step, and 0.5 s of dwell time. Charging effects were corrected considering the adventitious carbon at C 1s XPS region at 284.5 eV (see Figure S1 of Supplementary material).

2.2. Theoretical calculations

Density Functional Theory (DFT) calculations were conducted for the TiO_2 bulk, TiO_2 (001) surface and Pd (001) layers over TiO_2 (001) surface. It was considered the anatase and fcc crystal structures for TiO_2 and Pd, respectively. It is known that the TiO_2 (101) and TiO_2 (100) surfaces are the most stable ones for the anatase crystal structure [22]. However, it was already reported that both H_2 atmosphere [23] and high temperature [24] treatments promote the appearance of more TiO_2 (001) facets, then making the TiO_2 (001), TiO_2 (101), and TiO_2 (100) surface probables. Furthermore, it is well known that the TiO_2 (001) surface is strongly repulsive for electrons, which are directed towards the TiO_2 (101) surface [25–26]. Since the observed effect was of electron transfer from Pd to TiO_2 surface (see Section 3), the TiO_2 (001) surface was chosen to theoretically investigate such charge transfer. Whether it is theoretically observed a charge transfer from Pd to TiO_2 (001) surface, it should occur also for other TiO_2 surfaces. The Pd (001)/TiO_2 (001) atomic cell was constructed using 2 and 5 atomic layers of Pd and TiO_2, respectively, using the Quantum Wise software. There, the initial cells of Pd (001) and TiO_2 (001) were superposed in the (001) direction taking into account the lattice mismatch between Pd and TiO_2. The atomic configuration containing the smaller surface tension was chosen. After this, a structural relaxation process was performed with the pseudopotentials used in the calculations. Figure S2 of Supplementary material shows the atomic configuration used. Within the plane waves self-consistency field (PWSCF) framework of the Quantum ESPRESSO 6.1 suit of codes [27], the DFT calculations were performed using ultrasoft pseudopotentials from the Standard Solid-State Pseudopotentials (SSSP) [28] library to describe the Pd (5s 5p 4d), Ti (4s 3d), and O (2s 2p 3d) electronic states applying Perdew-Burke-Ernzerhof (PBE) exchange–correlation functionals. The initial crystal structures were relaxed to a force per atom of 10^{-6} eV/Å after a sequence of energy minimization and geometry optimization calculations. The kinetic energy cutoff for the wave functions was set to 40 Ry and the charge density cutoff to 440 Ry. An 8x8x8 k-point mesh was used for the integration on the Brillouin zone of the materials bulk, yielding the representation of the electronic band gap. In order to enhance the convergence tendency of the calculations, a Gaussian spread (σ = 0.03) was set to the Brillouin zone integration. The electronic ground states were determined after an electronic energy convergence of 10^{-8} eV. Calculations performed for the (001) surface models used a slab of 2 × 2 × 3 (x × y × z) primitive cells of the oxide primitive cell, under a 20 Å vacuum. These surface calculations used also the same cutoff values obtained for the bulk calculations, but the integrations on the Brillouin zone were realized at the gamma point.

2.3. Data analysis

The size distribution histograms from TEM images were obtained analyzing the diameter of around 1000 nanoparticles with the ImageJ 1.46r software. Only nanoparticles presenting well distinguishable borders were taken into account. In order to estimate the diameter of irregular shaped nanoparticles, the maximum and minimum Feret diameters were measured and then averaged individually. The distribution of Pd nanoparticles supported on TiO_2 was observed using Z-contrast in HAADF-STEM images with the EDS verification.

Powder diffractograms were indexed using the PCPDFWIN software, version 2.1, using the JCPDS-ICDD database. The diffraction patterns were analysed with the Fullprof Suite software version of july-2017 using the Rietveld refinement method [29]. The Thompson-Cox-Hastings pseudo-Voigt Axial divergence asymmetry profile function [30] was used. The crystal structures of metallic Pd (JCPDS 77885), PdO (JCPDS 24692), and TiO_2 (JCPDS 92363) and the atomic positions of Pd, Ti and O atoms at the base vectors were used as input in the Fullprof software. The refinements were performed using the following constrains: (i) the V and W parameters of the Gaussian contribution of the profile function were determined by refining a reference sample and fixed to 0 for the analysis of the diffraction patterns; (ii) the isotropic temperature parameter (B-factor) and the occupancy number values of each atomic specie of each phase were fixed to the values obtained in the crystallographic information file (CIF) of metallic Pd, PdO, and TiO_2; (iii) the overall B-factor was fixed to 0. The Rietveld refinement quality is expressed on the R_{wp}/R_{exp} ratio, namely 1.50 and 1.58 for the Pd and TiO_2, respectively.

The NAP-XPS measurements were analyzed using XPSPeak 4.1 software and a Shirley-type background [31]. A symmetric Gaussian-Lorentzian function with 30% Lorentzian contribution was used. The relative binding energy and FWHM values of a given component in the NAP-XPS analysis were constrained to the same value.

3. Results and discussion

Fig. 1 shows a typical HAADF-STEM image from the Pd/TiO_2 nanoparticles. It is possible to identify the presence of well dispersed Pd nanoparticles presenting regular and circular shapes. The mean diameter was obtained from TEM images of the isolated Pd and TiO_2 nanoparticles (see Figure S3 of Supplementary material) and it corresponds to (5 ± 4) nm and (171 ± 59) nm, respectively. Fig. 1(b) shows the XRD pattern of the Pd/TiO_2 nanoparticles. The analysis of the diffraction pattern reveals that the Pd nanoparticles present the fcc crystal structure characteristic of Pd(0) (JCPDS 77885). At the same time, it is observed the presence of the anatase crystal structure (JCPDS 92363) of TiO_2. One also can notice that the Bragg reflections associated with the Pd(0) crystal structure are broader than those associated with the TiO_2 one. Such feature indicates that the Pd nanoparticles present smaller crystallites than TiO_2, as expected by the nanoparticles size observed from the HAADF-STEM and TEM measurements. Crystalline parameters obtained from Rietveld refinement analysis are displayed in Table S1 of Supplementary material. Figure S3 of Supplementary material shows the XRD pattern of the isolated Pd and TiO_2 nanoparticles, where the same features of Fig. 1(b) are observed. The only difference is the presence of the PdO phase in a small amount (3% in accordance to the Rietveld refinement), which is not observed in the Pd/TiO_2 nanoparticles due to

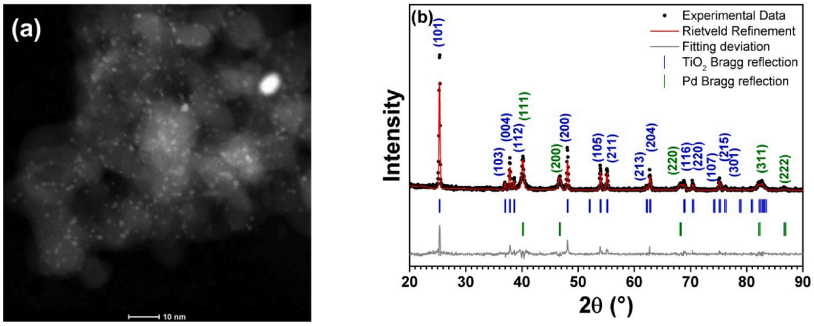

Fig. 1. (a) Typical HAADF-STEM image and (b) XRD pattern with the corresponding Rietveld refinement shown in solid red lines of the as prepared Pd/TiO_2 nanoparticles.

the presence of only 20 wt% of Pd in Pd/TiO_2 nanoparticles.

Figure S4 of Supplementary material shows the TPR measurements, where one can notice a decrease on the H_2 thermal conductivity signal at around 100 °C, which is associated to the Pd nanoparticles and comes from the decomposition of palladium hydride [32]. Furthermore, there is no signal associated with H_2 consumption, showing that the Pd nanoparticles already present an essentially reduced chemical state. Note that there is no significant changes associated with the oxide support during reduction treatment. Moreover, there is no evidence of exothermic or endothermic transformations during oxidation treatment in the sample from DTA analysis, as shown in Figure S5 of Supplementary material, then ensuring the absence of phase change during the treatment employed. Figure S6 of Supplementary material compares HAADF-STEM images of the Pd/TiO_2 nanoparticles before and after heating treatment at 500 °C in H_2 atmosphere with the EDS analysis confirming the presence of Pd after thermal treatment. Figure S7 of Supplementary material shows a comparison between the XRD patterns after reduction and oxidation treatments at 300 °C and the corresponding Rietveld refinement, whose results are presented in Table S1 of Supplementary material. Both HAADF-STEM and XRD measurements show no evidence of sintering effects in the Pd nanoparticles.

Ex situ XPS measurements allowed the identification of the thermal conditions needed to promote the geometrical factor of the SMSI effect on Pd/TiO_2 nanoparticles. Figure S8 of Supplementary material shows the ex situ XPS spectra of the Pd 3d and Ti 2p electronic regions. In this case, the photoelectrons from Pd 3d and Ti 2p have an inelastic mean free path of $\lambda \approx 16$ Å and $\lambda \approx 22$ Å, respectively [33]. It shows that both measurements are probing almost the same depth in the Pd/TiO_2 nanoparticles. In this way, it is possible to estimate the Pd 3d/Ti 2p intensity ratio in order to probe the existence of the geometrical factor of the SMSI effect. It is expected that the presence of a capping layer from the support surrounding the Pd nanoparticles would decrease the Pd 3d/Ti 2p intensity ratio in comparison to the as prepared case, as typically observed in the literature [5].

Table 1 shows the Pd 3d/Ti 2p intensity ratio as a function of the thermal treatment, which was obtained by calculating the Pd 3d and Ti 2p areas of the ex situ XPS measurements. It is possible to observe that there is a strong decrease on the Pd 3d/Ti 2p intensity ratio after reduction treatment at 500 °C in comparison to the as prepared case. It evidences the increase of the Ti 2p XPS intensity compared to the Pd 3d one, which can be interpreted as the occurrence of the encapsulation of the Pd nanoparticles by TiO_x layers. This is in accordance to what is expected [14] and that is observed in the literature for Pd/TiO_2 nanoparticles [15–18]. The subsequent oxidation treatment at 500 °C partially recovers the Pd 3d/Ti 2p intensity ratio, meaning a partial removal of the capping layer after oxidation treatment. Furthermore, a small decrease of the Pd 3d/Ti 2p intensity ratio is observed after reduction treatment at 300 °C in comparison to the as prepared case, despite inside the uncertainty. In the literature, no capping layer is observed after reduction treatment at 250 °C for Pd/TiO_2 nanoparticles [18]. Then, this result shows that probably 300 °C represents the onset for the occurrence of the geometric factor of the SMSI effect in Pd/TiO_2 nanoparticles. It is important to stress out that the geometrical factor of the SMSI effect depends on several characteristics of the support and nanoparticles and this temperature may represents a rough estimative for the onset of the geometrical factor of the SMSI effect in Pd/TiO_2 nanoparticles.

Table 1
Pd 3d/Ti 2p XPS intensity ratio as a function of the thermal treatments employed. The uncertainty of the Pd 3d/Ti 2p intensity ratio is around 20% of its value.

Condition	Pd 3d/Ti 2p XPS intensity ratio
As prepared	1.2
Reduction, 300 °C	0.8
Oxidation, 300 °C	0.9
Reduction, 500 °C	0.4
Oxidation, 500 °C	0.6

The valence bands of Pd/TiO_2 nanoparticles after reduction treatment were probed by UPS, as shown in Fig. 2. The two main electronic features are associated to the Pd and TiO_2 valence bands. Comparing the shape of the UPS spectra presented at Fig. 2, one can notice that the contribution of the TiO_2 component is very sensitive to the thermal treatment applied. After reduction treatment at 300 °C, there is a slight decrease of the TiO_2 component relative to the Pd one. It can be explained considering the presence of Ti(III) states, as observed in the ex-situ XPS measurements (Figure S8), which shift towards smaller binding energies in modulus and then gives a decrease of the UPS intensity at TiO_2 component. Nonetheless, it is observed an increase of the TiO_2 component in comparison to the Pd one after reduction treatment at 500 °C, despite the presence of Ti(III) states in the ex-situ XPS measurements (Figure S8). This behavior can be associated to the SMSI effect, since UPS measurements are very sensitive to the outermost layer of the sample and the increase of the TiO_2 contribution comes from the capping layer surrounding the Pd nanoparticles after reduction treatment at 500 °C. The behavior evidences that for low temperatures the electronic features dominate the SMSI occurrence, as described in the literature.

The ex situ XPS measurements showed clearly the occurrence of the geometrical factor of the SMSI effect after reducing treatment at 500 °C. The reduction treatment at 300 °C corresponds to the threshold condition for the geometrical factor of the SMSI effect but no clear evidence of

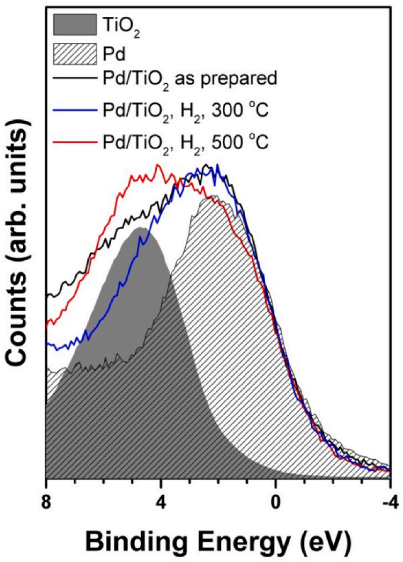

Fig. 2. UPS spectra of the Pd/TiO_2 nanoparticles before and after reduction treatment at 300 °C and 500 °C.

the electronic factor of the SMSI effect was observed in the ex situ XPS measurements, besides one would expect its occurrence before the geometrical factor of the SMSI effect. Considering this, NAP-XPS measurements were conducted to probe in situ the chemical state of the Pd/TiO_2 nanoparticles surface. Fig. 3 shows the (a) Pd 3d and (b) Ti $2p_{3/2}$ NAP-XPS spectra as a function of the reduction and oxidation treatments employed. The Pd 3d NAP-XPS spectra show the presence of two chemical components for the as prepared Pd/TiO_2 nanoparticles, which are attributed to Pd(0) and PdO, respectively [34]. This result is in accordance to the XRD findings. Table 2 shows the contribution of chemical components to Pd 3d XPS spectra as a function of the thermal treatment. The as prepared nanoparticles present 51% PdO, which is greater than 3% PdO observed in the XRD analysis due to the surface sensitivity of the NAP-XPS technique. The photoelectrons coming from Pd 3d NAP-XPS spectra present an inelastic mean free path $\lambda \approx 16$ Å [33] and the as prepared nanoparticles present surfactant at the surface, then enhancing the surface sensitivity. The reduction treatment induces a decrease of the PdO component, as expected, which increases again with the oxidation treatment. Furthermore, the oxidation treatment with 0.1 mbar O_2 does not fully oxidizes the Pd nanoparticles but 0.5 mbar does almost oxidize (around 97% PdO contribution). The Ti $2p_{3/2}$ NAP-XPS spectra show a single component associated to TiO_{2-x} [35] and there is no further component during the full experiment. As expected, the Pd 3d/Ti 2p intensity ratio remains constant (around 0.14) for all the thermal treatments studied, then showing no evidence of the geometrical factor of the SMSI effect.

The NAP-XPS spectra evidenced the occurrence of the electronic factor of the SMSI effect. It is known from the literature the existence of the hydrogen spillover effect for Pd/TiO_2 nanoparticles exposed to a H_2 atmosphere at room temperature [36]. Then it is reasonable to consider the occurrence of the spillover effect during the H_2 exposition at room temperature, which creates O vacancies at the TiO_{2-x} surface. During the thermal treatment employed, there is a clear shift of the Pd 3d NAP-XPS

Table 2
Chemical component fraction of Pd/TiO_2 nanoparticles obtained from Pd 3d NAP-XPS spectra.

Condition	Pd(0) (%)	PdO (%)
UHV	49.0	51.0
0.1 mbar H_2, RT	80.8	19.2
0.1 mbar H_2, 300 °C	78.2	21.8
0.1 mbar O_2, 300 °C	32.1	67.9
0.5 mbar O_2, 300 °C	3.2	96.8
1.0 mbar O_2, 300 °C	0.0	100

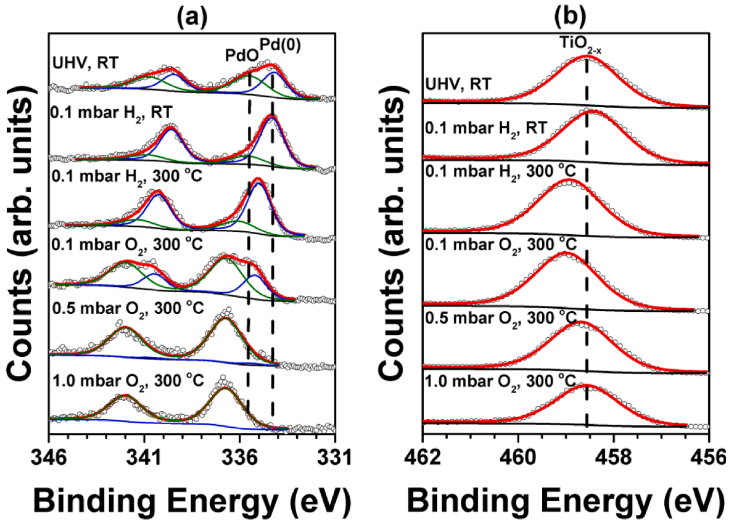

Fig. 3. (a) Pd 3d and (b) Ti $2p_{3/2}$ NAP-XPS spectra of Pd/TiO_2 nanoparticles. The empty circles show the measured data and the red, blue and green solid lines represent the best fit, Pd(0) and PdO components, respectively.

spectra towards higher binding energy values in module. The shift increases with the sequence of steps employed during the full experiment (see dashed line in Fig. 3(a)). Surprisingly, Ti $2p_{3/2}$ NAP-XPS spectrum shifts towards higher binding energies values during reduction treatment (from 0.1 mbar H_2 at room temperature to 0.1 mbar H_2 at 300 °C), but it shifts towards smaller binding energy values during oxidation treatment (from 0.1 mbar O_2 at 300 °C to 1.0 mbar O_2 at 300 °C). Since the initial surface state of Pd and TiO_{2-x} presents PdO and O vacancies, respectively, the binding energy shift observed during reduction treatment at 300 °C can be interpreted as the O migration from PdO (PdO to Pd(0) transformation) towards the Pd-TiO_{2-x} interface creating more Pd-O-Ti interface states relative to the as prepared sample. Then there is a charge transfer from Pd to O atoms, which is responsible for the Pd 3d NAP-XPS spectrum shift observed. At the same time, it oxidizes the TiO_{2-x} surface, then explaining the Ti $2p_{3/2}$ NAP-XPS spectrum shift detected. This charge transfer from the Pd nanoparticles to the TiO_2 support is characteristic of the electronic factor of the SMSI effect. In a previous work, Pd/CeO_2 nanoparticles were exposed to a reduction treatment at 500 °C in H_2 atmosphere. A charge transfer from Pd nanoparticles to CeO_2 support was observed with a small energy shift of + 0.3 eV in the Pd 3d ex situ XPS spectra after reduction treatment [10]. In this work, the Pd 3d energy shift observed in the NAP-XPS measurements during reduction treatment at 300 °C is + 0.7 eV in comparison to the as prepared case. The NAP-XPS measurements during oxidation treatment with increasing O_2 pressures corroborate the hypothesis of charge transfer via Pd-O-Ti interface states. The increase of O_2 pressure from 0.1 mbar to 0.5 mbar and then to 1.0 mbar induced a consistent shift towards opposite directions of Pd 3d and Ti $2p_{3/2}$ electronic levels. In other words, Pd 3d NAP-XPS spectrum shifts towards higher binding energy and the Ti $2p_{3/2}$ NAP-XPS spectrum goes to smaller binding energy values during oxidation treatment (from 0.1 mbar O_2 at 300 °C to 1.0 mbar O_2 at 300 °C). Because the oxidation treatment occurs at 300 °C, the TiO_{2-x} surface is oxidized to TiO_2 through the creation of even more Pd-O-Ti interface states. Then the charge transfer from Pd nanoparticles to TiO_2 support leaves it negatively charged and the Ti $2p_{3/2}$ NAP-XPS spectrum shifts to smaller binding energies while the Pd 3d NAP-XPS spectrum shifts in the opposite direction. Increasing the O_2 pressure produces more Pd-O-Ti interface states resulting in the binding energy shift observed. The experiment was repeated with a smaller H_2 and O_2 pressures of 0.05 mbar and the same trend was obtained, as demonstrated in Figure S9 of Supplementary material. The charge transfer effect from Pd nanoparticles to TiO_{2-x} support can be further observed analyzing the Ti $2p_{3/2}$ – Pd $3d_{5/2}$ binding energy difference, which shows the Pd $3d_{5/2}$ NAP-XPS region getting closer to the Ti $2p_{3/2}$ one during the full thermal treatment employed (see Figure S10 of Supplementary Material). It is interesting to note that the oxidation treatment is responsible for removing the capping layer of Pd nanoparticles during reduction treatment at high temperatures, then killing the geometrical factor of the SMSI effect, as widely reported in the literature and observed in the ex-situ XPS measurements of the present work. However, the oxidation treatment at 300 °C does not kill the electronic factor of the SMSI effect but does contribute to enhance such effect. It is important to stress out that the interface reaction expected for Pd/TiO_2 nanoparticles is the encapsulation of Pd nanoparticles by TiO_{2-x} entities from support [14] but that occurs only for high temperatures (greater than 300 °C in accordance to this work). Alloy formation and interdiffusion are not observed for TiO_2 support but the redox reaction is reported for reactive metals supported on TiO_2 [14]. In a pioneering way the present work elucidates the interface reaction existing in the Pd/TiO_2 nanoparticles before occurrence of the encapsulation effect. Furthermore, it opens new possibilities in catalysis since the charge transfer between nanoparticles and support influences the activation energy of a catalytic reaction, i.e. modifying its reaction rate [37–39]. It shows the charge transfer from Pd to TiO_2 nanoparticles can be controlled to some extent by adjusting the O_2 pressure used in the oxidation treatment.

DFT calculations were conducted aiming to corroborate the experimental results. Fig. 4 presents a comparison between the calculated DOS of TiO_2 bulk, TiO_2 (001) surface and Pd (001)/TiO_2 (001) crystal cells. The DOS values are normalized by the number of atoms used in the cell. Intending to overcome the underestimation of the band gap obtained using PBE functionals [40], a Hubbard potential (U) was added to the calculations. The DFT + U (U = 8.5 eV) calculations included Coulomb repulsion among Ti orbitals, stretching the TiO_2 band gap to 3.0 eV, as observed in Fig. 4(a). This result is close to the experimental one (3.2 eV [41] and it is also in agreement with values from DFT calculations in the literature [42]. The PDOS calculated for Pd(001)/TiO_2(001) surface shows the filling of the band gap with Pd *d* states.

The stratification of TiO_2 DOS reveals that the valence band of the oxide is dominated by O *p* orbitals. It is interesting to notice that, by breaking the crystal symmetry on the z direction, a narrow π state (non-bonding orbital) localized about 1 eV below the Fermi energy begins to detach from the valence band and move towards the oxide conduction band. Furthermore, the break of bulk crystal symmetries on the z direction, revealing the (001) surface, causes a spreading of localized states on both valence and conduction bands of TiO_2. The widening of TiO_2 valence band caused by the appearing of surface states closer to the Fermi energy reduces the oxide band gap to approximately 2 eV. The inclusion of Pd (001) layers over the TiO_2 (001) surface makes the *p*-rich valence band of TiO_2 becoming wider and presenting more localized states. The farther band, slightly detached from the others, localized at around 6 eV below the Fermi energy, is associated to the bonding σ orbital of O *p* states. At the same time, the localized bands between 2 and 6 eV below Fermi energy are associated to the non-bonding π orbitals of the O *p* states [43]. As the valence band spreads, Pd *d* states fill the band gap of TiO_2, revealing a significant superposition with non-bonding O *p* states. Furthermore, Fig. 4 shows that the bonding σ band becomes more occupied than the case without Pd layers. It is consistent with the charge transfer from the Pd nanoparticles to O atoms, as indicated by NAP-XPS measurements.

Fig. 4(d) presents the charge density calculated for TiO_2 (001) (upper) and Pd (001)/TiO_2 (001) (bottom) surfaces. It is possible to observe (see highlighted region) that the charge shared between Ti and O atoms for TiO_2 (001) surface decreases with the insertion of Pd (001). In this last case, the most relevant charge sharing occurs between O and Pd atoms. This meets the picture of charge transfer through Pd-O-Ti entities existing at the interface. Furthermore, the DOS was calculated layer-by-layer for the Pd (001)/TiO_2 (001) system (see Figure S11 of Supplementary Material) and, from that, the Bader charge was obtained layer-by-layer. The results are in clear agreement with a charge transfer from Pd nanoparticles to TiO_2 support because the Bader charge for the interface region (Pd-O-Ti entities highlighted in Fig. 4) is −1.17 (O atoms), +2.44 (Ti atoms) and + 0.06 (Pd atoms). It shows the DFT calculations support the idea that the electronic factor of the SMSI effect occurs through Pd-O-Ti interface states which promote a charge transfer from Pd to the O *p* bonding state. This result sheds light on the precise nature of the electronic factor of the SMSI effect and it shows that it does not occur through direct interaction between *d* electrons at noble metal and metal oxide, as proposed by Horsley for the Pt-TiO_2 system [12]. In the case of absence of O vacancies at the TiO_2 surface, the charge transfer still takes place, which was not observed also for the Pt-TiO_2 system [12]. Finally, mapping the electronic factor of the SMSI effect opens new possibilities on tuning the electronic density at Pd nanoparticles, then playing a key role on the projection of future smart catalysts.

4. Conclusions

The present work exposes an experimental-computational approach to elucidate the origins of the electronic factor of the SMSI effect in Pd/TiO_2 nanoparticles. The electronic and geometrical factors dominate the SMSI effect during reduction treatment at 300 °C and 500 °C,

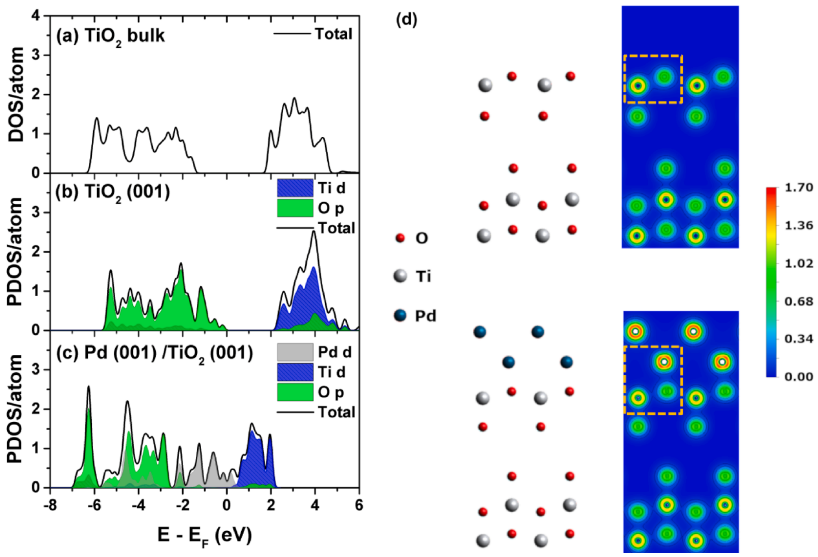

Fig. 4. (a) TiO_2 bulk density of states (DOS), (b) TiO_2 (001) surface and (c) Pd (001)/TiO_2 (001) partial density of states (PDOS) calculated by DFT. (d) Charge density of TiO_2 (001) (upper) and Pd (001)/TiO_2 (001) (bottom) surfaces.

respectively. Particularly, the electronic factor of the SMSI effect occurs through a charge transfer from the Pd nanoparticles to the O *p* bonding state of TiO_2 support and such interaction is observed during both reduction and oxidation treatments at 300 °C. The charge transfer is mediated through Pd-O-Ti entities at the Pd-TiO_2 interface.

CRediT authorship contribution statement

Wallace T. Figueiredo: Conceptualization, Formal analysis, Investigation, Methodology, Validation, Writing – original draft, Writing – review & editing. **Ravi Prakash:** Investigation, Methodology, Writing – review & editing. **Clóvis G. Vieira:** Investigation, Methodology, Writing – review & editing. **Dirléia S. Lima:** Investigation, Methodology, Writing – review & editing. **Vágner E. Carvalho:** Funding acquisition, Investigation, Methodology, Writing – review & editing. **Edmar A. Soares:** Funding acquisition, Investigation, Methodology, Writing – review & editing. **Silvio Buchner:** Funding acquisition, Investigation, Methodology, Writing – review & editing. **Hannes Raschke:** Investigation, Methodology, Writing – review & editing. **Oscar W. Perez-Lopez:** Funding acquisition, Investigation, Methodology, Writing – review & editing. **Daniel L. Baptista:** Funding acquisition, Investigation, Methodology, Writing – review & editing. **Roland Hergenröder:** Funding acquisition, Investigation, Methodology, Writing – review & editing. **Maximiliano Segala:** Conceptualization, Investigation, Methodology, Supervision, Writing – review & editing. **Fabiano Bernardi:** Conceptualization, Formal analysis, Funding acquisition, Investigation, Methodology, Project administration, Resources, Supervision, Validation, Writing – original draft, Writing – review & editing.

Declaration of Competing Interest

The authors declare that they have no known competing financial interests or personal relationships that could have appeared to influence the work reported in this paper.

Acknowledgments

The authors thank the Centro de Nanociência e Nanotecnologia (CNANO), Centro de Microscopia e Microanálise (CMM), Núcleo de Laboratórios de Microscopia do Inmetro (Nulam), Centro Nacional de Supercomputação (CESUP) and Laboratório Nacional de Computação Científica (LNCC) across SDumont Supercomputer. W. T. F., and F. B. thank the CNPq for the research grant. The authors also thank CAPES – Finance Code 001.

Appendix A. Supplementary material

Supplementary data to this article can be found online at https://doi.org/10.1016/j.apsusc.2021.151647.

References

[1] J.K. Nørskov, T. Bligaard, B. Hvolbæk, F. Abild-Pedersen, I.b. Chorkendorff, C. H. Christensen, The nature of the active site in heterogeneous metal catalysis, Chem. Soc. Rev. 37 (10) (2008) 2163, https://doi.org/10.1039/b800260f.

[2] W.D. Williams, M. Shekhar, W.-S. Lee, V. Kispersky, W.N. Delgass, F.H. Ribeiro, S. M. Kim, E.A. Stach, J.T. Miller, L.F. Allard, Metallic Corner Atoms in Gold Clusters Supported on Rutile Are the Dominant Active Site during Water–Gas Shift Catalysis, J. Am. Chem. Soc. 132 (40) (2010) 14018–14020, https://doi.org/10.1021/ja1064262.

[3] J.-H. Zhong, X. Jin, L. Meng, X. Wang, H.-S. Su, Z.-L. Yang, C.T. Williams, B. Ren, Probing the electronic and catalytic properties of a bimetallic surface with 3 nm resolution, Nat. Nanotechnol. 12 (2017) 132–136, https://doi.org/10.1038/nnano.2016.241.

[4] Y.-G. Wang, D. Mei, V.-A. Glezakou, J. Li, R. Rousseau, Dynamic formation of single-atom catalytic active sites on ceria-supported gold nanoparticles, Nat. Commun. 6 (2015) 6511, https://doi.org/10.1038/ncomms7511.

[5] W.T. Figueiredo, G.B. Della Mea, M. Segala, D.L. Baptista, C. Escudero, V. Pérez-Dieste, F. Bernardi, Understanding the Strong Metal-Support Interaction (SMSI) Effect in Cu_xNi_{1-x}/CeO_2 ($0 < x < 1$) Nanoparticles for Enhanced Catalysis, ACS Appl, Nano Mater. 2 (2019) 2559–2573, https://doi.org/10.1021/acsanm.9b00569.

[6] S.J. Tauster, S.C. Fung, R.L. Garten, Strong metal-support interactions. Group 8 noble metals supported on titanium dioxide, J. Am. Chem. Soc. 100 (1) (1978) 170–175, https://doi.org/10.1021/ja00469a029.

[7] S. TAUSTER, Strong metal-support interactions: Occurrence among the binary oxides of groups IIA-VB, J. Catal. 55 (1) (1978) 29–35, https://doi.org/10.1016/0021-9517(78)90182-3.

[8] W.T. Figueiredo, C. Escudero, V. Pérez-Dieste, C.A. Ospina, F. Bernardi, Determining the Surface Atomic Population of Cu_xNi_{1-x}/CeO_2 ($0 < x \leq 1$) Nanoparticles during the Reverse Water-Gas Shift (RWGS) Reaction, J. Phys. Chem. C. 124 (2020) 16868–16878, https://doi.org/10.1021/acs.jpcc.0c01498.

[9] L.P. Matte, A.S. Kilian, L. Luza, M.C.M. Alves, J. Morais, D.L. Baptista, J. Dupont, F. Bernardi, Influence of the CeO_2 Support on the Reduction Properties of Cu/CeO_2 and Ni/CeO_2 Nanoparticles, J. Phys. Chem. C. 119 (47) (2015) 26459–26470, https://doi.org/10.1021/acs.jpcc.5b07654.

[10] A.S. Thill, A.S. Kilian, F. Bernardi, Key Role Played by Metallic Nanoparticles on the Ceria Reduction, J. Phys. Chem. C. 121 (45) (2017) 25323–25332, https://doi.org/10.1021/acs.jpcc.7b09013.

[11] S. Bernal, J.J. Calvino, M.A. Cauqui, J.M. Gatica, C. Larese, J.A. Pérez Omil, J. M. Pintado, Some recent results on metal/support interaction effects in NM/CeO_2 (NM: noble metal) catalysts, Catal. Today. 50 (2) (1999) 175–206, https://doi.org/10.1016/S0920-5861(98)00503-3.

[12] J.A. Horsley, A Molecular Orbital Study of Strong Metal-Support Interaction between Platinum and Titanium Dioxide, J. Am. Chem. Soc. 101 (11) (1979) 2870–2874, https://doi.org/10.1021/ja00505a011.

[13] G. Kennedy, L.R. Baker, G.A. Somorjai, Selective Amplification of C=O Bond Hydrogenation on Pt/TiO_2: Catalytic Reaction and Sum-Frequency Generation Vibrational Spectroscopy Studies of Crotonaldehyde Hydrogenation, Angew. Chem. Int. Ed. Engl. 53 (13) (2014) 3405–3408, https://doi.org/10.1002/anie.201400081.

[14] Q. Fu, T. Wagner, Interaction of nanostructured metal overlayers with oxide surfaces, Surf. Sci. Rep. 62 (11) (2007) 431–498, https://doi.org/10.1016/j.surfrep.2007.07.001.

[15] Q. Fu, T. Wagner, S. Olliges, H.D. Carstanjen, Metal-oxide interfacial reactions: Encapsulation of Pd on TiO_2 (110), J. Phys. Chem. B. 109 (2005) 944–951, https://doi.org/10.1021/jp046091u.

[16] T. Suzuki, R. Souda, Encapsulation of Pd by the supporting TiO_2 (110) surface induced by strong metal-support interactions, Surf. Sci. 448 (2000) 33–39, https://doi.org/10.1016/S0039-6028(99)01201-7.

[17] R.A. Bennett, C.L. Pang, N. Perkins, R.D. Smith, P. Morrall, R.I. Kvon, M. Bowker, Surface structures in the SMSI state; Pd on (1×2) reconstructed TiO_2 (110), J. Phys. Chem. B. 106 (18) (2002) 4688–4696, https://doi.org/10.1021/jp0138328.

[18] S. Zhang, P.N. Plessow, J.J. Willis, S. Dai, M. Xu, G.W. Graham, M. Cargnello, F. Abild-Pedersen, X. Pan, Dynamical observation and detailed description of catalysts under strong metal-support interaction, Nano Lett. 16 (7) (2016) 4528–4534, https://doi.org/10.1021/acs.nanolett.6b0176910.1021/acs.nanolett.6b01769.s001.

[19] G.N. Vayssilov, Y. Lykhach, A. Migani, T. Staudt, G.P. Petrova, N. Tsud, T. Skála, A. Bruix, F. Illas, K.C. Prince, V. Matolín, K.M. Neyman, J. Libuda, V. Matolín, K. M. Neyman, J. Libuda, Support nanostructure boosts oxygen transfer to catalytically active platinum nanoparticles, Nat. Mater. 10 (2011) 310–315, https://doi.org/10.1038/nmat2976.

[20] A. Bruix, José.A. Rodriguez, P.J. Ramírez, S.D. Senanayake, J. Evans, J.B. Park, D. Stacchiola, P. Liu, J. Hrbek, F. Illas, A New Type of Strong Metal-Support Interaction and the Production of H_2 through the Transformation of Water on Pt/CeO_2 (111) and $Pt/CeO_x/TiO_2$ (110) Catalysts, J. Am. Chem. Soc. 134 (21) (2012) 8968–8974, https://doi.org/10.1021/ja302070k.

[21] A. Jurgensen, N. Esser, R. Hergenroder, Near ambient pressure XPS with a conventional X-ray source, Surf. Interf. Anal. 44 (2012) 1100–1103, https://doi.org/10.1002/sia.4826.

[22] U. Diebold, The Surface Science of Titanium Dioxide, Surf. Sci. Rep. 48 (5-8) (2003) 53–229, https://doi.org/10.1016/S0167-5729(02)00100-0.

[23] A.S. Barnard, P. Zapol, Predicting the Energetics, Phase Stability, and Morphology Evolution of Faceted and Spherical Anatase Nanocrystals, J. Phys. Chem. B 108 (48) (2004) 18435–18440, https://doi.org/10.1021/jp0472459.

[24] T.D. Malevu, B.S. Mwankemwa, S.V. Motloung, K.G. Tshabalala, R.O. Ocaya, Effect of annealing temperature on nano-crystalline TiO_2 for solar cell applications, Physica E: Low-dim. Syst. Nanost. 106 (2019) 127–132, https://doi.org/10.1016/j.physe.2018.10.028.

[25] S. Selcuk, A. Selloni, Facet-dependent trapping and dynamics of excess electrons at anatase TiO_2 surfaces and aqueous interfaces, Nat. Mater. 15 (10) (2016) 1107–1112.

[26] M. D'Arienzo, M.V. Dozzi, M. Redaelli, B. Di Credico, F. Morazzoni, R. Scotti, S. Polizzi, Crystal Surfaces and Fate of Photogenerated Defects in Shape-Controlled Anatase Nanocrystals: Drawing Useful Relations to Improve the H_2 Yield in Methanol Photosteam Reforming, J. Phys. Chem. C 119 (2015) 12385–12393, https://doi.org/10.1021/acs.jpcc.5b01814.

[27] P. Giannozzi, S. Baroni, N. Bonini, M. Calandra, R. Car, C. Cavazzoni, D. Ceresoli, G.L. Chiarotti, M. Cococcioni, I. Dabo, A. Dal Corso, S. de Gironcoli, S. Fabris, G. Fratesi, R. Gebauer, U. Gerstmann, C. Gougoussis, A. Kokalj, M. Lazzeri, L. Martin-Samos, N. Marzari, F. Mauri, R. Mazzarello, S. Paolini, A. Pasquarello, L. Paulatto, C. Sbraccia, S. Scandolo, G. Sclauzero, A.P. Seitsonen, A. Smogunov, P. Umari, R.M. Wentzcovitch, QUANTUM ESPRESSO: a modular and open-source software project for quantum simulations of materials, J. Phys. Condens. Matter. 21 (39) (2009) 395502, https://doi.org/10.1088/0953-8984/21/39/395502.

[28] G. Prandini, A. Marrazzo, I.E. Castelli, N. Mounet, N. Marzari, Precision and efficiency in solid-state pseudopotential calculations, Npj Comput. Mater. 4 (2018) 72, https://doi.org/10.1038/s41524-018-0127-2.

[29] L.B. McCusker, R.B. Von Dreele, D.E. Cox, D. Louër, P. Scardi, Rietveld refinement guidelines, J. Appl. Crystallogr. 32 (1) (1999) 36–50, https://doi.org/10.1107/S0021889898009856.

[30] P. Thompson, D.E. Cox, J.B. Hastings, Rietveld refinement of Debye-Scherrer synchrotron X-ray data from Al2O3, J. Appl. Crystallogr. 20 (2) (1987) 79–83, https://doi.org/10.1107/S0021889887087090.

[31] D.A. Shirley, High-Resolution X-Ray Photoemission Spectrum of the Valence Bands of Gold, Phys. Rev. B. 5 (12) (1972) 4709–4714, https://doi.org/10.1103/PhysRevB.5.4709.

[32] U.S. Ozkan, M.W. Kumthekar, G. Karakas, Characterization and temperature-programmed studies over Pd/TiO_2 catalysts for NO reduction with methane, Catal. Today. 40 (1) (1998) 3–14, https://doi.org/10.1016/S0920-5861(97)00112-0.

[33] D. Tahir, Suarga, N.H. Sari, Yulianti, Stopping powers and inelastic mean free path of 200 eV–50 keV electrons in polymer PMMA, PE, and PVC, Appl. Radiat. Isot. 95 (2015) 59–62. https://doi.org/10.1016/j.apradiso.2014.10.001.

[34] F. Bernardi, M.E. Grass, Y.P. Hong, R. Chang, N. Jabeen, C. Zhang, B.W. Eichhorn, B. Seo, S. Alayoglu, Z. Hussain, S.H. Joo, Z. Liu, Control of the surface atomic population of $Rh_{0.5}Pd_{0.5}$ bimetallic nanoparticles supported on CeO_2, Catal. Today. 260 (2016) 95–99, https://doi.org/10.1016/j.cattod.2015.06.024.

[35] J.F. Moulder, W.F. Stickle, P.E. Sobol, K.D. Bomben, Handbook of X-ray photoelectron spectroscopy: a reference book of standard spectra for identification and interpretation of XPS data, 1992.

[36] J.C. Conesa, J. Soria, Reversible Ti^{3+} Formation by H_2 Adsorption on M/TiO_2 Catalysts, J. Phys. Chem. 86 (1982) 1392–1395, https://doi.org/10.1021/j100397a035.

[37] G.-M. Schwab, H. Schultes, The mode of action of mixed catalysts on the decomposition of nitrous oxide, Zeitschrift Fuer Phys. Chemie, Abteilung B Chemie Der Elem. Aufbau Der Mater. 9 (1930) 265–288.

[38] G.-M. Schwab, Chemical effects at the solid/solid phase boundary, J. Colloid Interface Sci. 34 (3) (1970) 337–342, https://doi.org/10.1016/0021-9797(70)90192-X.

[39] G.M. Schwab, Electronics of Supported Catalysts, Adv. Catal. 27 (1979) 1–22, https://doi.org/10.1016/S0360-0564(08)60052-8.

[40] J.P. Perdew, W. Yang, K. Burke, Z. Yang, E.K.U. Gross, M. Scheffler, G.E. Scuseria, T.M. Henderson, I.Y. Zhang, A. Ruzsinszky, H. Peng, J. Sun, E. Trushin, A. Görling, Understanding band gaps of solids in generalized Kohn-Sham theory, Proc. Natl. Acad. Sci. U. S. A. 114 (11) (2017) 2801–2806, https://doi.org/10.1073/pnas.1621352114.

[41] D. Reyes-Coronado, G. Rodríguez-Gattorno, M.E. Espinosa-Pesqueira, C. Cab, R. de Coss, G. Oskam, Phase-pure TiO_2 nanoparticles: Anatase, brookite and rutile, Nanotechnology. 19 (14) (2008) 145605, https://doi.org/10.1088/0957-4484/19/14/145605.

[42] M.E. Arroyo-de Dompablo, A. Morales-García, M. Taravillo, DFTU calculations of crystal lattice, electronic structure, and phase stability under pressure of TiO2 polymorphs, J. Chem. Phy. 135 (5) (2011) 054503, https://doi.org/10.1063/1.3617244.

[43] S.-D. Mo, W.Y. Ching, Electronic and optical properties of three phases of titanium dioxide: Rutile, anatase, and brookite, Phys. Rev. B. 51 (19) (1995) 13023–13032.

New insights on the electronic factor of the SMSI effect in Pd/TiO_2 nanoparticles

Wallace T. Figueiredo[a], Ravi Prakash[b], Clóvis G. Vieira[c], Dirléia S. Lima[d], Vágner E. Carvalho[c], Edmar A. Soares[c], Silvio Buchner[a], Hannes Raschke[b], Oscar W. Perez-Lopez[d], Daniel L. Baptista[a], Roland Hergenröder[b], Maximiliano Segala[c], Fabiano Bernardi[a,*]

[a] Programa de Pós-Graduação em Física, Instituto de Física, Universidade Federal do Rio Grande do Sul (UFRGS), Porto Alegre, RS, Brazil

[b] AG Bioresponsive Materials, Leibniz-Institute für Analytische Wissenschaften, ISAS - e.V., Dortmund, Germany

[c] Departamento de Física, Instituto de Ciências Exatas, Universidade Federal de Minas Gerais (UFMG), Belo Horizonte, MG, Brazil

[d] Departamento de Engenharia Química, Escola de Engenharia, Universidade Federal do Rio Grande do Sul (UFRGS), Porto Alegre, RS, Brazil

[e] Departamento de Físico-Química, Instituto de Química, Universidade Federal do Rio Grande do Sul (UFRGS), Porto Alegre, RS, Brazil

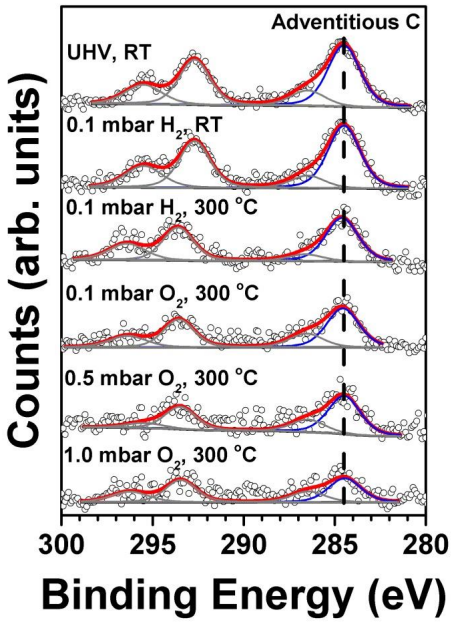

Figure S1 – C 1s NAP-XPS spectra of Pd/TiO_2 nanoparticles. The empty circles show the measured data and the red, blue and gray solid lines represent the best fit, adventitious C and other C components, respectively.

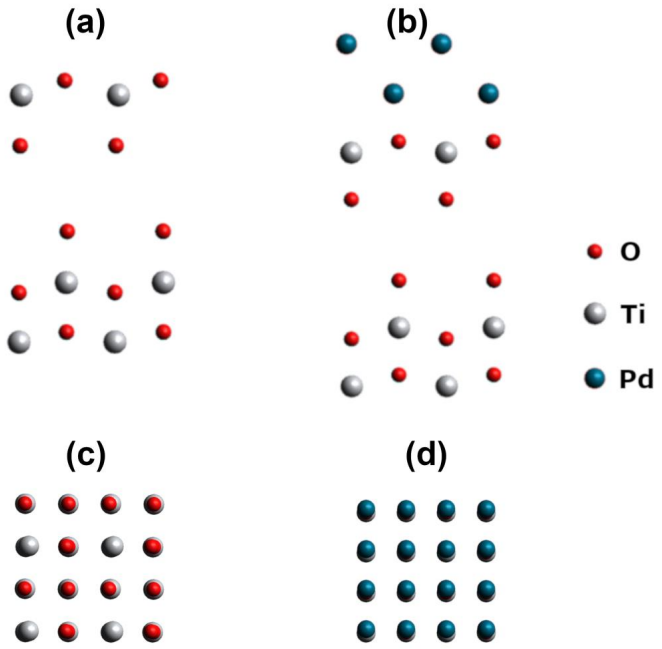

Figure S2 – Side view ((a) and (b)) and top view ((c) and (d)) of the atomic positions after relaxation for DFT calculations for TiO_2 (001) ((a) and (c)) and Pd (001)/TiO_2 (001) systems.

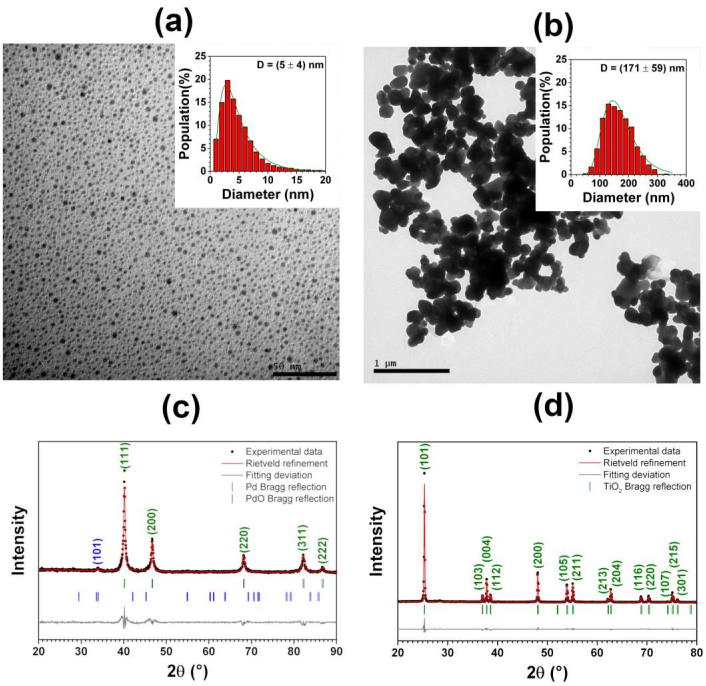

Figure S3 – Typical TEM images from the (a) Pd and (b) TiO_2 nanoparticles with the corresponding size distribution histograms and the XRD patterns of (c) Pd and (d) TiO_2 nanoparticles with the corresponding Rietveld refinement shown in solid red lines.

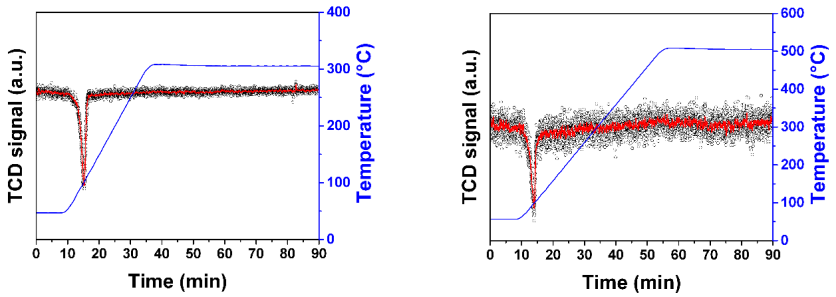

Figure S4 – TPR measurements of Pd/TiO_2 nanoparticles during reduction treatment in 30 mL/min of 5% H_2 + 95% N_2 atmosphere at (a) 300 °C and (b) 500 °C. The solid red line is used only to guide the eyes.

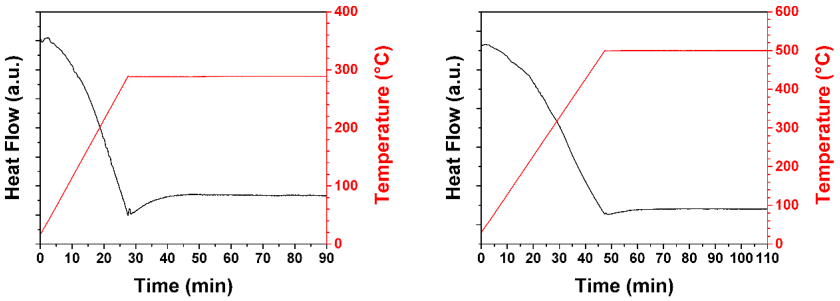

Figure S5 – DTA measurements of Pd/TiO_2 nanoparticles during oxidation treatment in 10 mL/min 20% O_2 + 80% N_2 atmosphere at (a) 300 °C and (b) 500 °C.

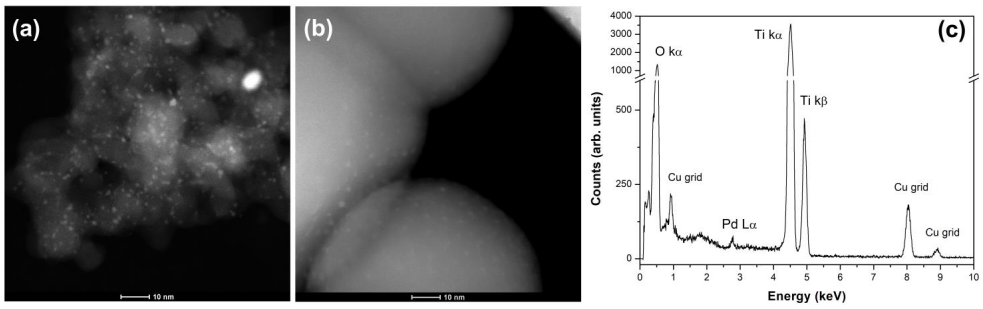

Figure S6 – HAADF-STEM imagens of Pd/TiO_2 nanoparticles for the (a) as prepared and (b) after reduction treatment at 500 °C. The global EDS spectrum (c) of an area of (b) confirms the presence of Pd.

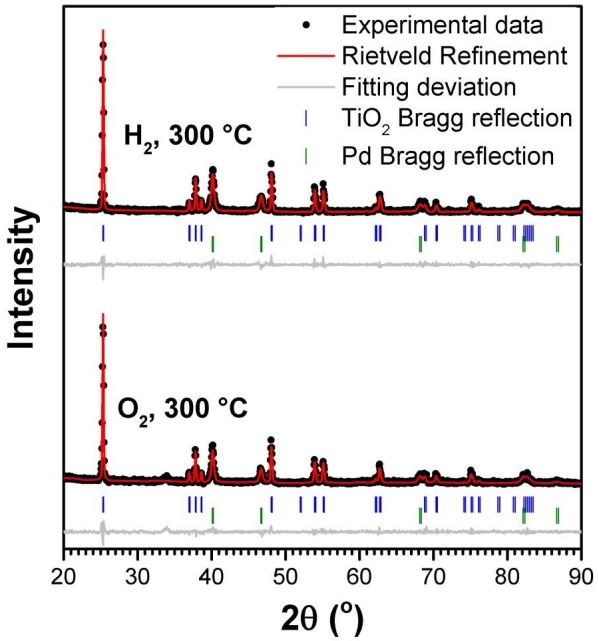

Figure S7 – XRD pattern of the Pd/TiO_2 nanoparticles after reduction and oxidation treatment at 300 °C with the corresponding Rietveld refinement shown in solid red lines.

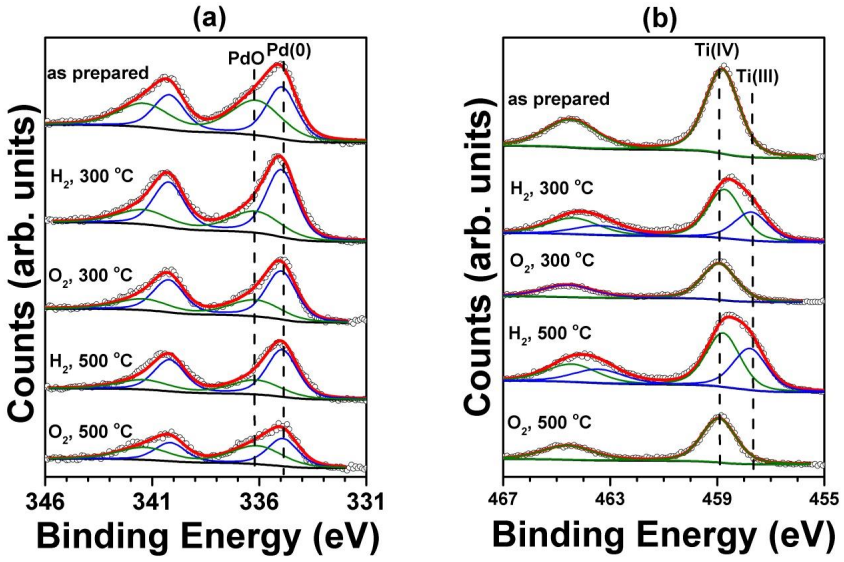

Figure S8 - Ex-situ XPS measurements at (a) Pd 3d and (b) Ti 2p regions of Pd/TiO_2 nanoparticles. The as prepared case refers to the initial condition of the Pd/TiO_2 nanoparticles for the ex-situ measurements, that is, after thermal treatment at 120 °C in UHV during 10 h. The Ti(III) component comes from the O vacancies created after reduction treatment.

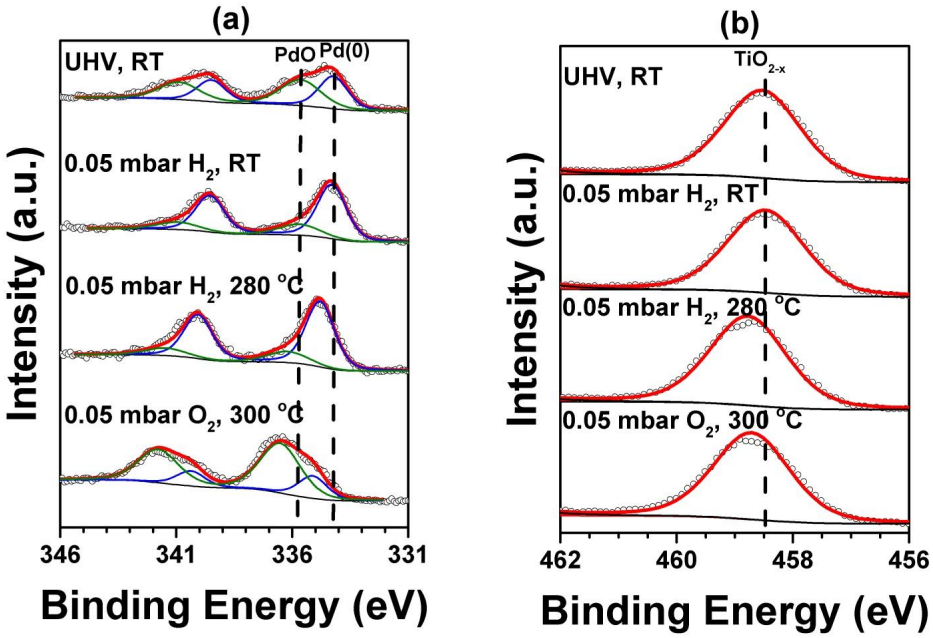

Figure S9 - (a) Pd 3d and (b) Ti $2p_{3/2}$ NAP-XPS spectra of Pd/TiO_2 nanoparticles using a smaller pressure of H_2 and O_2 of 0.05 mbar. The empty circles show the measured data and the red, blue and green solid lines represent the best fit, Pd(0) and PdO components, respectively.

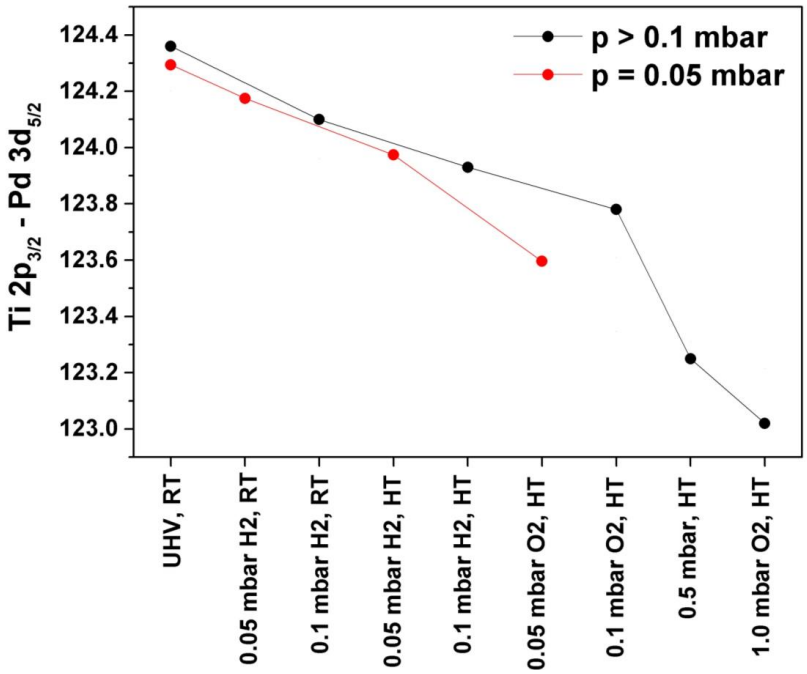

Figure S10 – Binding energy difference between Ti $2p_{3/2}$ and Pd $3d_{5/2}$ NAP-XPS position as a function of the thermal treatment employed. The Ti $2p_{3/2}$ and Pd $3d_{5/2}$ energy positions were obtained with the TiO_{2-x} and Pd(0) components, respectively. RT and HT stand for room temperature and high temperature, respectively. The black and red points correspond to measurements with $p \geq 0.1$ mbar and $p = 0.05$ mbar, respectively.

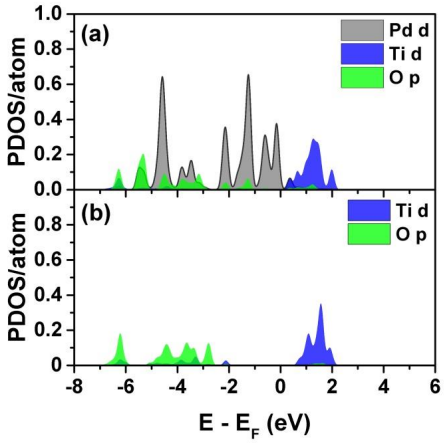

Figure S11 – Pd (001)/TiO_2 (001) partial density of states (PDOS) at the (a) interface layer between Pd (001) and TiO_2 (001) and (b) bottom layer of TiO_2 (001).

Table S1 – Crystalite size (D_c) determined by Rietveld refinement of the XRD powder diffractogram of Pd/TiO_2 nanoparticles.

Sample	**Crystalline phase**	**D_c (nm)**
Pd/TiO_2 as prepared	Pd(0)	34
Pd/TiO_2, H_2, 300 °C	Pd(0)	30
Pd/TiO_2, O_2, 300 °C	Pd(0)	31

Bibliography

[1] Bård Lindström and Lars J. Pettersson. A brief history of catalysis. *CATTECH*, 7 (4):130–138, Aug 2003. ISSN 1572-8811. doi: 10.1023/A:1025001809516.

[2] Valerius Cordus and Jacques Dubois. *Le guidon des apotiquaires: C'est à dire, la vraye forme & maniere, de composer les medicamens.* Pour Loys Cloquemin, & Estienne Michel., 1966.

[3] S. K. Kirchhoff. Die entdeckung der leichten umwandlung der stärke in zucker. *Bull Neusten Wiss Naturwiss*, 10:88–92, 1811.

[4] L. Thenard. Observations sur l'influence de l'eau dans la formation des acides oxigénés. *Ann. Chim*, 9:314–317, 1818.

[5] Edmund Davy. Vi. on some combinations of platinum. *Philosophical Transactions of the Royal Society of London*, (110):108–125, 1820.

[6] P. L. Dulong and L. Thenard. Note sur la propriété que possèdent quelques métaux de faciliter la combinaison des fluides élastiques. *Ann. Chim*, 2(23):440–444, 1823.

[7] JJ Berzelius. Quelques idées sur une nouvelle force agissant dans les combinaisons des corps organiques. *Ann. Chim*, 61:146–151, 1836.

[8] Jaime Wisniak. The history of catalysis. from the beginning to nobel prizes. *Educación Química*, 21(1):60 – 69, 2010. ISSN 0187-893X. doi: https://doi.org/10.1016/S0187-893X(18)30074-0.

[9] Ludwig Wilhelmy. *Ueber das Gesetz, nach welchem die Einwirkung der Säuren auf den Rohrzucker stattfindet.* Number 29. Engelmann, 1891.

[10] Jacobus Henricus Van't Hoff. *Etudes de dynamique chimique*, volume 1. Muller, 1884.

[11] J.A. Moulijn, P.W.N.M. van Leeuwen, and R.A. van Santen. *Catalysis: An Integrated Approach to Homogeneous, Heterogeneous and Industrial Catalysis.* ISSN. Elsevier Science, 1993. ISBN 9780080886985.

[12] Carl Bosch. Nobel lecture. URL https://www.nobelprize.org/prizes/chemistry/1931/bosch/lecture/. Nobel Prize Outreach AB 2021 (accessed: August 4, 2021).

[13] Fritz Haber. Nobel lecture. URL https://www.nobelprize.org/prizes/chemistry/1918/haber/lecture/. Nobel Prize Outreach AB 2021 (accessed: August 4, 2021).

[14] Chris Adams. Applied catalysis: A predictive socioeconomic history. *Topics in Catalysis*, 52(8):924–934, Jul 2009. ISSN 1572-9028. doi: 10.1007/s11244-009-9251-z.

[15] W Ostwald. Improvements in the manufacture of nitric acid and nitrogen oxides. *GBD190200698*, 19020109, 1902.

[16] Jan Willem Erisman, Mark A Sutton, James Galloway, Zbigniew Klimont, and Wilfried Winiwarter. How a century of ammonia synthesis changed the world. *Nature Geoscience*, 1(10):636, 2008.

[17] John N. Armor. A history of industrial catalysis. *Catalysis Today*, 163(1):3 – 9, 2011. ISSN 0920-5861. doi: https://doi.org/10.1016/j.cattod.2009.11.019. Special issue on Industrial Catalysis.

[18] Paul R. Ehrlich and John P. Holdren. Impact of population growth. *Science*, 171 (3977):1212–1217, 1971. ISSN 00368075, 10959203.

[19] Thomas Wiedmann, Manfred Lenzen, Karen Turner, and John Barrett. Examining the global environmental impact of regional consumption activities — part 2: Review of input–output models for the assessment of environmental impacts embodied in trade. *Ecological Economics*, 61(1):15 – 26, 2007. ISSN 0921-8009. doi: https://doi.org/10.1016/j.ecolecon.2006.12.003.

[20] Atsushi Beniya and Shougo Higashi. Towards dense single-atom catalysts for future automotive applications. *Nature Catalysis*, 2(7):590–602, 2019.

[21] Paul Boldrin and Nigel P Brandon. Progress and outlook for solid oxide fuel cells for transportation applications. *Nature Catalysis*, 2(7):571–577, 2019.

[22] Hirohisa Tanaka, Masashi Taniguchi, Mari Uenishi, Nobuhiko Kajita, Isao Tan, Yasuo Nishihata, Jun'ichiro Mizuki, Keiichi Narita, Mareo Kimura, and Kimiyoshi Kaneko. Self-regenerating rh-and pt-based perovskite catalysts for automotive-emissions control. *Angewandte Chemie International Edition*, 45(36):5998–6002, 2006.

[23] An-Jie Zhang, Ai-Min Zhu, Jun Guo, Yong Xu, and Chuan Shi. Conversion of greenhouse gases into syngas via combined effects of discharge activation and catalysis. *Chemical Engineering Journal*, 156(3):601–606, 2010.

[24] Mun-Sing Fan, Ahmad Zuhairi Abdullah, and Subhash Bhatia. Utilization of greenhouse gases through carbon dioxide reforming of methane over ni–co/mgo–zro2: preparation, characterization and activity studies. *Applied Catalysis B: Environmental*, 100(1-2):365–377, 2010.

[25] Paul Anastas and Nicolas Eghbali. Green chemistry: Principles and practice. *Chemical Society Reviews*, 39(1):301–312, 2010. ISSN 14604744. doi: 10.1039/b918763b.

[26] Ioana Fechete, Ye Wang, and Jacques C. Védrine. The past, present and future of heterogeneous catalysis. *Catalysis Today*, 189(1):2–27, 2012. ISSN 0920-5861. doi: https://doi.org/10.1016/j.cattod.2012.04.003. Catalytic Materials for Energy: Past, Present and Future.

[27] Francisco Zaera. Mechanisms of hydrocarbon conversion reactions on heterogeneous catalysts: analogies with organometallic chemistry. *Topics in Catalysis*, 34(1):129–141, May 2005. ISSN 1572-9028. doi: 10.1007/s11244-005-3806-4.

[28] Ulf Hanefeld and Leon Lefferts. *Catalysis: An Integrated Textbook for Students*. John Wiley & Sons, 2018.

[29] S Ted Oyama and Gabor A Somorjai. Homogeneous, heterogeneous, and enzymatic catalysis. *Journal of Chemical Education*, 65(9):765, 1988.

[30] Gabor A Somorjai and Yimin Li. *Introduction to surface chemistry and catalysis*. John Wiley & Sons, 2010.

[31] Yimin Li and Gabor A. Somorjai. Nanoscale advances in catalysis and energy applications. *Nano Letters*, 10(7):2289–2295, 2010. doi: 10.1021/nl101807g. PMID: 20524636.

[32] Eric W. Wong, Paul E. Sheehan, and Charles M. Lieber. Nanobeam mechanics: Elasticity, strength, and toughness of nanorods and nanotubes. *Science*, 277(5334): 1971–1975, 1997. ISSN 0036-8075. doi: 10.1126/science.277.5334.1971.

[33] Bin Wu, Andreas Heidelberg, and John J Boland. Mechanical properties of ultrahigh-strength gold nanowires. *Nature materials*, 4(7):525, 2005.

[34] Lien T. Ngo, Dorothée Almécija, John E. Sader, Brian Daly, Nikolay Petkov, Justin D. Holmes, Donats Erts, and John J. Boland. Ultimate-strength germanium nanowires. *Nano Letters*, 6(12):2964–2968, 2006. doi: 10.1021/nl0619397. PMID: 17163740.

[35] Baomei Wen, John E. Sader, and John J. Boland. Mechanical properties of zno nanowires. *Phys. Rev. Lett.*, 101:175502, Oct 2008. doi: 10.1103/PhysRevLett.101.175502.

[36] Richard D. Averitt, Sarah L. Westcott, and Naomi J. Halas. Linear optical properties of gold nanoshells. *J. Opt. Soc. Am. B*, 16(10):1824–1832, Oct 1999. doi: 10.1364/JOSAB.16.001824.

[37] Lin Guo, Shihe Yang, Chunlei Yang, Ping Yu, Jiannong Wang, Weikun Ge, and George K. L. Wong. Highly monodisperse polymer-capped zno nanoparticles: Preparation and optical properties. *Applied Physics Letters*, 76(20):2901–2903, 2000. doi: 10.1063/1.126511.

[38] JP Borah and KC Sarma. Optical and optoelectronic properties of zns nanostructured thin film. *Acta Physica Polonica-Series A General Physics*, 114 (4):713, 2008.

[39] TW Ebbesen, HJ Lezec, H Hiura, JW Bennett, HF Ghaemi, and T Thio. Electrical conductivity of individual carbon nanotubes. *Nature*, 382(6586):54, 1996.

[40] Jan Richter, Michael Mertig, Wolfgang Pompe, Ingolf Mönch, and Hans K. Schackert. Construction of highly conductive nanowires on a dna template. *Applied Physics Letters*, 78(4):536–538, 2001. doi: 10.1063/1.1338967.

[41] Jinhwan Lee, Phillip Lee, Hyungman Lee, Dongjin Lee, Seung Seob Lee, and Seung Hwan Ko. Very long ag nanowire synthesis and its application in a highly transparent, conductive and flexible metal electrode touch panel. *Nanoscale*, 4(20): 6408–6414, 2012.

[42] Gabor A Somorjai and Jose Carrazza. Structure sensitivity of catalytic reactions. *Industrial & engineering chemistry fundamentals*, 25(1):63–69, 1986.

[43] R.K. Herz, W.D. Gillespie, E.E. Petersen, and G.A. Somorjai. The structure sensitivity of cyclohexane dehydrogenation and hydrogenolysis catalyzed by platinum single crystals at atmospheric pressure. *Journal of Catalysis*, 67(2):371 – 386, 1981. ISSN 0021-9517. doi: https://doi.org/10.1016/0021-9517(81)90297-9.

[44] D. Wayne Goodman. Ethane hydrogenolysis over single crystals of nickel: Direct detection of structure sensitivity. *Surface Science Letters*, 123(1):L679 – L68, 1982. ISSN 0167-2584. doi: https://doi.org/10.1016/0167-2584(82)90071-8.

[45] Christine E Garrett and Kapa Prasad. The art of meeting palladium specifications in active pharmaceutical ingredients produced by pd-catalyzed reactions. *Advanced Synthesis & Catalysis*, 346(8):889–900, 2004.

[46] Janet Kielhorn, Christine Melber, Detlef Keller, and Inge Mangelsdorf. Palladium–a review of exposure and effects to human health. *International journal of hygiene and environmental health*, 205(6):417–432, 2002.

[47] WM Sharman and JE Van Lier. Use of palladium catalysis in the synthesis of novel porphyrins and phthalocyanines. *Journal of Porphyrins and Phthalocyanines*, 4(5): 441–453, 2000.

[48] Gerhard Ertl, Helmuth Knözinger, Ferdi Schüth, and Jens Weitkamp. *Handbook of heterogeneous catalysis*. Wiley-VCH, 2008.

[49] Sampyo Hong and Talat S. Rahman. Rationale for the higher reactivity of interfacial sites in methanol decomposition on au13/tio2(110). *Journal of the American Chemical Society*, 135(20):7629–7635, 2013. doi: 10.1021/ja4010738. PMID: 23617758.

[50] Davide Ricci, Angelo Bongiorno, Gianfranco Pacchioni, and Uzi Landman. Bonding trends and dimensionality crossover of gold nanoclusters on metal-supported mgo thin films. *Phys. Rev. Lett.*, 97:036106, Jul 2006. doi: 10.1103/PhysRevLett.97.036106.

[51] Atsushi Ueda, Takayuki Nakao, Masashi Azuma, and Tetsuhiko Kobayashi. Two conversion maxima at 373 and 573 k in the reduction of nitrogen monoxide with hydrogen over pd/tio2 catalyst. *Catalysis Today*, 45(1-4):135–138, 1998.

[52] Gengnan Li, Liang Li, Yuan Yuan, Jingjing Shi, Yinyin Yuan, Yongsheng Li, Wenru Zhao, and Jianlin Shi. Highly efficient mesoporous pd/ceo2 catalyst for low temperature co oxidation especially under moisture condition. *Applied Catalysis B: Environmental*, 158:341–347, 2014.

[53] Robert F Hicks and Alexis T Bell. Kinetics of methanol and methane synthesis over pd/sio2 and pd/la2o3. *Journal of Catalysis*, 91(1):104–115, 1985.

[54] Charline Berguerand, Igor Yuranov, Fernando Cárdenas-Lizana, Tatiana Yuranova, and Lioubov Kiwi-Minsker. Size-controlled Pd nanoparticles in 2-butyne-1,4-diol hydrogenation: Support effect and kinetics study. *Journal of Physical Chemistry C*, 118(23):12250–12259, 2014. ISSN 19327455. doi: 10.1021/jp501326c.

[55] Chun-Jern Pan, Meng-Che Tsai, Wei-Nien Su, John Rick, Nibret Gebeyehu Akalework, Abiye Kebede Agegnehu, Shou-Yi Cheng, and Bing-Joe Hwang. Tuning/exploiting Strong Metal-Support Interaction (SMSI) in Heterogeneous Catalysis. *Journal of the Taiwan Institute of Chemical Engineers*, 74:154–186, may 2017. ISSN 18761070. doi: 10.1016/j.jtice.2017.02.012.

[56] S. J. Tauster, S. C. Fung, and R. L. Garten. Strong metal-support interactions. Group 8 noble metals supported on titanium dioxide. *Journal of the American Chemical Society*, 100(1):170–175, jan 1978. ISSN 0002-7863. doi: 10.1021/ja00469a029.

[57] J G Dickson, Lewis Katz, and Roland Ward. Compounds with Hexagonal Barium Titanate StructureThe variation of reliability factor with iridium content in the system Ba(IrxTii-,)0|. The solid line repre. 83, 1961.

[58] J. A. Horsley. A molecular orbital study of strong metal-support interaction between platinum and titanium dioxide. *Journal of the American Chemical Society*, 101(11): 2870–2874, may 1979. ISSN 0002-7863. doi: 10.1021/ja00505a011.

[59] S TAUSTER. Strong metal-support interactions: Occurrence among the binary oxides of groups IIA?VB. *Journal of Catalysis*, 55(1):29–35, oct 1978. ISSN 00219517. doi: 10.1016/0021-9517(78)90182-3.

[60] H SADEGHI. Electronic interactions in the rhodium/TiO2 system. *Journal of Catalysis*, 109(1):1–11, jan 1988. ISSN 00219517. doi: 10.1016/0021-9517(88)90179-0.

[61] Tom W. van Deelen, Carlos Hernández Mejía, and Krijn P. de Jong. Control of metal-support interactions in heterogeneous catalysts to enhance activity and selectivity, nov 2019. ISSN 25201158.

[62] Jeannette Santos, J. Phillips, and J. A. Dumesic. Metal-support interactions between iron and titania for catalysts prepared by thermal decomposition of iron pentacarbonyl and by impregnation. *Journal of Catalysis*, 81(1):147–167, may 1983. ISSN 0021-9517. doi: 10.1016/0021-9517(83)90154-9.

[63] A. David Logan, Ehrich J Braunschweig, Abhaya K Datye, and David J Smith. Direct Observation of the Surfaces of Small Metal Crystallites: Rhodium Supported on TiO2. *Langmuir*, 4(4):827–830, 1988. ISSN 15205827. doi: 10.1021/la00082a009.

[64] Shaofeng Liu, Wei Xu, Yiming Niu, Bingsen Zhang, Lirong Zheng, Wei Liu, Lin Li, and Junhu Wang. Ultrastable Au nanoparticles on titania through an encapsulation strategy under oxidative atmosphere. *Nature Communications 2019 10:1*, 10(1):1–9, dec 2019. ISSN 2041-1723. doi: 10.1038/s41467-019-13755-5.

[65] Hailian Tang, Yang Su, Bingsen Zhang, Adam F. Lee, Mark A. Isaacs, Karen Wilson, Lin Li, Yuegong Ren, Jiahui Huang, Masatake Haruta, Botao Qiao, Xin Liu, Changzi Jin, Dangsheng Su, Junhu Wang, and Tao Zhang. Classical strong metal–support interactions between gold nanoparticles and titanium dioxide. *Science Advances*,

3(10), oct 2017. ISSN 23752548. doi: 10.1126/SCIADV.1700231/SUPPL_FILE/1700231_SM.PDF.

[66] Hope O. Otor, Joshua B. Steiner, Cristina García-Sancho, and Ana C. Alba-Rubio. Encapsulation Methods for Control of Catalyst Deactivation: A Review, jul 2020. ISSN 21555435.

[67] Qiang Fu, Thomas Wagner, Sven Olliges, and Heinz-Dieter Carstanjen. MetalOxide Interfacial Reactions: Encapsulation of Pd on TiO 2 (110). *The Journal of Physical Chemistry B*, 109(2):944–951, jan 2005. ISSN 1520-6106. doi: 10.1021/jp046091u.

[68] A. Berkó, I. Ulrych, and K. C. Prince. Encapsulation of Rh nanoparticles supported on TiO2(110)-(1 × 1) surface: XPS and STM studies. *Journal of Physical Chemistry B*, 102(18):3379–3386, apr 1998. ISSN 15206106. doi: 10.1021/jp973255g.

[69] Xiaoyan Liu, Ming Han Liu, Yi Chia Luo, Chung Yuan Mou, Shawn D. Lin, Hongkui Cheng, Jin Ming Chen, Jyh Fu Lee, and Tien Sung Lin. Strong metal-support interactions between gold nanoparticles and ZnO nanorods in CO oxidation. *Journal of the American Chemical Society*, 134(24):10251–10258, jun 2012. ISSN 00027863. doi: 10.1021/ja3033235.

[70] Víctor A. De La Peña O'Shea, M. Consuelo Álvarez Galván, Ana E. Platero Prats, Jose M. Campos-Martin, and Jose L.G. Fierro. Direct evidence of the SMSI decoration effect: The case of Co/TiO 2 catalyst. *Chemical Communications*, 47 (25):7131–7133, jun 2011. ISSN 1364548X. doi: 10.1039/c1cc10318k.

[71] Wallace T. Figueiredo, Guilherme B. Della Mea, Maximiliano Segala, Daniel L. Baptista, Carlos Escudero, Virginia Pérez-Dieste, and Fabiano Bernardi. Understanding the Strong Metal–Support Interaction (SMSI) Effect in Cu x Ni 1– x /CeO 2 (0 < x < 1) Nanoparticles for Enhanced Catalysis. *ACS Applied Nano Materials*, 2(4):2559–2573, apr 2019. ISSN 2574-0970. doi: 10.1021/acsanm.9b00569.

[72] Qijun Pei, Teng He, Yang Yu, Zijun Jing, Jianping Guo, Lin Liu, Zhitao Xiong, and Ping Chen. Liberating Active Metals from Reducible Oxide Encapsulation for Superior Hydrogenation Catalysis. *ACS Applied Materials Interfaces*, 12(6): 7071–7080, feb 2020. ISSN 1944-8244. doi: 10.1021/acsami.9b17805.

[73] Albert Bruix, José A. Rodriguez, Pedro J. Ramírez, Sanjaya D. Senanayake, Jaime Evans, Joon B. Park, Dario Stacchiola, Ping Liu, Jan Hrbek, and Francesc Illas. A New Type of Strong Metal–Support Interaction and the Production of H 2 through the Transformation of Water on Pt/CeO 2 (111) and Pt/CeO x /TiO 2 (110) Catalysts. *Journal of the American Chemical Society*, 134(21):8968–8974, may 2012. ISSN 0002-7863. doi: 10.1021/ja302070k.

[74] Junjie Li, Qiaoqiao Guan, Hong Wu, Wei Liu, Yue Lin, Zhihu Sun, Xuxu Ye, Xusheng Zheng, Haibin Pan, Junfa Zhu, Si Chen, Wenhua Zhang, Shiqiang Wei, and Junling Lu. Highly Active and Stable Metal Single-Atom Catalysts Achieved by Strong Electronic Metal–Support Interactions. *Journal of the American Chemical Society*, 141(37):14515–14519, sep 2019. ISSN 0002-7863. doi: 10.1021/jacs.9b06482.

[75] Qiang Fu and Thomas Wagner. Interaction of nanostructured metal overlayers with oxide surfaces. *Surface Science Reports*, 62(11):431–498, nov 2007. ISSN 01675729. doi: 10.1016/j.surfrep.2007.07.001.

[76] W. Schottky. Halbleitertheorie der Sperrschicht. *Naturwissenschaften 1938 26:52*, 26(52):843–843, dec 1938. ISSN 1432-1904. doi: 10.1007/BF01774216.

[77] N. F. Mott. Note on the contact between a metal and an insulator or semi-conductor. *Mathematical Proceedings of the Cambridge Philosophical Society*, 34(4):568–572, 1938. ISSN 1469-8064. doi: 10.1017/S0305004100020570.

[78] John Bardeen. Surface states and rectification at a metal semi-conductor contact. *Physical Review*, 71(10):717–727, may 1947. ISSN 0031899X. doi: 10.1103/PhysRev.71.717.

[79] Volker Heine. Theory of surface states. *Physical Review*, 138(6A):A1689, jun 1965. ISSN 0031899X. doi: 10.1103/PhysRev.138.A1689.

[80] W. Monch. On the physics of metal-semiconductor interfaces. *Reports on Progress in Physics*, 53(3):221, mar 1990. ISSN 0034-4885. doi: 10.1088/0034-4885/53/3/001.

[81] Raymond T. Tung. Recent advances in Schottky barrier concepts. *Materials Science and Engineering: R: Reports*, 35(1-3):1–138, nov 2001. ISSN 0927-796X. doi: 10.1016/S0927-796X(01)00037-7.

[82] Theophilos Ioannides and Xenophon E. Verykios. Charge Transfer in Metal Catalysts Supported on Doped TiO2: A Theoretical Approach Based on Metal–Semiconductor Contact Theory. *Journal of Catalysis*, 161(2):560–569, jul 1996. ISSN 0021-9517. doi: 10.1006/JCAT.1996.0218.

[83] ALESSANDRO TROVARELLI. Catalytic Properties of Ceria and CeO 2 - Containing Materials. *Catalysis Reviews*, 38(4):439–520, nov 1996. ISSN 0161-4940. doi: 10.1080/01614949608006464.

[84] Yun Zhao, Xiwen Zhou, Lin Ye, and Shik Chi Edman Tsang. Nanostructured Nb 2 O 5 catalysts. *Nano Reviews*, 3(1):17631, jan 2012. ISSN 2000-5121. doi: 10.3402/nano.v3i0.17631.

[85] Alan Jones. *Tempature-programmed reduction for solid materials characterization*, volume 24. CRC Press, 1986.

[86] JW Jenkins. Gordon research conference on catalysis. *Colby-Sawyer College, New London, New Hampshire*, 1975.

[87] Nicholas W. Hurst, Stephen J. Gentry, and Alan Jones. Temperature Programmed Reduction. *Catalysis Reviews*, 24(2):233–309, jan 1982. ISSN 15205703. doi: 10.1080/03602458208079654.

[88] W. Smykatz-Kloss and Springer-Verlag (Berlin). *Differential Thermal Analysis: Application and Results in Mineralogy*. Ecological Studies. Springer-Verlag, 1974. ISBN 9783540069065.

[89] H Le Chatelier. The constitution of clay. *Z. physik. Chem*, 1:396, 1887.

[90] Marjorie J Vold. Differential thermal analysis. *Analytical chemistry*, 21(6):683–688, 1949.

[91] David B. Williams and C. Barry Carter. *Transmission electron microscopy: A textbook for materials science*. Springer US, 2009. ISBN 9780387765006. doi: 10.1007/978-0-387-76501-3.

[92] Mohammad Jafari Eskandari, Ali Shafyei, and Fathallah Karimzadeh. One-step fabrication of Au@Al2O3 core-shell nanoparticles by continuous-wave fiber laser ablation of thin gold layer on aluminum surface: Structural and optical properties. *Optics and Laser Technology*, 126:106066, jun 2020. ISSN 00303992. doi: 10.1016/j.optlastec.2020.106066.

[93] W. Schärtl. *Light Scattering from Polymer Solutions and Nanoparticle Dispersions*. Springer Laboratory. Springer Berlin Heidelberg, 2007. ISBN 9783540719519.

[94] Christina Cruickshank. The Stokes-Einstein law for diffusion in solution. *Proceedings of the Royal Society of London. Series A, Containing Papers of a Mathematical and Physical Character*, 106(740):724–749, dec 1924. ISSN 0950-1207. doi: 10.1098/RSPA.1924.0100.

[95] Wilhelm Conrad Röntgen. Uber eine neue art von strahlen. *Sitzungsber Phys Med Ges Wurtzburg*, 9:132–141, 1895.

[96] Challapalli Suryanarayana and M Grant Norton. *X-ray diffraction: a practical approach*. Springer Science & Business Media, 2013.

[97] Vitalij K. Pecharsky and Peter Y. Zavalij. *Fundamentals of Powder Diffraction and Structural Characterization of Materials*. Springer US, Boston, MA, 2009. ISBN 978-0-387-09578-3. doi: 10.1007/978-0-387-09579-0.

[98] Max von Laue. Concerning the detection of X-ray interferences. *Nobel lecture*, pages 347–355, jun 1920.

[99] W H Bragg and W L Bragg. The reflection of X-rays by crystals. *Proceedings of the Royal Society of London. Series A, Containing Papers of a Mathematical and Physical Character*, 88(605):428–438, jul 1913. ISSN 0950-1207. doi: 10.1098/rspa.1913.0040.

[100] H. M. Rietveld. A profile refinement method for nuclear and magnetic structures. *Journal of Applied Crystallography*, 2(2):65–71, jun 1969. ISSN 00218898. doi: 10.1107/S0021889869006558.

[101] V. Pecharsky and P. Zavalij. *Fundamentals of Powder Diffraction and Structural Characterization of Materials, Second Edition.* Springer US, 2008. ISBN 9780387095790.

[102] L. W. Finger, D. E. Cox, and A. P. Jephcoat. A correction for powder diffraction peak asymmetry due to axial divergence. *Journal of Applied Crystallography*, 27(6): 892–900, Dec 1994. doi: 10.1107/S0021889894004218.

[103] John F. Watts and John Wolstenholme. *An Introduction to Surface Analysis by XPS and AES.* John Wiley Sons, Ltd, mar 2003. ISBN 0-470-84713-1. doi: 10.1002/0470867930.

[104] M. P. Seah and W. A. Dench. Quantitative electron spectroscopy of surfaces: A standard data base for electron inelastic mean free paths in solids. *Surface and Interface Analysis*, 1(1):2–11, feb 1979. ISSN 10969918. doi: 10.1002/sia.740010103.

[105] C. S. Fadley and A. D. Baker, editors. *Electron Spectroscopy: Theory, Techniques and Applications*, volume 2. Academic Press, 1978.

[106] V. Pérez-Dieste, L. Aballe, S. Ferrer, J. Nicolàs, C. Escudero, A. Milán, and E. Pellegrin. Near ambient pressure XPS at ALBA. In *Journal of Physics: Conference Series*, volume 425, page 072023. Institute of Physics Publishing, mar 2013. doi: 10.1088/1742-6596/425/7/072023.

[107] D. Frank Ogletree, Hendrik Bluhm, Eleonore D. Hebenstreit, and Miquel Salmeron. Photoelectron spectroscopy under ambient pressure and temperature conditions. *Nuclear Instruments and Methods in Physics Research, Section A: Accelerators, Spectrometers, Detectors and Associated Equipment*, 601(1-2):151–160, mar 2009. ISSN 01689002. doi: 10.1016/j.nima.2008.12.155.

[108] J.H.D. Eland. *Photoelectron Spectroscopy: An Introduction to Ultraviolet Photoelectron Spectroscopy in the Gas Phase.* Elsevier Science, 2013. ISBN 9781483103211.

[109] S Krischok, P Stracke, and V Kempter. Metal (cu; pd) adsorption on mgo: investigations with mies and ups. *Applied Physics A*, 82(1):167–173, 2006.

[110] W Kohn. Nobel Lecture: Electronic structure of matter—wave functions and density functionals. *Reviews of Modern Physics*, 71(5):1253–1266, oct 1999. ISSN 0034-6861. doi: 10.1103/RevModPhys.71.1253.

[111] L. H. Thomas. The calculation of atomic fields. *Mathematical Proceedings of the Cambridge Philosophical Society*, 23(5):542–548, jan 1927. ISSN 0305-0041. doi: 10.1017/S0305004100011683.

[112] Fermi Enrico. Un metodo statistico per la determinazione di alcune prioprieta dell'atomo. *Rend. Accad. Naz. Lincei*, 6:602–607, 1927.

[113] D. R. Hartree. The Wave Mechanics of an Atom with a Non-Coulomb Central Field. Part I. Theory and Methods. *Mathematical Proceedings of the Cambridge Philosophical Society*, 24(1):89–110, jan 1928. ISSN 0305-0041. doi: 10.1017/S0305004100011919.

[114] V. Fock. Näherungsmethode zur Lösung des quantenmechanischen Mehrkörperproblems. *Zeitschrift für Physik*, 61(1-2):126–148, jan 1930. ISSN 1434-6001. doi: 10.1007/BF01340294.

[115] W. Pauli. Über den Zusammenhang des Abschlusses der Elektronengruppen im Atom mit der Komplexstruktur der Spektren. *Zeitschrift für Physik*, 31(1):765–783, feb 1925. ISSN 0044-3328. doi: 10.1007/BF02980631.

[116] P. Hohenberg and W. Kohn. Inhomogeneous Electron Gas. *Physical Review*, 136 (3B):B864–B871, nov 1964. ISSN 0031-899X. doi: 10.1103/PhysRev.136.B864.

[117] E.K.U. Gross and R.M. Dreizler. *Density Functional Theory*. Nato Science Series B:. Springer US, 2013. ISBN 9781475799750.

[118] W. Kohn and L. J. Sham. Self-Consistent Equations Including Exchange and Correlation Effects. *Physical Review*, 140(4A):A1133–A1138, nov 1965. ISSN 0031-899X. doi: 10.1103/PhysRev.140.A1133.

[119] John P. Perdew, Weitao Yang, Kieron Burke, Zenghui Yang, Eberhard K.U. U. Gross, Matthias Scheffler, Gustavo E. Scuseria, Thomas M. Henderson, Igor Ying Zhang, Adrienn Ruzsinszky, Haowei Peng, Jianwei Sun, Egor Trushin, and Andreas Görling. Understanding band gaps of solids in generalized Kohn–Sham theory. *Proceedings of the National Academy of Sciences*, 114(11):2801–2806, mar 2017. ISSN 0027-8424. doi: 10.1073/pnas.1621352114.

[120] Ylva Andersson, Erika Hult, Henrik Rydberg, Peter Apell, Bengt I. Lundqvist, and David C. Langreth. Van der Waals Interactions in Density Functional Theory. *Electronic Density Functional Theory*, pages 243–260, 1998. doi: 10.1007/978-1-4899-0316-7_17.

[121] Paolo Giannozzi, Stefano Baroni, Nicola Bonini, Matteo Calandra, Roberto Car, Carlo Cavazzoni, Davide Ceresoli, Guido L. Chiarotti, Matteo Cococcioni, Ismaila Dabo, Andrea Dal Corso, Stefano De Gironcoli, Stefano Fabris, Guido Fratesi, Ralph Gebauer, Uwe Gerstmann, Christos Gougoussis, Anton Kokalj, Michele Lazzeri, Layla Martin-Samos, Nicola Marzari, Francesco Mauri, Riccardo Mazzarello, Stefano Paolini, Alfredo Pasquarello, Lorenzo Paulatto, Carlo Sbraccia, Sandro Scandolo, Gabriele Sclauzero, Ari P. Seitsonen, Alexander Smogunov, Paolo Umari, and Renata M. Wentzcovitch. QUANTUM ESPRESSO: a modular and open-source software project for quantum simulations of materials. *Journal of Physics: Condensed Matter*, 21(39):395502, sep 2009. ISSN 0953-8984. doi: 10.1088/0953-8984/21/39/395502.

[122] G. Kresse and J. Furthmüller. Efficient iterative schemes for ab initio total-energy calculations using a plane-wave basis set. *Physical Review B*, 54(16):11169–11186, oct 1996. ISSN 0163-1829. doi: 10.1103/PhysRevB.54.11169.

[123] José M. Soler, Emilio Artacho, Julian D. Gale, Alberto García, Javier Junquera, Pablo Ordejón, and Daniel Sánchez-Portal. The SIESTA method for ab initio order-N materials simulation. *Journal of Physics: Condensed Matter*, 14(11):2745–2779, mar 2002. ISSN 0953-8984. doi: 10.1088/0953-8984/14/11/302.

[124] Stewart J. Clark, Matthew D. Segall, Chris J. Pickard, Phil J. Hasnip, Matt I.J. Probert, Keith Refson, and Mike C. Payne. First principles methods using CASTEP. *Zeitschrift fur Kristallographie*, 220(5-6):567–570, may 2005. ISSN 00442968. doi: 10.1524/zkri.220.5.567.65075.

[125] Xavier Gonze, Bernard Amadon, Gabriel Antonius, Frédéric Arnardi, Lucas Baguet, Jean Michel Beuken, Jordan Bieder, François Bottin, Johann Bouchet, Eric Bousquet, Nils Brouwer, Fabien Bruneval, Guillaume Brunin, Théo Cavignac, Jean Baptiste Charraud, Wei Chen, Michel Côté, Stefaan Cottenier, Jules Denier, Grégory Geneste, Philippe Ghosez, Matteo Giantomassi, Yannick Gillet, Olivier Gingras, Donald R. Hamann, Geoffroy Hautier, Xu He, Nicole Helbig, Natalie Holzwarth, Yongchao Jia, François Jollet, William Lafargue-Dit-Hauret, Kurt Lejaeghere, Miguel A.L. Marques, Alexandre Martin, Cyril Martins, Henrique P.C. Miranda, Francesco Naccarato, Kristin Persson, Guido Petretto, Valentin Planes, Yann Pouillon, Sergei Prokhorenko, Fabio Ricci, Gian Marco Rignanese, Aldo H. Romero, Michael Marcus Schmitt, Marc Torrent, Michiel J. van Setten, Benoit

Van Troeye, Matthieu J. Verstraete, Gilles Zérah, and Josef W. Zwanziger. The ABINITproject: Impact, environment and recent developments. *Computer Physics Communications*, 248:107042, mar 2020. ISSN 00104655. doi: 10.1016/j.cpc.2019.107042.

[126] Frank Neese. The ORCA program system. *Wiley Interdisciplinary Reviews: Computational Molecular Science*, 2(1):73–78, jan 2012. ISSN 17590876. doi: 10.1002/wcms.81.

[127] M. J. Frisch, G. W. Trucks, H. B. Schlegel, G. E. Scuseria, M. A. Robb, J. R. Cheeseman, G. Scalmani, V. Barone, G. A. Petersson, H. Nakatsuji, X. Li, M. Caricato, A. V. Marenich, J. Bloino, B. G. Janesko, R. Gomperts, B. Mennucci, H. P. Hratchian, J. V. Ortiz, A. F. Izmaylov, J. L. Sonnenberg, D. Williams-Young, F. Ding, F. Lipparini, F. Egidi, J. Goings, B. Peng, A. Petrone, T. Henderson, D. Ranasinghe, V. G. Zakrzewski, J. Gao, N. Rega, G. Zheng, W. Liang, M. Hada, M. Ehara, K. Toyota, R. Fukuda, J. Hasegawa, M. Ishida, T. Nakajima, Y. Honda, O. Kitao, H. Nakai, T. Vreven, K. Throssell, J. A. Montgomery, Jr., J. E. Peralta, F. Ogliaro, M. J. Bearpark, J. J. Heyd, E. N. Brothers, K. N. Kudin, V. N. Staroverov, T. A. Keith, R. Kobayashi, J. Normand, K. Raghavachari, A. P. Rendell, J. C. Burant, S. S. Iyengar, J. Tomasi, M. Cossi, J. M. Millam, M. Klene, C. Adamo, R. Cammi, J. W. Ochterski, R. L. Martin, K. Morokuma, O. Farkas, J. B. Foresman, and D. J. Fox. Gaussian~16 Revision C.01, 2016. Gaussian Inc. Wallingford CT.